Thèse n° 9468

Controlling motion at the nanoscale with light

Présentée le 18 novembre 2022

Faculté des sciences et techniques de l'ingénieur
Laboratoire de nanophotonique et métrologie
Programme doctoral en photonique

pour l'obtention du grade de Docteur ès Sciences

par

Mintae CHUNG

Acceptée sur proposition du jury

Prof. Y. Bellouard, président du jury
Prof. O. Martin, directeur de thèse
Prof. Q.-H. Park, rapporteur
Prof. K. Crozier, rapporteur
Prof. J. Brugger, rapporteur

École
polytechnique
fédérale
de Lausanne

2022

Acknowledgements

I am grateful to take this opportunity to thank everyone who has supported and helped me in many ways during the journey of my PhD for the past four and half years. Without them, I would not have made my PhD successful.

In particular, a special thanks to Prof. Olivier J.F. Martin, who offered me the opportunity to work at the Nanophotonics and Metrology laboratory and supervised me during my doctoral program. I was able to keep moving forward against all odds thanks to the inspiring discussion with him and the helpful guidance and support from him. All the projects I was involved in would not have worked without him. I appreciate many talented colleagues who are always open to numerous discussions on many different subjects. I used to look for Jenna and Christian when I faced some difficulties in optical measurements and nanofabrication, which are critical parts of my work. I thank Karim and Andrei for their endless help every time I have some problems in numerical calculations. I would also like to thank Marco, Debdatta, Andre-Pierre, Dong-Cheon, Hsiang-Chu, Ville, Tao, and Sergejs. All our discussions were constructive and provided me with scientific insight. I thank CMi staff, Zdenek, Joffrey, Cyrille, Remy, Guy, and Julien, for their devoted help because the experimental part of my work is highly involved with nanofabrication.

I would also like to thank Prof. Anna Fontcuberta i Morral, who supervised me in my master's thesis project at LMSC. Without her, my journey in Switzerland would not have started. I also appreciate help and support from my former colleagues at LMSC, Martin F, Lucas, Wonjong, Nick, Luca, Didem, Rajrupa, Valerio, Elias, Anna K, Andrea, and Simon. I also thank my former flatmate Sho, who helped me calm down whenever I encountered difficulties. Living with him was one of the funniest moments in my life.

Many thanks to the members of the Korean student association at EPFL: Minkyung, Joowon, Kyunghwan, Hanhee, Jaejun, Hakgu, Daehyun, Taeheon, Jinwoo, Hyungoo, Umji, Jisoo, Jihyun, Oh-Hyun, and others. They always encouraged me and made me feel comfortable. We had many meaningful conversations, sharing the joys and difficulties of studying abroad together.

I would also like to thank the members of the thesis committee, Prof. Yves Bellouard, Prof. Q-Han Park, Prof. Kenneth B. Crozier, and Prof. Jürgen Brugger for accepting to be members

of the jury and for the valuable comments to this manuscript.
Finally, I would like to express my gratitude to my family and relatives. Unconditional love from them always makes me feel like being with them, although it has been almost seven years since I moved to Europe. In particular, a special thanks to my father for always listening to my opinion, believing in me, and supporting me. Although he passed away four months before my public defense and was not able to see the last moment of my PhD, he will live forever in my heart.

Lausanne, 27 October 2022 Mintae CHUNG

Abstract

Optical manipulation at the micro- nano-scale is a fascinating topic due to its inherent non-invasive properties and multifaceted applications in various fields such as biology, sensing, micro-fluidics, and micro- nano-robotics. This thesis involves intensive efforts dedicated to realizing the rotational motion and trapping. Despite recent developments, selecting the most efficient and powerful nanomotor is still not obvious. Therefore, this thesis provides a comprehensive understanding of the current state of affairs for optically-driven motors and solutions for nanomotor design, numerical analysis, and nanofabrication.

Motors at the micro- nano-scale have diversified and emerged as versatile devices due to their ability to control mechanical motions. For the past two decades, the development of man-made optical motors has been remarkable, as the recent advancements in fabrication technologies have gradually enhanced the resolution and precision of manufacturing equipment. An in-depth review provides comprehensive insights into the physical mechanisms of micro- and nano-motors driven by light momenta. Diverse micro- nano-technologies that enable motor fabrication are introduced. The applications in various fields such as biology, sensing, micro-fluidics, and micro- nano-robotics are summarized. Future directions, anticipated in view of the collaborative exploitation of other research fields, such as machine learning, metasurfaces, and 2D materials, are also discussed.

I demonstrate that a machine learning algorithm as a global solution can produce nanorotor structures generating improved optical torques for a given incident light. The combination of two different fields, machine learning and nanomotors, via nanofabrication requires substantial optimization processes in deep learning algorithms, fabrication parameters, and optical measurements, which have been described in great detail in this thesis. A torque predictor made of a convolutional neural network (CNN) is connected to a deep convolution generative adversarial network (DCGAN) nanorotor generator. An electromagnetic surface integral equation (SIE) scheme provides a numerical method to obtain the scattering cross-section (SCS), multipole expansion, optical torque, and electric field enhancement distribution for the generated nanorotors. The nanorotor structures obtained from the algorithms are realized by nanofabrication techniques such as electron beam lithography (EBL), thin film deposition,

and various etching processes, and are implemented in a SiO_2 embodiment to build nanomotors. The nanorotors suggested by the artificial intelligence exhibit improved rotation speeds compared to conventional designs based on V-shape, rods, or gammadion structures.
The realization of sophisticated structures at the nanoscale is critical for linking an ideal design with real devices. The importance of ion beam etching (IBE) is growing due to its ability to fabricate tiny gaps and sharp features for plasmonic responses. However, as the required features go down to a few tens of nanometers, inevitable fences, which occur due to physical bombardment and redeposition, cause the expansion of the structure. This gives rise to unexpected behaviors for the fabricated nanostructures. To quantify and solve these issues, a series of structures have been fabricated using different etch mask heights and, subsequently, analyzed by investigating their cross-section. The optimized recipe provides high quality nanostructures with features as designed. In addition, doughnut rings placed around the nanostructures and Au wet etch carried out after the aforementioned process led to a further improvement. The doughnut ring structures allow for suppression of the expansion during IBE. The additional Au wet etch step removed the fences on the sidewall.
Optical trapping has attracted a lot of attention due to its promising applications. In addition to the rotating motion described above, we introduce in this thesis an experiment aimed at visualizing trapping events in plasmonic apertures in this thesis. The idea relies on a combination of optical trapping and Föster or fluorescence resonance energy transfer (FRET) between trapped fluorescent particles (FRET donor) and the plasmonic apertures that have been functionalized with FRET acceptor molecules. A dyed polystyrene (PS) beads solution is injected on top of the plasmonic nanostructures in a confined chamber. For the FRET measurement, a laser is focused onto the nanoaperture using an objective. The dyed PS beads are drawn to the nanoaperture by optical forces, and FRET occurs once PS beads are close enough to the functionalized plasmonic nanoaperture.

Keywords: Electromagnetism, Plasmonics, Multipolar modes, Optical angular momentum, Nanomotor, Machine learning, Convolutional neural network, Generative adversarial network, Optical torque, Nanofabrication, Electron beam lithography, Ion beam etching, Focused ion beam, Extraordinary optical transmission, Optical trapping.

Résumé

La manipulation optique à l'échelle micro-nano est un sujet fascinant en raison de ses propriétés non invasives inhérentes et de ses applications passionnantes dans divers domaines tels que la biologie, la détection, la micro-fluidique et la micro-nano-robotique. Cette thèse est le résultat d' efforts intensifs dédiés principalement à la réalisation du mouvement de rotation et du piégeage. Malgré les développements récents, la sélection du nanomoteur le plus efficace et le plus puissant n'est toujours pas manifeste. Par conséquent, cette thèse fournit une compréhension globale de l'état actuel des moteurs à commande optique et des solutions de conception de nanomoteurs, d'analyse numérique et de nanofabrication.

Les moteurs à l'échelle micro-nano se sont diversifiés et sont devenus des dispositifs polyvalents grâce à la grande contrôlabilité de leur mouvements mécaniques. Au cours des deux dernières décennies, le développement des moteurs optiques artificiels a été remarquable, les progrès récents des technologies de fabrication améliorant progressivement la résolution et la précision des équipements de fabrication. Cette étude fournit un aperçu complet des mécanismes physiques des micro-nano-moteurs entraînés par des impulsions lumineuses. Diverses micro-nano-technologies permettant la fabrication de moteurs sont introduites. Les applications dans divers domaines tels que la biologie, la détection, la micro-fluidique et la micro-nano-robotique sont résumées. Les orientations futures, anticipées en vue d'une exploitation collaborative d'autres domaines de recherche, tels que l'apprentissage automatique, les métasurfaces et les matériaux 2D, sont également discutées.

Une démonstration qu'un algorithme d'apprentissage automatique en tant que solution globale peut produire des structures de nanorotor générant des couples optiques améliorés pour une lumière incidente donnée est introduite. La combinaison de deux domaines différents, l'apprentissage automatique et les nanomoteurs, via la nanofabrication, nécessite des processus d'optimisation substantiels dans les algorithmes d'apprentissage en profondeur, les paramètres dans les procédés de fabrication et les mesures optiques, qui sont décrits en détail dans la thèse. Un prédicteur de couple constitué d'un réseau neuronal convolutif (CNN) est connecté à un générateur de nanorotor à réseau antagoniste génératif à convolution profonde (DCGAN). Un schéma d'équation intégrale de surface électromagnétique (SIE) fournit une

méthode numérique pour obtenir la section efficace de diffusion (SCS), l'expansion multipolaire, le couple optique et la distribution d'amélioration du champ électrique des nanorotors générés. Les structures de nanorotor obtenues à partir de l'algorithme sont réalisées par des techniques de nanofabrication utilisant la lithographie par faisceau d'électrons (EBL), le dépôt de couches minces et divers processus de gravure et sont mises en œuvre dans un mode de réalisation SiO_2 pour construire des nanomoteurs. Les rotors générés par l'apprentissage automatique présentent des vitesses de rotation améliorées par rapport aux conceptions conventionnelles basées sur des structures en forme de V, de tiges ou de gammadions.
La réalisation de structures sophistiquées à l'échelle nanométrique est essentielle pour lier conception idéale et dispositifs réels. L'importance de la gravure par faisceau d'ions (IBE) augmente en raison de sa capacité à fabriquer de minuscules écarts et des caractéristiques nettes pour les réponses plasmoniques. Cependant, comme les dimensions caractéristiques requises atteignent les quelques dizaines de nanomètres, des barrières inévitables, dues au bombardement physique et à la redéposition, provoquent l'expansion de la structure. Cela engendre des comportements inattendus des nanostructures. Pour quantifier et résoudre le problème, une série de structures ont été fabriquées en utilisant différentes hauteurs de masque de gravure et, par la suite, analysées en étudiant la section transversale. La recette optimisée fournit des nanostructures de haute qualité avec des fonctionnalités telles que conçues. De plus, des anneaux de beignets placés autour des nanostructures et une gravure humide Au réalisée après le procédé susmentionné ont permis une amélioration supplémentaire. Les structures en anneau permettent de supprimer l'expansion pendant l'IBE. L'étape supplémentaire de gravure humide Au a supprimé les barrières sur la paroi latérale.
La principale manipulation optique, le piégeage optique, a attiré beaucoup d'attention en raison de ses applications prometteuses. En plus du mouvement de rotation décrit ci-dessus, nous introduisons dans cette thèse une expérience visant à visualiser les événements de piégeage dans les ouvertures plasmoniques. L'idée repose sur une combinaison de piégeage optique et de Föster ou transfert d'énergie par résonance de fluorescence (FRET) entre les particules fluorescentes piégées (donneur de FRET) et les ouvertures plasmoniques qui ont été fonctionnalisées avec des molécules accepteuses de FRET. Une solution de billes de polystyrène teinté (PS) est injectée au-dessus des nanostructures plasmoniques dans une chambre confinée. Pour la mesure de FRET, un laser est focalisé sur la nano-ouverture à l'aide d'un objectif. Les billes de PS colorées sont attirées vers la nano-ouverture par des forces optiques, et le FRET se produit une fois que les billes de PS sont suffisamment proches de la nano-ouverture plasmonique fonctionnalisée.

Contents

List of Figures

List of Tables

1 Introduction

Since Ashkin demonstrated the optical tweezer using a highly focused laser beam, optical trapping has become an attractive research topic thanks to its promising applications [1, 2]. The smallest specimen size and optical power required have been considerably improved to a few nanometers and a few microwatts [3]. Various materials such as metal, dielectric particles, single molecules, cells, and DNA have been successfully manipulated with optical traps [4, 5, 6]. However, optical tweezing requires high optical energy to trap sub-micron particles, which can destroy the specimen, and focusing with an objective lens encounters the diffraction limit [7]. To overcome these limitations, plasmonic structures, which can provide local field enhancement and localization, have attracted a significant attention [7, 3]. Optical trapping with plasmonic structures is realized by various platforms: coaxial structures [8], antennas [9], apertures [10], arrays [11], and gaps [12]. In addition, exploring optical sorting [13], pulling [14], binding [15], assembling [16], and rotating [17] have been followed to extend the manipulation methods. All these intriguing phenomena are possible thanks to optical forces exerted on an object by the incident light [2]. In this thesis, I contribute to rotational motion and trapping applications by developing fabrication technologies for such sophisticated geometries.

Among the various methods in optical manipulation, optically-driven motors generating optical torques on objects have been developed and experimentally verified by researchers in various configurations [18, 19, 20]. The rotational properties originate from the interaction between the object geometry and the incident light or the transfer of the angular momentum of light into absorbing objects. Redirecting the incident light by refraction and reflection induces the transverse components of the momentum and leads to the mechanical rotational motion, i.e., the conservation of the momentum of light results in optical torques. Birefringent particles that change the direction of circular polarization of light obtain angular momen-

tum from the incident circularly polarized light [21]. In addition, plasmonic resonances can play a role in the additional enhancement of the rotational speed [22, 23, 24]. The development of optically-driven motors has progressed with the improvement of nanotechnologies. Photolithography-based etching at the microscale gave rise to the early motors driven by momentum exchange by refraction and reflection [25]. Two-photon polymerization realized even 3D structure [26], and the resolution went down to a few microns. The refraction and reflection of 3D geometries cause more photons to interact with the structure and induce faster rotation for a given illumination light [27]. Nanoparticle synthesis for spheres, rods, or other shapes has been developed and used to realize rotary motors driven by linearly polarized light or light carrying angular momentum [28, 29, 30]. The recent developments of nanotechnology enable sophisticated geometries for plasmonic resonances [23]. The enhancement of scattering dominant motors is possibly attributed to the plasmonic resonance [31]. When light is incident on an object, absorbing and scattering occur simultaneously. Therefore, the combination of absorbing and scattering optical torques leads to stronger torques [22]. In particular, both absorption and scattering can be enhanced by plasmonic resonances. These promising factors have attracted great attention from researchers [32]. Yet, the geometry of optical motors remains intuitively simple, like rods, spheres, V-shapes, and gammadion [33, 31, 29, 23]. Nowadays, many researchers try to improve device performances using machine learning [34]. Thanks to the tremendous calculations and weight updates, this approach provides solutions beyond the human intuition. On the other hand, I noticed that the optical torque value of planar metallic nanomotors depends on their geometry. Accordingly, I have naturally been motivated by the fact that machine learning could be used in the design of nanomotors.

Optical trapping with aperture-type structures has widely been verified in various platforms and have attracted considerable attention due to its promising applications [10, 35, 36, 37, 38]. In addition to the rotational motion, I studied a combination of optical trapping using nanoaperture structures and the fluorescence resonance energy transfer (FRET) phenomenon. FRET occurs when a suitable pair of donor and acceptor molecules have a distance smaller than 20 nm [39]. With this distance cognitive ability, the performance of optical trapping can be evaluated by the intensity of the emission signal of acceptors. In the experiment, donor molecules are functionalized on the trapped particles, while acceptor molecules are immobilized on the trap site. The energy transfer is the evidence that the distance between donor and acceptor is less than 20 nm. Various methods are tried and discussed for the visualization of trapping using FRET.

Thesis objectives

This thesis aims to develop nanofabrication processes to provide nanostructures dedicated to optical manipulations such as rotation and trapping. To achieve this goal, various nanofabrication technologies have been explored. The rotational motion is realized by combining two works: the optimization of machine learning algorithms to produce nanostructures with improved optical torques and the development of nanofabrication techniques to produce nanostructures suggested by the machine learning algorithms. For the optical trapping, periodic structures exhibiting plasmonic resonances are fabricated using focused ion beam milling. Accordingly, a detailed numerical analysis of the optical properties of the nanostructures has been conducted to understand the fundamental principles. Finally, the optical manipulations with the fabricated nanostructures are verified with spectroscopy, rotation, and trapping measurements.

Thesis organization

A review of the recent advances in optically-driven motors is provided in Chapter 2. A brief historical introduction, as well as the physics and fabrication techniques of motors, are discussed. Promising applications of motors in various fields are reviewed. Chapter 3 provides a detailed description of the development of machine learning algorithms for optical torque predictor and nanostructure generator, numerical analysis of optical properties of nanostructures using the surface integral equation (SIE) methods, and fabrication techniques used in this thesis. In Chapter 4, the study of optimization of ion beam etching (IBE) for Au plasmonic nanostructures at the nanoscale is detailed, and the realization of widely used nanostructures with the optimized process is presented. In Chapter 5, the visualization of optical trapping using FRET is explored with the purpose of quantifying the trapping performance. A conclusion is provided in Chapter 6, along with an outlook for future opportunities for research and development.

2 Recent advances in optical rotary motions at the micro- nano-scale

The material presented here will be submitted for a review article.

2.1 Introduction

Micro- nano-motors have constantly attracted many researchers owing to their great potential in biology [40], biomedicine [41], nanostructure fabrication [42], micro- nano-robot [43], and micro- nano-scale manipulation [44] since the concept of tiny machines was suggested by Feynmann [45]. As nanotechnology and bio-chemical synthesis have advanced, various methods to realize micro- nano-motors have been proposed and demonstrated with tremendous efforts made by researchers [44, 46, 47, 48, 49]. Micro- nano-motors are translation and actuation devices converting energy from various sources such as electric and magnetic fields, chemical reaction, heating, and acoustic waves into mechanical momentum. Depending on the applications, they have different names: motor, sensor, actuator, swimmer, and tracer.

Applications of micro- nano-motors

The small aforementioned motors are particularly promising in biology and bio-medicine due to the diverse applications such as delivery, surgery, sensing, DNA stretching, and detoxification, [41, 50, 51]. For example, a micromotor rotating in the vitreous of a living rabbit has already proved that it can be used for precise, wireless, and invasive surgery [52]. The towing ability of the nanomotor with functional surfaces leads to active and efficient bio-sensing [53]. A torque exertion of about tens of pN·nm at the nanoscale is sufficient to precisely stretch and overwind DNA [54, 55]. Micro- nano-motors can also serve as a part of micro- nano-scale machines such as NEMS/MEMS and nanorobots. In general, NEMS/MEMS devices consist

of mechanical and electrical components[56, 57, 58]. Among the mechanical components, nanomotors can be inherently used as a physical actuator by which NEMS/MEMS devices can achieve the desired functionality. The rotational motion of motors can adjust oscillatory components in MEMS, which is suitable for sensing applications [59]. Micro- nano-motors are also inherently promising in lab-on-a-chip applications due to their stable rotational movement at the nanoscale which enables the precise flow control [60]. Conventionally, a syringe pump is used to control the flow in micro-fluidics. However, one might encounter difficulties in adjusting the flow rate with the syringe pump due to the oscillating flow [61]. In the case of pressure pumps with multiple entry points, backflow might also be a problem. Optically-driven motors allow non-destructive actuation to generate the continuous flow in micro-fluidics such that no additional needle-based liquid injection is required [62]. The flow at the pN scale made by the nanomotor facilitates the precise control within the chip under low Reynolds numbers [22]. Nanomotors have many potentials in various fields, just like the electric motor invented by Michael Faraday and has found applications in automobiles, ships, and factories has changed the human lifestyle [63].

Various methods to generate rotary motion

The term, micro- nano-motor, refers to the platforms that generate either rotational or propulsion motions by converting electric, magnetic, thermal, chemical, biological, or optical energies into mechanical motions [44]. Let us illustrate the realization of micro- nano-motors with the following examples. Mycoplasma mobile cells were found to unidirectionally glide with the speed of 2-5 μm/s along microcracks while growing through fission [64]. When attached to a dielectric motor platform, rotation occurs; even though the mechanism of gliding is not verified, researchers make use of this behavior. The mobile cells are powerful as the resource of propulsion due to the self-repair and self-organization. On the other hand, bio-compatible motors can also make use of flagella to obtain propulsion [65]. When it comes to electric fields, it can drive micro- nano-sized metallic particles and carbon nanotubes (CNTs). The metallic nano-objects are aligned along the external electric field to lower the potential energy [66]. The rotation of electric fields induces the rotational movement of the nanomotors [66, 67, 68]. Likewise, magnetic entities that align along the magnetic fields can be driven by rotating magnetic fields [69, 70]. Magnetically functionalized nanoparticles propagate along the field gradients [71]. The geometry of the magnetic field-driven swimmer converts the magnetic rotation into linear propulsion [72]. Chemical motors gain kinetic momentum from various chemical reactions [47, 73]. The decomposition of the surrounding molecules leads to mechanical motion. For example, the light illumination provokes a chemical reaction on the

Au – TiO_2 side and results in the photocatalytic decomposition of H_2O_2. The by-products, 0_2 molecules, emerge and give rise to propulsion from 0_2 bubbles [74]. In this case, photochemical energy is converted into mechanical motion. On the other hand, light illumination can generate the localized surface plasmon heating on the Au side of the motor [75, 76]. A local temperature gradient leads to the perturbation in the equilibrium of the surrounding medium, and self-propulsion occurs. For the other types of motors, acoustic motors obtain rotary motions from the acoustic energy of ultrasonic wave or ultrasound [77, 78, 79], and there are even thermally-driven motors [80].

Perspective of Chapter 2

There are several reviews about micro-nano-motors with a broad scope [44, 47]. In particular, optically-driven plasmonic nanomotors have also been reviewed [32]. However, these works focused only on motors enhanced by plasmonic resonances. Distinctively, I focus here on physical platforms that convert light energy into rotational momentum in a range from fundamental momentum exchanges to plasmonic enhancement at the micro- nano-scale and I provide a comprehensive understanding of optically-driven motors and relevant light properties. This chapter is not aiming at describing all the details of optical torques but at giving a manifest view of the distinct properties of optical motors and their applications. Although the descriptions are provided at a fundamental level, they offer fascinating insights into essential approaches for realizing optically-driven motors, as well as the advances to this day. This chapter will be helpful for newcomers in the field of optical motors and researchers in optical manipulation, micro-fluidics, biology, and chemistry.

2.2 Linear momentum

2.2.1 Linear momentum of light

One of the first recorded observations of the linear momentum of light was carried out by a German astronomer, Kepler in the 17th century. He made the assumption that a comet passing by the earth is gradually obliterated by sun light based on the fact that the tails of a comet extend off toward the opposite direction of the sun [81]. A comet mainly consisting of ice, methane, and ammonia appears in the sky every 76 years: Halley's comet, named after the person who found it. A comet in space has an orbital movement around the earth. It has two tails that are off the path of the orbital movement. The first tail, which consists of ion gases, always linearly stretches out toward the opposite direction to the sun. This is because the solar

winds, composed of charged particles such as electrons and protons, are emitted from the surface of the sun due to the solar corona at speeds up to 750 km/s and electromagnetically pushes away the charged ions on the comet [82]. On the other hand, the second tail is made of dust and is electrically neutral. The radiation pressure of the sun light nudges a fraction of dust. The dust particles retain their initial forward motion and result in a more curved tail than the ion tail since forces generated on the neutral dust particles by the radiation pressure, which is proportional to the linear momentum of light, are not as strong as the Lorentz forces on the charged particles.

Linear momentum and energy

The derivation of the momentum of a photon can be conducted in the framework of the special relativity [45], using the momentum p and energy E relation, $E^2 = (pc)^2 + (m_0c^2)^2$, where m_0 is the invariant mass and c is the speed of light. Since a photon has no mass, the second term including m_0 vanishes. The momentum, then, is expressed as the energy over the speed of light $p = \frac{E}{c}$. For a photon, the energy is proportional to the frequency f with the proportional constant being the Planck's constant h. Introducing the wavelength λ [45], the photon momentum becomes $p = \frac{h}{\lambda}$.

We now introduce the Ponyting vector **S** of a photon, which represents the energy flux of an electromagnetic wave and is directly proportional to the momentum flux $\mathbf{S}/c$ [83], and appears in the Poynting theorem [84]. According to the Poynting theorem, which represents the energy conservation law, the change of energy density u over time is equal to a combination of the divergence of the energy flux and the inner product of the total current density **j** and the electric field **E**, $\frac{\partial u}{\partial t} = -\nabla \cdot \mathbf{S} - j \cdot \mathbf{E}$.

In vacuum, there is no current density so the variation of energy u is equal to the divergence of the Poynting vector. The Poynting vector represents the directional energy flow per unit area, which is derived from the outer product of the electric field and magnetic field, $\mathbf{S} = \mathbf{E} \times \mathbf{H}$ [83].

The Poynting vector **S** is linearly proportional to the linear momentum density **g** with the proportional constant, $1/c^2$. The momentum density is the momentum of light per unit volume [45, 83]. The linear momentum density is given by $\mathbf{g} = \mathbf{E} \times \mathbf{H}/c^2 = \mathbf{S}/c^2$.

When light propagates from free space to a dielectric medium, the momentum of light changes due to the difference of the refractive index between free space and the dielectric medium. About 100 years ago, a disagreement arose on the interpretation of this momentum change – the so called Abraham-Minkowski controversy. Abraham anticipated that the linear momen-

tum of light decreases when it enters a dielectric medium [85], while Minkowski predicted it increases [86]:

$$\mathrm{p}_{\mathrm{Abr}} = \frac{\hbar\omega}{nc} \quad \text{and} \quad \mathrm{p}_{\mathrm{Min}} = \frac{n\hbar\omega}{c}, \tag{2.1}$$

where $\hbar$ is equal to h divided by 2π, ω is the angular frequency and n is the refractive index of the medium. Experiments have been conducted to clarify the controversy [87, 88, 89, 90]. They found that the experimental results supported both previous predictions. Theoretical analyses were also examined to interpret the mechanism. The energy-momentum tensor in the medium can be calculated by reversing the order of the Lorentz force [91]. The analysis of the radiation pressure experiment elucidated how momentum is transferred to the medium and divided into electromagnetic momentum and co-traveling mechanical (or canonical) momentum of the medium [87, 83, 92]. A quantum perspective was also applied to analyze the effective momentum of light in dielectrics [93, 94]. A hybrid momentum density, $\mathbf{g}^* = \frac{1}{2}\mathbf{D}\times\mathbf{B} + \frac{1}{2}\mathbf{E}\times\mathbf{H}/\mathrm{c}^2$, was also suggested [95]. The theoretical analysis proved that the net momentum in the world is conserved and both Abraham and Minkowski descriptions are equivalent [96]. The origin of the controversy lies in the fact whether the mechanical momentum of the medium is considered [97].

Momentum transfer in the form of radiation pressure

A photon carrying linear momentum reaches the surface of an object and exerts radiation pressure, $\mathrm{P}_{\mathrm{rad}}$, by which the radiation pressure force is generated [83]. The force caused by the photon moves the object and the object subsequently gains linear momentum in the same direction as the incident photon has. The Poynting vector of photon indicates the radiation pressure. Given the speed of light is constant, the Poynting vector becomes the force $\mathbf{F}$ times the speed of light per unit area A:

$$\mathbf{S} = \frac{\mathbf{F}\Delta x}{\Delta t \mathrm{A}} = \frac{\mathbf{F}}{\mathrm{A}}\frac{\Delta x}{\Delta t} = \mathrm{P}_{\mathrm{rad}}\, c. \tag{2.2}$$

The radiation pressure, $\mathrm{P}_{\mathrm{rad}}$, can be calculated by dividing the Poynting vector by the speed of light c. The time-averaged Poynting vector, $\langle\mathbf{S}\rangle$, is applied to avoid the consideration of instantaneous fluctuation in time. The radiation pressure with an absorbing object can be rewritten as $\mathrm{P}_{\mathrm{rad}} = \langle\mathbf{S}\rangle/\mathrm{c}$. The radiation pressure doubles when the absorbing material is replaced with perfectly reflecting material. When a mirror-like material reflects the light, the same amount of radiation pressure as that of the incident light is added due to Newton's third law.

One of the early experiments in lab to observe the radiation pressure exerted by linear momentum of light was performed by Nicholas and Hull in 1901 [98]. In the experiment, a pair of perfect absorbing plates are suspended on the ceiling via a quartz fiber in a vacuum chamber. One of the plates is illuminated by light as shown in Fig. 2.1**a** and starts rotating as if it were pushed by a hand. When the other plate is illuminated, the same effect occurs and maintains the plates rotation. This experiment reveals the existence of linear momentum for light. The Lorentz force cannot play a role, since the plates are electromagnetically neutral. Light that reaches one of the plates exerts radiation pressure on the surface. When the absorbing plates are replaced with perfectly reflecting mirrors, the radiation pressure doubles with reflecting surfaces since the same amount of the reflected light's momentum is added.

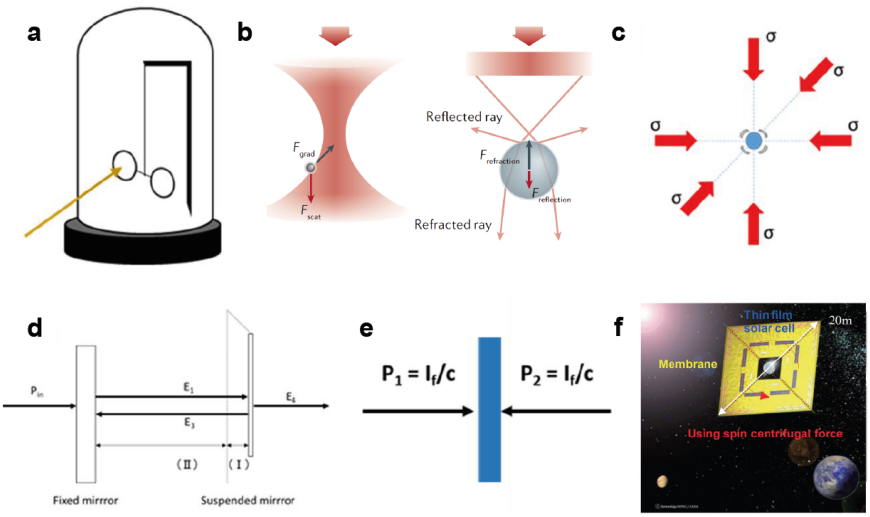

Figure 2.1: **Examples of applications of linear momentum of light. a**, Radiation pressure experiment done by Nichols and Hulls [98]. Two mirrors are suspended on a string in a vacuum chamber. One of the mirrors is illuminated by light and rotates through the radiation pressure. **b**, Schematic of the optical tweezer mechanism when a laser is highly focused onto a trapped particle [99]. The particle is trapped at the location where the gradient force and the scattering force are balanced. **c**, An atom is laser-cooled by light illumination from 6 directions. The vibrational (thermal) energy is canceled out by the momentum of light. **d**, Radiation pressure-driven interferometry: a light mirror is suspended in the pendulum and moves by the radiation pressure [100]. The length change in the system introduces nonlinearities. **e**, Schematics for stationary radiation friction . **f**, Schematics of a solar sail: a wide and thin mirror-like sheet connected with a spaceship reflects the sun light and generates the radiation pressure on its surface [101]. The spaceship acquires the linear momentum for propulsion.

Applications of the linear momentum of light

The optical trapping mechanism can be explained by momentum exchange in ray optics when the diameter of a trapped particle is much larger than the wavelength of trapping light [102, 1].

A spherical particle is located on the z-axis, the refractive index of the particle is larger than that of the surrounding medium and the particle is illuminated by focused incident light propagating toward the positive z-direction (Fig. 2.1**b** (left). The actual position of the particle is slightly above the focal spot, where the net force balances the scattering force. Once a ray of the incident light reaches the surface of the particle, it forms an incident angle with the normal at the point where the ray arrives on the particle, as shown in Fig. 2.1**b** (right). Subsequently, the ray is refracted further toward the z-axis due to Snell's law. The refracted light contains a higher azimuthal component in momentum toward the center of the particle. In order to satisfy the conservation law, the particle acquires the azimuthal component in the opposite direction as well as the radial direction. A net force exerted by the momentum change is toward the focal spot. When the particle is located above the focal spot, the momentum change brings the particle back to the focal spot. When the diameter of the trapped particle is smaller than the wavelength of the trapping light, the particle behaves like a point dipole [102, 103]. As before, the scattering force moves the particle in the direction of light propagation. Furthermore, optical forces can be enhanced in the vicinity of an optical resonance, leading to resonance radiation pressure.

The principle of laser cooling is that the momentum transfer of a photon onto an atom either heats the atom or offsets the vibrational movement. Since the motional energy and the thermal energy of the material are synonyms in this case, the atom loses temperature down to mili-Kelvin [104, 105]. The vibrational movement of the atom is not in one direction, so the laser cooling is realized with 6 lasers to cover all the directions, as illustrated in Fig. 2.1**c**. A light mirror suspended in an interferometry system can be pushed by the radiation pressure and stay at the equilibrium point between the radiation pressure force and the gravity force (Fig. 2.1**d**). When the length in the interferometer changes, the internal field varies and introduces nonlinear effects such as optical equilibrium bistability and multistability [100, 106]. Radiation friction can also be realized by the radiation pressure, as was already suggested by Einstein in 1909 [107, 108]. Consider a plate where constant radiation is incident into the normal direction from both sides of the plate. When the plate is stationary, the same amount of radiation pressure occurs on both sides as shown in Fig. 2.1**e**. However, if the plate moves at a constant speed in the direction perpendicular to the surface, it produces stronger radiation pressure on the front side (toward the direction of movement) compared to the backside. Accordingly, two different forces magnitudes in opposite directions are generated on the plate back and front and a net force slows the plate down; this net force is stronger with higher speed.

In 1970, Carl Sagan asserted that the radiation pressure exerted by the sun could enable the concept of solar sailing [81]. According to his explanation, a spaceship with a wide and thin mirror, which reflects photons from the sun, experiences the radiation pressure, gains linear momentum and can travel in space without any fuel for propulsion (Fig. 2.1**f**). This has many advantages such as low cost, long lifetime, constant sun light, cumulative effect over time, and orientation of the spacecraft [109]. For example, the total energy generated by the radiation pressure of sun light is close to the propulsion by electric engines: a 800 x 800 m^2 wide reflecting sheet located as far from the sun as the earth produces 5 N for propulsion [110]. The first practical application of this technology is IKAROS, which was sent to space in 2010 [101, 111].

2.2.2 Micro- nano-motors driven by linear momentum of light

The linear momentum of light and the radiation pressure have been reviewed in the previous section. This section introduces methods of generating rotational motions by means of linear momentum of light through micro- nano-motors and various examples with comprehensive understanding. Even though there is no angular momentum in the incident light, the rotational movements of nano- micro-structures can be realized by such optical effects. In other words, the redirection of the light momentum drives the rotational momentum in the object. Such motors are indicated as "LM" type in Table. 2.1, where their rotation speed is indicated.

Planar motors larger than the wavelength

Dielectric motors at the microscale have been explored with the advent of microfabrication technologies [25, 18, 27]. The rotation mechanism can be explained by the refraction or reflection in ray optics. The geometry of the motors with respect to the rays of the incident light and the difference of the refractive index between the motor and the surroundings govern the momentum exchange and cause the optical force. When the optical force is generated, the viscous drag force of the surrounding medium hinders the motion accordingly. At the steady state, a damping term with the viscosity in medium determines the rotation speed for a given optical torque. The rotation speed is linearly proportional to the laser power.

As an example of refraction motors, a cross-like shape micromotor made of fluorinated polyimide (refractive index: 1.53 at 1064 nm) was fabricated by EBL and reactive ion etching [25] (Fig. 2.2**a**). Ethanol (refractive index: 1.36 at 1064 nm) was selected as the surrounding medium. A high NA oil-immersion objective (100X 1.25NA) is used to increase the transverse component

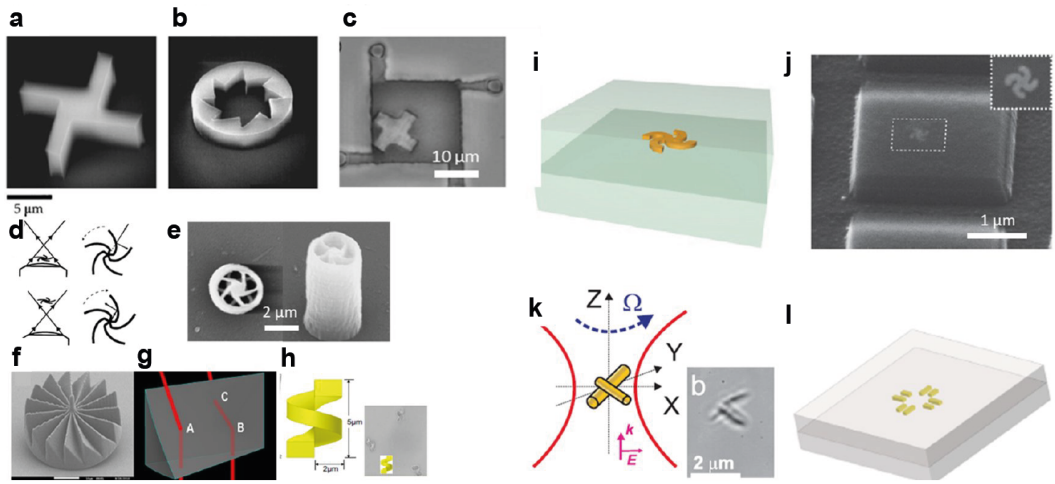

Figure 2.2: **Examples of 2D and 3D micro- nano-motors are presented.** SEM images of low-relative refractive index (**a**) and high-relative refractive index (**b**) motors fabricated by RIE [25]. **c**, A ship-in-a-bottle motor stays in a micro cavity after femto-second laser-assisted etching [112]. **d**, Two-photon polymerization-made spiral motor [18]. It has two handednesses that generate torques in the opposite directions. **e**, The two spiral motors from **d** are extruded and jointed [113]. **f**, 3D turbine-like motor fabricated by two-photon polymerization [114]. It generates a helical wavefront from a plane wave. **g**, The optical torque generation mechanism in **f** can be explained by refraction and reflection in ray optics. **h**, Two-photon polymerization realizes a 3D Archimedes microscrew motor [27]. **i**, Schematic of a gammadion plasmonic motor embedded in a SiO_2 microplate [23]. **j**, SEM image of **i** on top of a SiO_2 plate. The motor is fabricated by EBL and isotropic etching. **k**, Schematic and SEM images of Au aggregate showing rotational movement under linearly polarized light [29]. **l**, 4 pairs of Au nanorods embedded in SiO_2 plate [115]. Each of them scatters the incident light unidirectionally.

of the incident light while the longitudinal component exerts the axial force to hold the motor's position. The refraction of the transverse components redirects the radiation pressure of the incident light and generates the optical force on the side surface. Subsequently, the sum of the optical forces generates a rotational torque. The rotational speed is 80 rpm under 120 mW illumination. On the other hand, another motor is suggested as an engraved saw-like shape motor whose inner part is empty, and the ring part has a lower refractive index in Fig. 2.2**b**. When the engraved saw-like motor rotates, Cargille immersion liquid (refractive index: 1.61 at 1064 nm) replaces Ethanol. The engraved saw-like motor avoids the simultaneous trapping of many objects: it presents stable trapping for a long term without gathering other objects, because the intensity maximum appears at the center of the motor. The refraction of the transverse component of the incident light manly happens on the side walls rather than the center body. According to the Gaussian beam profile of the transverse electric TEM_{00} mode, the center body that has no contribution to the optical torque is illuminated by the strongest intensity. The TEM_{00} mode is replaced with the $TEM_{01}{}^*$ mode to enhance the rotational speed,

which has the highest intensity over the beam profile rim. The TEM_{01}* mode exerts higher rotational speed with the same laser power. Another example of dielectric planar micromotors is shown in Fig. 2.2**c** [112]: a femtosecond laser-assisted etching realized SiO_2 motor which is rotating in water. On the other hand, motors can also take advantage of reflection to realize rotational motion [18, 26]. To to do, the two-photon polymerization technique was applied to produce complex shapes [116]. The polymerization leads to a glass-like material with a refractive index of 1.56. It has two different parts, the first one is a round and relatively bulky part for trapping and the second one becomes a thin spiral for the reflection of light. The rotation direction depends on the handedness of the spiral part and its position within the trap site, as shown in Fig. 2.2**d**. The high NA objective is required to maximize the transverse component of the incident light. There is probable friction between the glass substrate and the rotor, which slows the rotation speed, when the motor is pulled by the focal spot and closely approaches the substrate. Even though it has a 3D structure, the torque generation occurs in the 2D spiral part. An extruded planar structure has also been realized as twin spiral blades [113]. Two-photon polymerization by a mode-locked laser was used to fabricate this motor shown in Fig. 2.2**e**. As we have seen for the previous motors, the handedness of a motor with respect to the relative position to the focal center decides the rotational directions. When the center of the motor between two blades is trapped at the focal spot of the laser, the two blades that have the opposite handedness can rotate in the same direction. Compared to a single blade motor, the twin blade motor shows improved speeds. A cylindrical structure that wraps the motor blades is added to generate a continuous unidirectional flow, which reduced the rotation speed by almost half.

3D Motors larger than the wavelength

In 2D planar motors, the torque generation mechanism was explained by the transverse component of light. 3D motors can generate further enhanced optical torques due to the extended degree of freedom in geometry. A 3D turbine-like spiral shape motor is realized by two-photon polymerization [114] (Fig. 2.2**f**). The size of the motor is around 30 µm. The driving mechanism is realized by refraction and reflection occurring in a single helicoid. Figure 2.2**g** shows that the refraction on the helicoid and the vertical backside and the helicoid's internal reflection generate the optical force to rotate the motor. The momentum conservation can also explain the torque generation mechanism. The spiral phase plate structure of the motor converts a plane wave passing through it into a helical wave, which carries orbital angular momentum (OAM). The rotational speed reaches the highest value when the incident plane of light corresponds to the cross-section of the motor. At this time, the conversion of light into the

torque can be maximum with minimum waste of light. The rotational speed was 500 rpm with 200 mW in laser power when a 40x objective was used. A 3D Archimedes microscrew motor consisting of cylindrical stairs is presented in Fig. 2.2**h** [27]. The two-photon polymerization technique was used to realize the motor. The radius of the motor is 2 μm, and the height is 5 μm. The momentum change due to reflection provides optical torques. This conversion occurs simultaneously in all directions due to the cylindrical shape. This also gives the motor the same orientation as the optical axis after being trapped; without the incident laser, the motor has an arbitrary orientation. The rotational speed was 40 Hz with 200 mW of laser power.

Motors smaller than the wavelength including plasmonic enhancement

Light refraction and reflection in ray optics have been employed to explain the torque generation when the motor is larger than the incident light wavelength. But, in the Rayleigh regime, when the motor has a smaller size than the wavelength, the rotational mechanism must be described by light scattering. When a linearly polarized incident light illuminates a specific nanostructure, owing to its geometry, it is possible that the nanostructure scatters light carrying angular momentum and, to satisfy the conservation law, torques are exerted on the structure. This light scattering can be further enhanced by the surface plasmon resonances that provide new opportunities in designing optical applications such as nanomotors [23], antennas for optical trapping [9], nanorod metamaterials for biosensing [117], and nanoparticles with tunable resonances that depend on shapes [118]. Therefore, optical torques exerted on objects can be further enhanced at plasmonic resonances [31, 33, 22].

For example, a gammadion Au nanomotor has been demonstrated [23]. It causes the phase retardation of the scattered light, which means that the re-emitted light carries OAM and, as a result of the momentum's conservation low, the motor obtains a torque. The motor consists of four branches in which the geometry and optical properties of metal determine the resonance frequencies, as shown in Fig. 2.2**i**. When light at a resonance frequency illuminates it, a plasmonic mode is formed and induces phase retardation between the surface currents [119, 120]. Subsequently, OAM is impressed onto the scattered light and the motor rotates accordingly. Plasmonic enhancement is observed as a function of wavelength in the electric field enhancement. The spectral maximum torque positions also coincides with the enhancement position. In particular, the rotation direction can be changed as a function of the different plasmonic modes excited. The local electric field distribution and the time-averaged Poynting vectors indicate the dependence of the rotation direction. In the gammadion motor, the plasmonic

resonance at 810 nm generates the rotational movement anticlockwise, and another resonance mode at 1700 nm rotates the motor in the opposite direction. The nanomotors are embedded in the SiO_2 microplates; Fig. 2.2**j** shows that the motor is on top of the SiO_2 plate in the middle of the fabrication process. One motor generates enough torque to rotate the entire body, which is 4000 times larger in volume. The rotational speed is 0.3 Hz with 1.0 mW/μm^2 laser power density. Multiple motors can also be implemented in the same microplate and exert a combined torque, although the latter is not linearly proportional to the number of motors because inner torques are canceled out in this case.

Asymmetrically combined Au nanorods can generate optical torques with plasmonic resonances as a nanomotor [29]. Figure 2.2**k** shows the schematic of Au aggregate with incident light. The anisotropic scattering of the aggregate causes the rotational movement when the incident light is linearly polarized. The rotational frequency is calculated as 16.16 Hz with 15 mW. As another example of asymmetric shapes for rotation, Au aggregates, fabricated by pulsed laser ablation, also exhibit a rotational motion[121]. The rotational movement is caused by the asymmetric shape, which generates anisotropic light scattering.

A combination of unidirectional light scattering units gives rise to rotary motion with plasmonic modes [115]. A pair of nanorods is detuned to have dipolar resonances and scatter unidirectional light, which generates lateral optical forces. For the rotational behavior, four pairs of nanorods are implemented in cardinal points and generate torques as shown in Fig. 2.2**l**. The rotational speed is 0.25 Hz with 2.0 mW/μm^2 in laser power density.

Rotational movement with alignment

Some other nanoparticles align with respect to the polarization of light, even though they cannot create rotational motion by themselves [122, 123]. They exhibit a plasmonic resonance and align in the direction that lowers the total optical potential energy. When a circularly polarized light beam is introduced, the alignment nanoparticles are repelled toward the minimum of light intensity [30]. Rotational motion can also be created by orienting the polarization direction of the incident lights. When the particles are absorbing, circularly polarized light can transfer the angular momentum to the particles. Moving the focal spot along a round trajectory enables a trapped part to rotate, for example to control the flow rate in micro-fluidics [124].

2.3 Spin angular momentum

2.3.1 Spin angular momentum of light

The spin angular momentum (SAM) of light is described in this section. Circularly polarized light is the most well-known example of light with SAM. The generation and transfer of SAM are briefly explained; our purpose is not to look at details in the quantum-mechanical description but to provide the prior knowledge for the next section on micro- nano-motors driven by SAM. Experiments to prove the existence and transfer of SAM are also introduced.

Circularly polarized light in classical electromagnetism

The electric field oscillates with a constant frequency in general. The x- and y-components of the electric field can have phases independent of each other when the field propagates along the z-axis [45]. We can first think of the superposition of x- and y-components with different amplitudes but the same phase. In this case, we have a linearly polarized oscillating electric field. The orientation of the linear polarization depends on the amplitudes. When the x- and y-components reach their maximum and minimum values simultaneously, they are in phase. When the phase difference between the x- and y-components begins to occur, the electric field takes an elliptical shape in a plane perpendicular to the propagating direction. In the particular case where the x- and y-components have the same amplitude and a phase difference of $\pi/2$, the electric field shows a circular pattern, indicating that the light is circularly polarized [83].

SAM and its transfer mechanism to an object

According to the quantum-mechanical point-of-view, the constituent parts of light are photons. When the light is circularly polarized, each photon carries SAM $\sigma = \pm\hbar$ [83]. The quantity of SAM is $\hbar$, the reduced Plank constant, and the sign, $\pm$, is determined by the polarization handedness. The SAM direction, $\pm\hbar$, is parallel to the propagation direction. The positive value, $+\hbar$, means the SAM has the same direction as the light propagation, and the negative one, $-\hbar$, is in the opposite direction, as shown in Fig. 2.3**a**.

The angular momentum of circularly polarized light can be transferred to an object. Electrons bound to the substance move in a circular motion due to the Lorentz force exerted by the rotating incident electric field. The angular velocity, ω, of the electrons follow the light frequency [125], while the torque generated by the magnetic field vanishes. In order to investigate

the relation between the energy and the angular momentum, the power transferred from the light to the substance is considered. The power is the derivative of energy, E, with respect to time. Simultaneously, the power on an object in rotational motion is a torque time angular velocity. So the relation can be written as:

$$\frac{d\mathrm{E}}{dt} = \omega\tau, \tag{2.3}$$

where τ is the optical torque and J is the total angular momentum of light. The optical torque corresponds to the time derivative of the angular momentum, $\tau = \frac{d\mathrm{J}}{dt}$. The energy is linearly proportional to the angular momentum with ω as the constant of proportionality. When the energy changes over time, the angular momentum also changes. This means the angular momentum can be obtained when it absorbs energy from circularly polarized light. The rate is given by:

$$\mathrm{J} = \frac{\mathrm{E}}{\omega}. \tag{2.4}$$

When a charged particle emits or absorbs light, it undergoes an angular momentum exchange of $\pm\hbar$ as well as energy and linear momentum exchange.

It is also possible to generate a rotational movement within a birefringent particle by introducing a circularly polarized light. The birefringent particle can be considered as a half-wave plate with a suitable thickness and wavelength. The half-wave plate particle can alter the handedness of circularly polarized light [19]. While changing the handedness of circularly polarized light, the particle obtains a corresponding angular momentum to satisfy the momentum conservation law [21].

SAM transfer experiments

Since the SAM of light was confirmed experimentally, researchers have conducted experiments to prove the transfer of SAM to an object. An investigation on the light scattering by gases proves that photons can contain intrinsic spin in addition to energy and momentum [126]. An absorbing shaft is constantly revolving under illumination by a circularly polarized light beam, which indicates the transfer of angular momentum [127] (Fig. 2.3**b**). The conservation law in angular momentum has been confirmed by observing the angular momentum transfer through a half-wave plate [19](Fig. 2.3**c**). Torques can be exerted on an absorbing particle by the transfer of SAM [128]. A photon carrying SAM enables the excitation of an electron spin through the SAM transfer [129]. Even light propagating in a waveguide can carry SAM [130].

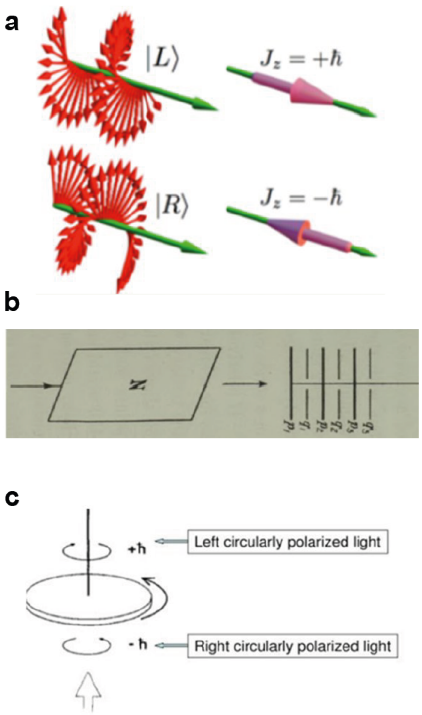

Figure 2.3: **Examples of SAM of lihgt. a**, Rotating electric fields in two different handednesses. The positive value of SAM, $+\hbar$, is in the direction of the propagation (left-handed circular polarization). The negative value of SAM, $-\hbar$ has the opposite direction to the propagation (right-handed circular polarization) [131]. **b**, A steel shaft revolves at a constant speed under illumination by a circularly polarized beam [127]. **c**, SAM transfer from a circularly polarized incident light to a birefringent plate. The change of $+2\hbar$ in angular momentum introduces the opposite handedness in the transmitted light [19].

2.3.2 Micro- nano-motors driven by spin angular momentum of light

The SAM of light has been introduced in the previous section. In this section, the realizations of the rotational movement through the SAM of light are observed with various examples of micro- and nano-motors. We examine under which conditions this movement is possible and categorize them. Besides, we have a look at the principle of plasmonic enhancement effects on motors driven by the SAM of light.

Motors with an absorbing body

When an absorbing motor or particle absorbs a circularly polarized light beam, it rotates due to the transfer of SAM [132, 133, 28]. The transmitted light beam may lose somewhat circular polarization properties; it becomes linearly polarized when the angular momentum is completely transferred. Torques exerted on the motor depend on the light intensity and

the absorptivity of the motor at the wavelength of light. When a circularly polarized light is intensely focused, the absorbing motor can be trapped and rotated at the focus. If optically generated torques reach an equilibrium with the drag forces of the surrounding medium, the rotational movement becomes constant. The handedness of circularly polarized light induces the same rotation direction for the motor.

One of the early SAM motor experiments has been conducted on a CuO particle [132]. It had irregular shapes and sizes ranging from 1 to 10 μm. A thin 50 nm CuO film showed 30 % light transmission at 1064 nm. A linearly polarized light beam is polarized circularly by a quarter-wave plate, such that each photon possesses SAM. The beam is strongly focused by an objective lens and traps a CuO particle in the vicinity of the focal spot. The rotational frequency depends on the angle of the quarter-wave plate because the polarization quality requires a proper angle between the linear polarization and the fast axis of the plate.

The transfer of SAM can also be observed with 2D arrays of polystrene (PS) beads [133]. The PS beads whose diameter was around 1 μm were immersed in water for the experiment, where the number of particles in the array was adjustable by varying the height of the stage. A circularly polarized light beam rotated the PS beads arrays, whereas a linearly polarized beam did not achieve the same. When circularly polarized light rotated the array, the transmitted light appeared to be unpolarized. It is clear that the SAM of light was transferred to the PS beads array and the conservation law of angular momentum was satisfied.

Au nanoparticles can also be considered as motors driven by absorbing SAM [28]. Colloidal Au particles of 400 nm in diameter showed the rotational motion under circularly polarized light illumination at the wavelength of 830 nm, Fig. 2.4**a**. The radiation pressure exerted on the surface of highly absorbing particles is strong enough to push the particles away against the gradient force. So, the particle cannot be levitated by a focused single beam. Instead, the focus of the laser is located near the cover glass within the chamber so that the displacement of the particle along the optical axis is hindered. Subsequently, the reverse glass prevents the particle from being pushed away and the particle rotates at a fixed position. The rotational frequency was measured by an avalanche photo diode with an autocorrelator and the rotational frequency increased with the laser intensity. The measurement results implied that higher laser intensity results in higher temperature, which reduced the viscosity and friction in water.

The optical torques exerted by the SAM of light were indirectly estimated based on the rotational speed of motors and the drag forces caused by the viscosity of surrounding media.

There was also an attempt of high accuracy direct measurement of optical torques using a magneto-optic manipulator [134].

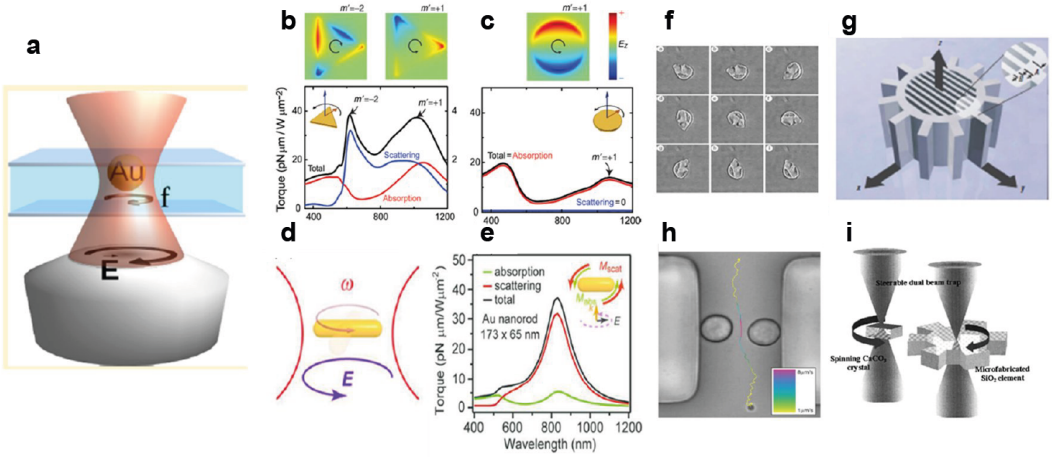

Figure 2.4: **Micro- nano-motors driven by SAM of light. a**, A spherical Au nanoparticle absorbs SAM and is set into a rotational motion [28]. **b**, A triangle-shaped flat motor has a torque peak from scattering due to multipolar resonances [31]. **c**, A round flat motor presents a dipole behavior and a torque from absorption while there is no contribution from scattering [31]. **d**, A focused circularly polarized light rotates an Au nanorod. The rotation direction follows the handedness of the light polarization [33]. **e**, Two torque contributions from absorption and scattering are shown, with a plasmonic resonance at around 810 nm [22]. **f**, A calcite particle converts the handedness of the polarization of the incident light and rotates at a constant rotational frequency [21]. **g**, A micromotor is fabricated from a 1D photonic crystal [135]. **h**, Two particles rotate in opposite directions to each other and control the flow in the middle [62]. The backflow is suppressed by covering the space between the particles and the wells. **i**, An engaged motor system is realized where the rotational torque is generated by the transfer from polarized light to a calcite particle and delivered to the neighboring SiO_2 micromotor [136].

Motors with both absorbing and scattering contributions

Two distinguishable contributions of absorption and scattering of light to the realization of optical torques have been analyzed, comparing round, triangular, and rectangular shapes thin Au nanostructures [31]. A circularly polarized light beam induces optical torques on the structures: the round one has continuous rotational symmetry, while the others show broken rotational symmetries, as illustrated in Fig. 2.4**b**, **c**. In the round shape, the scattering contribution to the optical torque is negligible; only torques from absorption are exerted. On the contrary, non-rotational symmetries such as triangular and rectangular shapes obtain torques from scattering as well as absorption. High order multipolar plasmonic resonances contribute to the scattering torques for the low symmetry nanostructures, while the round one shows only a dipole mode.

The theoretical analysis of Au nanorods, which show surface plasmon resonances and rotate under circularly polarized light, has been reported (Fig. 2.4**d**) [33]. The maximum torque generation occurs at the resonances, coinciding with the absorption efficiency, which implies some optical torques are induced by the absorption of photons carrying SAM. The optical torque efficiency is not linearly proportional with the absorption power, which means that scattering also contributes to optical torques. Localized surface plasmon resonances and extinction spectra are tunable by adjusting nanorods length [22]. Colloidal nanorods ranging from 130 nm to 170 nm in length with a width of 65 nm have been synthesized and the torque maximum corresponds to the resonances of both absorption and scattering (Fig. 2.4**e**). Here, the scattering contribution dominates the optical torque. As in the case of Au nanoparticles described previously, the heating due to extremely high power might change the viscosity and convection properties of the surrounding medium and lead to unstable rotations when a high power beam is used.

Motors with a birefringent body

In addition, birefringent particles can have rotational motion with circularly polarized light [21, 137, 62]. Refractive indexes of birefringent particles rely on the polarization and propagation direction of impinging light. A birefringent particle with a suitable thickness can be used as a half-wave plate for a wavelength. Half-wave plates can convert the handedness of circular polarization from left to right and vice versa. In order to observe the conservation law of the angular momentum, the SAM twice, 2σ, per photon is transferred to the wave plate. Likewise, birefringent objects can obtain the SAM, by converting the handedness of circularly polarized light. Unlike absorbing particles, transparent birefringent particles avoid the overheating issue.

When a birefringent and transparent particle, such as calcite, vaterite, or quartz, is optically trapped by a strongly focused and circularly polarized light beam, its optical axis becomes aligned with the trapping laser [21, 137, 138, 139]. Converting the direction of circular polarization, it rotates at a constant frequency (Fig. 2.4**f**). An anisotropy structure, like a 1D photonic crystal, acts as if it were a birefringent motor, as illustrated by the structure made of polymer and sculpted by EBL shown in Fig. 2.4**g** [135]. With a Wollaston prism, two counter motors can be realized and offer a promising concept for practical applications (Fig. 2.4**h**) [62]. An engaged micromachine consisting of a block of calcite and a SiO_2 micro-element has been demonstrated, which showed both the transfer of SAM to a matter and of the mechanical torque to another, as illustrated in Fig. 2.4**i** [136].

2.4 Orbital angular momentum

2.4.1 Orbital angular momentum of light

Linear and spin angular momenta have been elucidated in the previous sections. Here, OAM carried by photons and its applications are introduced. Regardless of SAM, OAM exists when a light beam has a phase distribution in its wavefront or in the cross product of the beam position from the optical axis and its linear momentum. OAM is a comparatively recent discovery; in a Laguerre-Gaussian mode in the paraxial approximation, the OAM exists independently of the polarization state. Since it has unique features, it has been suggesting promising applications for optical manipulation, nonlinear optics, telecommunications, and quantum mechanics.

Discovery of the OAM of light in the paraxial approximation

The linear momentum is h/λ per photon, according to the relativity equation [107]. Poynting recognized that the photon could also carry the SAM when a light beam is circularly polarized. Allen et al. discovered in 1992 that a beam with a helical wavefront contains OAM unrelated to the circular polarization, and the phase distribution in an azimuthal plane depends on $exp(il\phi)$ [140]. The topological value l can be any integer number and either negative or positive; the sign determines the OAM handedness. When l is equal to zero, the beam becomes a plane wave and the intensity profile follows a Gaussian beam pattern (Fig. 2.5**a**). If l takes any nonzero integer value, the intensity profile is transformed into an annular pattern which radius increases with l. A Laguerre-Gaussian (LG) mode is an example of a beam carrying OAM; its amplitude distribution in the paraxial approximation and given by [140]:

$$\begin{aligned} u_{pl} = \sqrt{\frac{2p}{\pi(p+|l|)!}}\frac{1}{w(z)}\left[\frac{r\sqrt{2}}{w(z)}\right]^{|l|} L_p^{|l|}\left(\frac{2r^2}{w^2(z)}\right) exp\left[\frac{-r^2}{w^2(z)}\right] exp(il\phi) \\ exp\left[\frac{ik_0 r^2 z}{2(z^2+z_R^2)}\right] exp\left[-i(2p+|l|+1)tan^-1\left(\frac{z}{z_R}\right)\right], \end{aligned} \tag{2.5}$$

where z_R is the Rayleigh range, $L_p^{|l|}$ is the Laguerre polynomial, k_0 is the wavenumber and $w(z)$ is the beam radius. The dependence of $exp(il\phi)$ indicates the existence of OAM in Eq. (2.5). Since its discovery, the OAM has attracted much attention because of its unique features such as quantization of the topological value, spatial phase distribution, interaction with SAM and its association with quantum mechanics [141, 142, 143, 144]. Analysis and works related to the OAM have been undertaken by many researchers [145, 146, 147, 148]. The study of Laguerre-Gaussian beam modes in the paraxial approximation could also be extended to

higher-order modes [149].

The main difference between SAM and OAM is that the former is related to polarization, and the latter is associated with the spatial phase distribution. This means that light carrying OAM can be polarized so that it has SAM at the same time. In optical trapping and rotation experiments [150], we can obtain practical insights through quantitative comparisons of SAM and OAM. Consider a beam carrying both SAM and OAM; when these two angular momenta have the same handedness and the same amount of momentum, $+\hbar$ and the beam is focused to trap a transparent particle, the rotational movement occurs by transferring the angular momenta. If they are set into opposite handedness to each other, the particle stops rotating. This experiment demonstrates that the OAM with $l = +1$, mechanically corresponds to the SAM with $\sigma = +1$ [150].

In addition to the paraxial approximation, researchers have made numerous efforts to obtain a non-paraxial vectorial beam solution for beams carrying OAM based on the full Maxwell theory [151, 152] and the vectorial Rayleigh-Sommerfeld formulas [153, 154]. Higher-order Bessel beams are another example of beams carrying OAM [155]. The Bessel beam is a non-diffractive beam during the propagation [156, 157]. This unique feature of non-diffraction enables optical conveyer belts [158]. Bessel beams can contain linear, circular, radial and azimuthal polarizations [159].

Various experimental methods can be used to generate light carrying OAM. Hermite–Gaussian (HG) modes can be modified into LG modes which carry OAM using $\pi/2$ converter [140]. It is also possible to change the handedness of OAM with a π converter [141]. This corresponds to the relationship between SAM and wave-plates. However, to create an LG beam with a higher amount of OAM, more complex HG modes have to be produced first, since each LG mode corresponds to one HG mode. Spiral phase plates can also produce a beam carrying OAM [160]. As mentioned above, OAM has a phase distribution in a plane perpendicular to the beam traveling direction and a spiral phase plate make this phase distribution continuous in the azimuthal plane. Therefore, the phase distribution becomes a multiple of the period according to the wavelength of light. Computational holographic methods like spatial light modulators (SLMs) can readily generate OAM of any l value from an incident plane wave [161]. The holographic image is made of the interference pattern of a plane wave and the beam to be created (Fig. 2.5**b**). This method is of high quality, reproducible, and can produce any desired phase and amplitude structures.

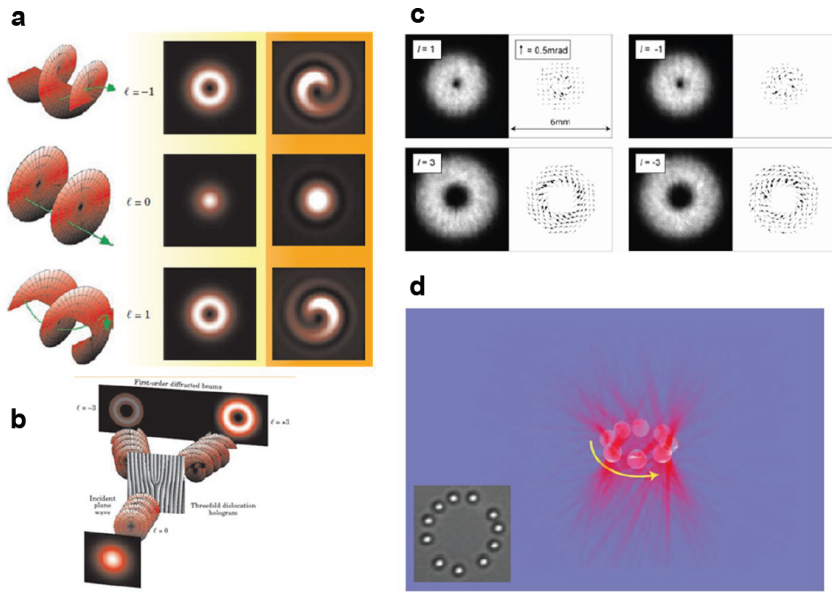

Figure 2.5: **Optical properties of optical angular momentum. a**, Phase profile, intensity and interference pattern with a plane wave are presented for l = -1, 0 and +1 [145]. Green arrows represent the Poynting vectors. When $l = 0$, the beam is a plane wave and the Poynting vector is parallel to the propagation axis. When l is not zero, the intensity profile becomes annular and the interference pattern has a spiral appearance. **b**, Hologram pattern made by SLM generates the first-order diffractive light carrying OAM from an incident plane wave [145]. **c**, Intensity profile cross-section and Poynting vector distribution indicating the angular momentum flow along the annular area [162]. **d**, A series of particles are trapped by a focused beam carrying OAM [163]. They are aligned along the intensity maximum and rotate in an orbital trajectory. The rotation direction follows the OAM handedness.

Poynting vector for a beam with helical wavefront

The origin, properties, and generation methods of OAM have been discussed so far. However, the spatial phase distribution and the annular intensity of OAM may not be sufficient to explain why this is one of the angular momenta. Although there are mathematical and analytical proofs [164], a more intuitive explanation is required. The Poynting vector, which is the cross product of the electric and magnetic field, depicts the direction and amplitude of energy flux, which also represents the momentum flow [145]. Each component of linear momentum density for an helical wavefront beam in the paraxial approximation can be given in cylinderical coordinates [142]:

$$p_r = \epsilon_0 \frac{\omega k r z}{z_R^2 + z^2} |u|^2, \qquad p_\phi = \epsilon_0 \left[\frac{wl}{r} |u|^2 \right], \qquad p_z = \epsilon_0 \omega k |u|^2, \tag{2.6}$$

where u is the complex amplitude and k is the wavenumber of light, while p_r converges to zero if the light is collimated. The skew angle, $y = l/kr$, between the azimuthal and longitudinal components of the Poynting vector indicates the OAM l per photon [162]. A continuous Poynting vector in a beam carrying OAM spirals along the propagation axis, while the azimuthal component results in the OAM and gives rise to the rotational movement when it transfers the OAM to an object (Fig. 2.5**c**).

Applications of OAM

Along with linear momentum and SAM, OAM of light can be transferred and set rotational motions into objects, as illustrated in Fig. 2.5**d** [163]. According to the azimutal components of its Poynting vector, the lowest order of LG mode has the momentum flow rotating around the optical axis. When this beam is focused to trap a particle, the annular intensity profile enables the orbital rotation moves. With higher OAM integer values, the radius of the profile and the amplitude of the Poynting vector increase. Interestingly, the LG mode beam can be circularly polarized and produce SAM on top of OAM [165]. This causes both intrinsic and extrinsic rotations on a birefringent calcite particle. This function has the advantage that it can be easily made with a quater-wave plate. The direct conversion from SAM to OAM is possible in inhomogenous and anisotropic media [143]. These two angular momenta can interact with each other and lead to various phenomena such as spin-Hall effects, spin-controlled shaping and spin-directional coupling [166]. These interactions can be enhanced by spin-based plasmonic effect in circular symmetric slits [167]. Using plasmonic vortex lenses, the SAM of incident light can be converted into the OAM of surface plasmons [168]. Spin-orbital coupling generates multi-patterned optical lattices through hexagonal-shaped slits [169]. A series of hexagonal slits produces plasmonic lattices in which SAM is converted into OAM [170]. The integer number l of OAM takes any value and can be encoded for telecommunications [171]. Such an OAM multiplexed system combines multiple beams carrying differernt OAM, which are superimposed and send the information to a detector in free space. Second harmonic generation with light beams carrying OAM enables also nonlinear effects: Two identical beams with OAM, $l = +1$, are introduced toward a dielectric crystal and produce an output beam which has OAM, $l = +2$, per photon to satisfy the momentum conservation law, which is known as up-conversion process. Likewise, down-conversion process is also possible: for example, a single beam can be converted into two lower-energy beams [145, 172]. In quantum mechanics, down-converted photons generated by the parametric down-conversion enable entanglements in both SAM and OAM [173]. In addition, the OAM entangled states can interact with plasmonic modes in transmission and are transferred into surface plasmons in

which the spatial modes are conserved [174].

2.4.2 Micro- nano-motors driven by OAM

This section introduces various micro- nano-motors that operate with angular momentum transfer from OAM light. As we have seen in the SAM section, light absorption and/or scattering of rotating bodies can be the main source for rotational forces. Motors rotated by OAM also have the same mechanism and show interesting rotational behaviors that reflect the unique features of OAM, such as the phase singularity, the quantized topological charge number, and the annular intensity distribution. Because of these characteristics, beams carrying OAM are also called optical vortex or helical-wave front beams. In addition, the role of plasmonic enhancement in motors driven by OAM is also examined.

Motors with an absorbing body

The z-component of the total angular momentum density per unit power for a LG beam can be calculated by $M_z = \frac{l}{\omega}|u|^2 + \frac{\sigma_z r}{2\omega}\frac{\partial|u|^2}{\partial r}$, where l is the topological index, $\sigma_z = \pm 1$ is for the handedness of the circular polarization, $\sigma_z = 0$ stands for linear polarization [140]. The ratio of the total angular momentum flux to the energy flux is J/cP = $(l+\sigma_z)/\omega$ in the paraxial approximation [142]. When the LG beam is tightly focused, the quantitative total angular momentum carried by the beam can be expressed as [175]:

$$\tau_z = \frac{\mathrm{P}}{\omega}(l+\sigma_z), \tag{2.7}$$

where P is the absorbed laser power. The angular momentum for a linearly polarized ($\sigma_z = 0$) LG beam is proportional to the power, P, as well as the topological index, l. Considering not only SAM But also OAM, the total angular momentum that a photon can carry becomes $(l+\sigma_z)\hbar$ [176]. The angular momentum of the LG beam can be transferred to objects and cause the objects to rotate. The transfer method determines the amount delivered and the rotation direction. When the LG beam is polarized, the σ_z value is no longer zero and the light obtains SAM at the same time. If the handedness of SAM is the same as OAM, the total angular momentum increases, as shown in Fig. 2.6**a** [177, 178].

In the conventional optical tweezer, the gradient force and the scattering force play major roles [2]. While the scattering force keeps pushing the particle, the gradient force attracts it toward the focal spot. The trapping position of the particle is determined from the balance of the two forces. Likewise, light carrying OAM, such as a LG beam and other optical vortex beams,

generates both gradient and scattering forces when tightly focused. Besides, the gradient force is directed toward the annular beam intensity and particles smaller than the annular ring are trapped and aligned along the ring. The azimuthal component of the scattering forces makes these trapped particles rotate along the ring [165]. On the other hand, in the case of particles larger than the beam spot, they are trapped at the optical axis of the beam, and spin in the beam axis similar to the effect of SAM [175, 176, 20, 163]. Additionally, since the annular shape of the beam intensity distribution exists in a relatively wide area, stable rotation is possible even for a combination of several particles (Fig. 2.6**b**) [179].

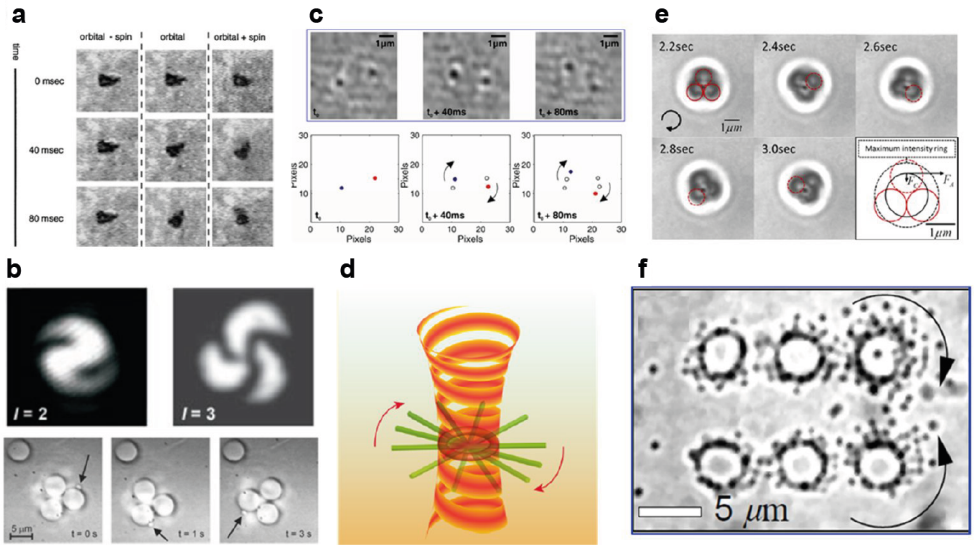

Figure 2.6: **Example of OAM-driven micro- nano-motors. a**, A 2-μm-diameter Teflon particle is rotated by OAM and SAM [177]. OAM always has a topological charge of l while SAM takes $\sigma = \pm 1$ or 0. **b**, SiO_2 beads, confined by an optical vortex beam, rotate in the same direction as the beam handedness [179]. **c**, Two Au nanoparticles are trapped within an annular beam and rotated by the angular momentum transferred from the optical vortex beam [180]. **d**, Schematic of a 10 μm rod rotating within an optical vortex beam [24]. The rotational axis corresponds to the center of the beam instead of the midpoint of the rod. **e**, A trimer consisting of Au particles (0.8 – 1.5 μm in diameter) is confined by an annular beam profile [181]. Light OAM is transferred to the trimer and gives rise to its rotational movement. **f**, Arrays of optical vortices are created by the holographic optical technique [182]. They trap and locate microspheres into the middle part of the array. Subsequently, the spheres unidirectionally move through the central path.

Motors with both absorbing and scattering contributions

Highly absorptive Au particles present unique features when trapped and rotated by a focused optical vortex beam [180, 183, 181] (Fig. 2.6**c**). The annular beam distribution of the vortex beam generated by the phase hologram can confine Au nanoparticles with a size of about

100-250 nm to the dark region inside the ring [180]. This confined region can be adjusted by modifying the wavelength or the topological charge value. These dark areas can also prevent particles from escaping by avoiding local heating. Particles of a specific size are trapped along the annular intensity ring and rotate following the handedness of the vortex beam. This indicates that we can selectively trap and rotate particles depending on their size. On the other hand, another experimental result shows that when the numerical aperture increases from 0.9 to 1.2 and the particle size doubles, the increased absorption cross-section allows more OAM to be transferred and more heat to be generated in the particles [183]. The generated heat helps to rotate faster by lowering the viscosity of the surrounding medium. The relatively large size makes trapping easier and enables stable manipulation. In addition, the wavelengths used for manipulation were at the plasmonic resonance, which substantially enhances the transfer of angular momentum.

A silver wire, whose length is 10 μm, becomes set into a rotational motion when illuminated with a linearly polarized optical vortex beam, as shown in Fig. 2.6**d** [24]. The rotation axis of the wire is determined by the optical axis of the vortex beam. The rotational speed increases with the topological charge. However, when the charge is $l = 1$ or 2, there is no rotational movement. There are two obstacles to rotating the wire: the drag force from the surrounding viscosity and unexpected plasmonic effects. As a result, the angular velocity of the wire has a dependency on the orientation and the rotational speed is suppressed when the wire is aligned with the direction of the linear polarization. This is because of plasmonic interactions that induce torques opposite to the momentum-transferred torque. For the realization of rotational movement, the optical torque needs to overcome the plasmonic interaction torque as well as the viscous drag torque. When the topological charger is larger than 2, the net torque becomes positive and the wire starts to rotate. The faster rotational frequency is demonstrated when the charge number increases.

A metallic trimer consisting of 0.8–1.2 μm particles can also be confined within the annular beam and rotate stably (Fig. 2.6**e**) [181]. However, since the metal particles outside the ring are strongly influenced by the repulsive force of the focused beam, a collecting method for each particle onto a specific place was employed. A conventional optical trapping is applied to place particles in a particular area. Subsequently, a focused vortex beam begins to trap and rotate the particles while the center of the particles matches the optical axis of the beam. When the vortex beam is switched off, the constituent particles are randomly dispersed by the Brownian motion.

OAM arrays for trapping

Besides the generation of OAM using holograms, it is also possible to locally develop OAM that plays the same role as a motor [182, 184, 185, 186, 170]. By making OAM arrays, particles can be moved mechanically, as shown in Fig. 2.6**f** [182]. Such local OAM can be generated by a phase plate [184], or by plasmonic metasurfaces [186]. Spin-orbital interactions are also used to generate OAM locally [170].

2.5 Summary

The fundamental principles of optically-driven micro- nano-motors have been described in this chapter, underlining the properties of light momenta and their interactions with micro-nano-objects. Over the last decades, progress in nanotechnology and nano-optics have enabled tremendous developments for motors in terms of their size and rotation speed. Various physical phenomena such as refraction, absorption, scattering, birefringence, and plasmonic enhancement have been explored for optical torque generation. In order to enhance the motors efficiency, cooperative platforms involving more than two rotary motion generation mechanisms would be desirable. For example, combining and maximizing SAM and OAM torques along with plasmonic enhancement can be performed in a single motor. In addition to blending the different mechanisms presented in this chapter, various physical benefits from other fields could also be implemented.

Artificial intelligence or machine learning has attracted much attention due to its promising ability to generate new images, nanostructures, or metasurface designs [187, 188, 189]. Researchers working on micro- nano-motors have tried many different structures but most of the time they are as simple as a sphere, rod, cross, gammadion, or random aggregate [28, 22, 112, 190, 121]. What if we apply machine learning for nanomotor design? With tremendous calculations, machine learning can suggest new structures with improved performances that are not just a mere geometrical optimization. The predictable limitation of this approach is the minimum resolution of the current nanofabrication technology. Actually, this is not a completely new idea in nano-optics and researchers have tried to improve nanoscale optical devices using machine learning [191, 34].

Metasurfaces possess very interesting applications in optical manipulation [192, 193, 194]. In particular, the ability to manipulate the direction of the reflected light is very useful to provoke transverse components in reflection for optically-driven motors. OAM can also be generated by metasurfaces [195]. Furthermore, SiO_2 sandwiched structures can contain any

nanostructure shape, even separated islands [115], this can prove a powerful approach to develop metasurfaces that generate strong optical torques.

New materials such as graphene that exhibit very promising nano-optical characteristics will probably lead to further improvements for optical micro- nano-motors [196, 197, 198]. Implementing graphene in nanomotors has not yet been discussed and systems that maximize the plasmonic enhancement and exploit the outstanding properties of graphene will certainly open new possibilities and interesting applications, different from those reported so far.

Table 2.1: micro- nano-motors

	Type	ref.	Shape	Size	Material	Obj NA	$\frac{\text{rpm}}{\text{mW}\cdot\text{um}^{-2}}$
1	LM	25	Cross	7.0 µm	Polymer	1.25	0.66
2	LM	112	Cross	11.7 µm	SiO_2	1.4	0.025
3	LM	18	Spiral	5.5 by 8.6 µm	Polymer	1.4	6.0
4	LM	113	Spiral	4.0 by 9.0 µm	Polymer	1.45	1.1
5	LM	114	Turbine	30.0 µm	Polymer		2.5
6	LM	27	Screw	2.0 by 5.0 µm	Polymer	1.25	11.6
7	LM	23	Gammadion	200 nm in SiO_2	Au	0.5	18
8	LM	29	Combined rods	200–500 nm	Au	1.3	64
9	LM	115	Parallel rods	200 nm in SiO_2	Au	1.2	1.87
10	SAM	132	Irregular	1–10 µm	CuO	100X	30
11	SAM	133	Aggregate	3 µm	Polystyrene	1.3	2.85
12	SAM	28	Particle	400 nm	Au	0.7	4580
13	SAM	22	Rod	200 nm	Au	0.7	115k
14	SAM	21	Particle	3 µm	Calcite	1.3	71.4
15	SAM	138	Particle	1.5–3.5 µm	Vaterite	1.3	68.5
16	SAM	137	Particle	1.0 µm	Quartz	-	81.0
17	SAM	135	Turbine	6.5 µm	Polymer	-	0.09
18	SAM	62	Particle	5.0 µm	Vaterite	1.3	-
19	OAM	175	Powder	1.0–5.0 µm	Al_2O_3	1.3	15–150
20	OAM	20	Particle	20.0 µm	CuO	1.3	70.5
21	OAM	112	Sphere	2.0 µm	Teflon	1.3	2.4
22	OAM	179	Sphere	1.0 µm	SiO_2	-	420
23	OAM	178	Particle	5.0 µm	Polystyrene	1.2	127
24	OAM	180	Particle	100–250 nm	Au	0.9	1.9
25	OAM	183	Particle	200 nm	Au	1.2	70.5
26	OAM	181	Particle	0.8–1.5 µm	Au	1.49	0.63
27	OAM	24	Wire	10.0 µm	Ag	1.2	0.67

3 Optically-driven Au nanomotor designed by machine learning

Some of the results in this chapter are in preparation for publication.

3.1 Introduction

The optical manipulation of microscopic/mesoscopic particles has been exploited vividly since the inception of optical tweezers in 1986 [1, 2, 17]. As one iconic example of mechanical systems operated by light, optically-driven micro- nano-motors have been realized by means of light absorption or scattering [44, 32]. Optical spinning motors, which convert light energy into rotation [32], have attracted significant attention due to their promising applications as biosensors [40], micro- nano-machines and robots [43, 41], micro- and nano-electromechanical systems [57] for microfluidics [60, 199] and nanoscale surgery [41]. Apart from optical rotors, self-propulsion motors driven by chemical [47] and magnetic [72] energy have also been widely studied for the environment [200, 201], drug delivery [202], lithography [42] and sensing applications [203].

The first scientific observation of optically-driven rotational movement has been demonstrated by transferring the spin angular momentum (SAM) of light to an absorbing material [19]. Since then, various absorbing optical motors have been explored [30, 28, 31]. Another example of harvesting SAM for rotation is birefringent particles that convert the handedness of the circularly polarized incident light and gain rotational momentum [21, 62]. On the other hand, light may also possess orbital angular momentum (OAM), which differs from SAM in that it is a property that stems from the spatial variations of the field rather than its polarization [140, 148]. Naturally, motors and manipulation applications based on OAM have also been widely studied, thus diversifying optical manipulations [182, 204, 181, 205].

At the same time, together with the developments of fabrication technologies at the microscale, the realization of non-absorbing optical micromotors has benefited from increased precision and design flexibility. For example, two-dimensional dielectric micromotors that rotate by refracting the azimuthal component of a focused beam have been fabricated by etching [25]. Additionally, three-dimensional motors have been realized with a significant degree of geometrical freedom at the microscale using two photon polymerization [113, 27].

Furthermore, the recent advances in nanofabrication [206] have enabled the realization of subwavelength features, especially in plasmonic metals [207, 3]. The resonant optical enhancement produced by plasmonic nanostructures has found many applications to enhance optical trapping [9, 3], absorption [208], scattering [209], fluorescence [210], spectroscopy [211] and heating [212]. It can also be applied to nanomotors such that the plasmonic modes drive the rotary motion [23, 213]. Plasmonic enhancement attributed to localized surface plasmon resonances (LSPRs) supports light scattering and absorption, which can both induce a force on the illuminated structure through momentum exchange [214, 215]. For the absorption, the amount of angular momentum transferred from the incident light to absorbing nanomotors depends on the LSPR properties of the nanomotors. Consequently, the rotational speed of SAM and OAM absorbing motors can be enhanced by plasmonic resonances [33, 24]. On the other hand, the geometry adjustment in a nanomotor allows the optical torque to be further enhanced by scattering [22]. In metallic structures, multipolar LSPRs can selectively enhance the conversion efficiency and make the scattering optical torque predominant [31]. When the scattering torque is stronger than the absorption torque, it is possible that the optical torque drives a nanomotor in opposite direction to the polarization handedness of the incident light [216]. Scattering torques are also favoured to avoid excessive heating. However, so far, the geometries that have been explored to induce strong scattering torques were based on intuitive designs such as rods [22], crystals [217], planar triangle structures [31], gammadions [23], or elementary spirals [216]; with a maximum optical torque reaching a theoretical value of 300 pN nm/mW μm^{-2} [216]. Here, we develop an appropriate method to overcome the limitations of intuitive designs and reach significantly higher torque values.

Thanks to the tremendous computational power that has been available since the middle of the 2010s, artificial intelligence has been able to tackle highly complex scientific tasks [218]. For example, machine learning has produced interesting results in fields such as big data analysis [219], medical diagnosis [220], image classification [221], natural language processing [222], and deep fakes in media [223]. Recently, machine learning algorithms have been used to design optical devices such as metagratings [224], nanoantennas for nonlinear op-

tics [225], optical tweezers [226], waveguides [227], periodic gratings [228], and dielectric color filters [229], demonstrating that machine learning algorithms can be successfully used in nano-optics [230, 191, 231]. With a sufficient amount of data and well-designed algorithms, the machine comes up with solutions as if it had physical insights [34]. Those solutions are not just optimized but expand outside of the dataset boundary. Although the results of machine learning are remarkable, one should keep in mind that transposing them to the real world represents another challenge due to the nanofabrication limitations.

In this thesis, plasmonic nanomotors which rotate under the illumination of linearly polarized light are designed by machine learning and experimentally demonstrated. A nanomotor consists of a gold (Au) planar nanorotor and a SiO_2 embodiment. First, we use machine learning algorithms to design nanorotors with exceptionally high torques. A torque predictor made of CNN [232, 233] is connected to a DCGAN [187] nanorotor generator, to compose the nanorotor structure generator. The SIE method is then used to study the electromagnetic properties of the proposed nanomotors, especially their optical torque [234, 235]. After an extensive nanofabrication optimization process to reach the level of details associated with the designed nanostructures, the most promising nanomotors are fabricated and characterized experimentally.

3.2 Nanomotor structure design using artifical neural networks

3.2.1 Methods

To generate nanorotors with higher torques beyond intuitive human insight, machine learning algorithms were built based on well-known CNN and DCGAN, and optimized in accordance with the goal. This work has been done with Tensorflow on Google Colaboratory, which is a cloud-based Jupyter notebook environment on GPUs (NVIDIA Tesla P100 PCIe and T4). An initial random dataset consisted of 4'400 pairs of blade images and their torque values (see the "Random dataset geometry" section in the Methods). SIE was dedicated to calculate their torques (see the "Numerical analysis with SIE" section in the Methods). A torque predictor constituting CNN was trained to have the ability to predict a torque value from an input blade image. After that, the predictor evaluated torque values of newly generated blades in DCGAN. The evaluation influenced the minimax game as the third loss function, forward loss, along with the conventional discriminiator and generator loss functions. After the training, output nanorotors statistically revealed the improvement of optical torques under illumination as well as rotor-like shapes.

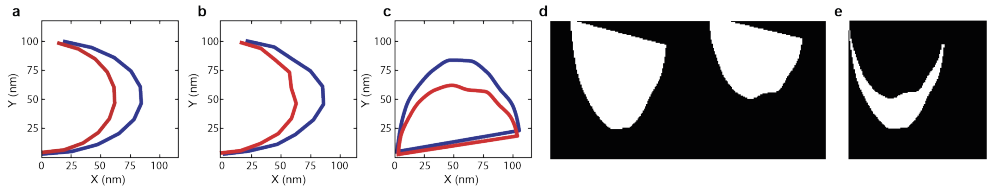

Figure 3.1: **Original geometry from the random dataset. a**, Example of a pair of ellipse plots (red and blue curves) originated from random coefficients. **b**, Roughness is randomly added to both curves. **c**, Curves are closed, reconfigured, and smoothed. **d**, Interpolygons of the two curves are selected, flipped, and aligned. **e**, The difference between both polygons produces a random blade shape.

Random geometry generator The random dataset used for the machine learning training is made of random spiral shapes. The spiral shape is achieved by subtracting two different ellipses with arbitrary sizes and roughnesses. To reach the required geometrical degree of freedom, uniformly distributed random numbers (function rand(), MATLAB R2018b [236]) have been used for the used to define the ellipse parameters. First, two random coefficients are set as

$$\begin{aligned} a_x &= a_0 + r a_0 \\ a_y &= 2a_0 + r a_0, \end{aligned} \tag{3.1}$$

where r is a random number between 0.0 and 1.0, and a_0 is the constant number 3×10^{-7}, which corresponds to the rough nanorotor dimensions we are aiming at. These coefficients define the ellipse in the x–y plane:

$$\begin{aligned} x &= a_x \cos(t)\cos(\theta) - a_y \sin(t)\sin(\theta) \\ y &= a_x \cos(t)\sin(\theta) + a_y \sin(t)\cos(\theta), \end{aligned} \tag{3.2}$$

where θ is the ellipse tilt-angle, and t is $N r\, t_0$, t_0 is a random angle between 9° and 18°, $N \in \{1, 2, ..., 10\}$. Two ellipses with different random coefficients are set (Fig. 3.1**a**). To include roughness, the ellipses are further modified using random functions as detailed Fig. 3.1**b**:

$$\begin{aligned} x' &= xv - 0.1\, r a_0 \\ y' &= xy - 0.1\, r a_0. \end{aligned} \tag{3.3}$$

Subsequently, a spline interpolation renders the elliptical curvature smooth, and the curvature is closed by connecting the initial and final points. Two elliptical curvatures are rearranged and aligned (Fig. 3.1**c**,**d**) and one is subtracted from the other one to form a spiral shaped blade, Fig. 3.1**e**. The blade is repeatedly attached on a disk and the extrude function completes the final structure.

Torque predictor The network for a torque predictor is illustrated in Fig. 3.2**a**. A CNN containing residual networks has been selected to build the torque predictor [232]. With deeper learning by adding layers, the residual networks provide enhanced performances, suppressing the degradation and vanishing gradients due to the skip connections. The residual CNN includes 13 Blocks (each consisting of one 2D convolutional layer, Batch normalization, and the Leaky ReLu activation function) and six skip connections completed with a flatten layer and two dense layers. It takes an input blade image (128 × 128), and provides an output torque value (1 × 1). The Adam optimizer [237] with the learning rate of $2.3\,10^{-4}$ and the mean squared error (MSE) loss function have been selected for the optimization [238, 239]. The optimization of the predictor algorithm was conducted until the torque predictor gave strong positive correlation (> 0.7) between real and predicted torque values from the validation dataset (Fig. 3.4**b** inset). The weight update of the torque predictor is halted after it reaches the required correlation value.

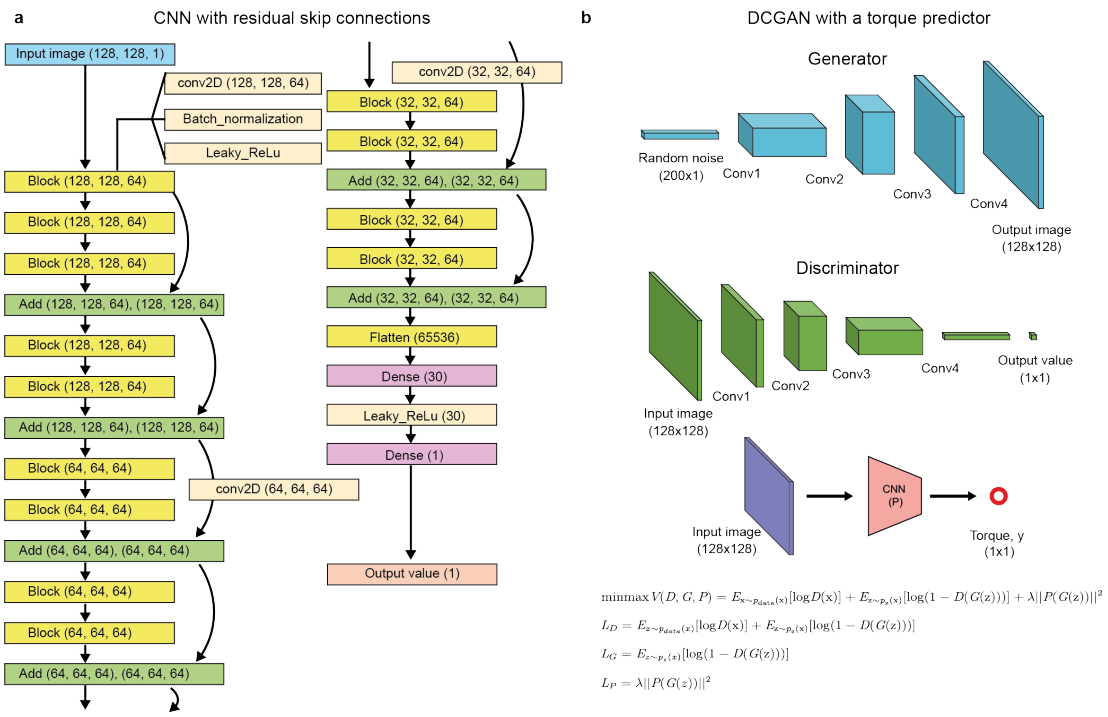

Figure 3.2: **Schematics of the machine learning algorithm. a**, Residual CNN optical torque predictor consisting of 15 bock layers and 6 skip connections. A block contains a convolutional layer, batch normalization, and leaky ReLu activation function. It receives an input image (128 × 128) and gives an output torque value (1 × 1). **b**, A DCGAN nanorotor structure generator is constituted by coupling a conventional DCGAN with the torque predictor in **a**. The torque predictor gives rise to an additional loss function, forward loss L_P.

Nanorotor generator The network for a nanorotor structure generator is illustrated in Fig. 3.2**b**.

DCGAN has been selected to design the nanorotor structure generator since it exhibits more stable and deeper training thanks to the convolutional layers compared to GAN [240]. The discriminator is composed of three convolutional layers with the kernel (5×5) and the strides (2×2 and 1×1), a flatten layer, and a dense layer. It receives an input image ($128 \times 128 \times 1$) and gives an output value (1×1). LeakyReLU was used as the activation function and the dropout rate is 0.3. The generator consists of one dense layer and three transposed convolutional layers with the kernel (5×5) and the strides (2×2); it receives an input noise (200×1), and generates an output image (128×128). The discriminator and generator loss functions are made of cross entropy. The optimizer for both is Adam with a learning rate of $1.0\,10^{-4}$. The nanorotor generator is constructed by combining the conventional DCGAN and the torque predictor. Once the torque predictor is involved into DCGAN, it begins to influence the adversarial feedback loop as an additional loss function, $forw\_loss$, which gives low losses for high torques. The gradient of "Total loss", $coef\_g * gen\_loss + coef\_f * forw\_loss$, is used to optimize the weight update in the generator during the training, and is adversarial to that of $disc\_loss$. After training, nanomotor generator produces further enhanced optical torques (Fig. 3.5). The coefficient $coef\_f$ gradually increases to suppress the porous surface during the training (Fig. 3.3).

3.2.2 Results and discussion

To prepare a dataset for machine learning, 4'400 nanorotors made of 30 nm thick gold nanostructures were generated by a random function varying the angle, length, and width (Fig. 3.1) [241]. For each structure, the corresponding torque value was calculated with SIE to form input pairs consisting of an image and its torque. Fig. 3.4**a** (left) shows an example of randomly generated single blade structure as a 128×128 binary image. A complete nanorotor structure is built by repeatedly attaching six blades to a central disk with a uniform angular spacing, as shown in Fig. 3.4**a** (right). Note that the torque calculations are conducted on the complete nanorotor structure. The torque increases with the number of blades, while the spectral torque peak position remains. The number of blades is set to 6 because the nanofabrication becomes excessively difficult for more than 6 blades (Fig. 3.6). This dataset is divided into a training set with 3'520 structures and a validation set with 880 structures.

The goal of the machine learning is to produce nanorotor structures that exhibit stronger optical torques than the training set. To do so, a torque predictor is built from a CNN with skip connections [232] and is implemented in DCGAN to provide an additional objective loss: a forward loss. A CNN, which extracts features from an image in multiple hidden layers and

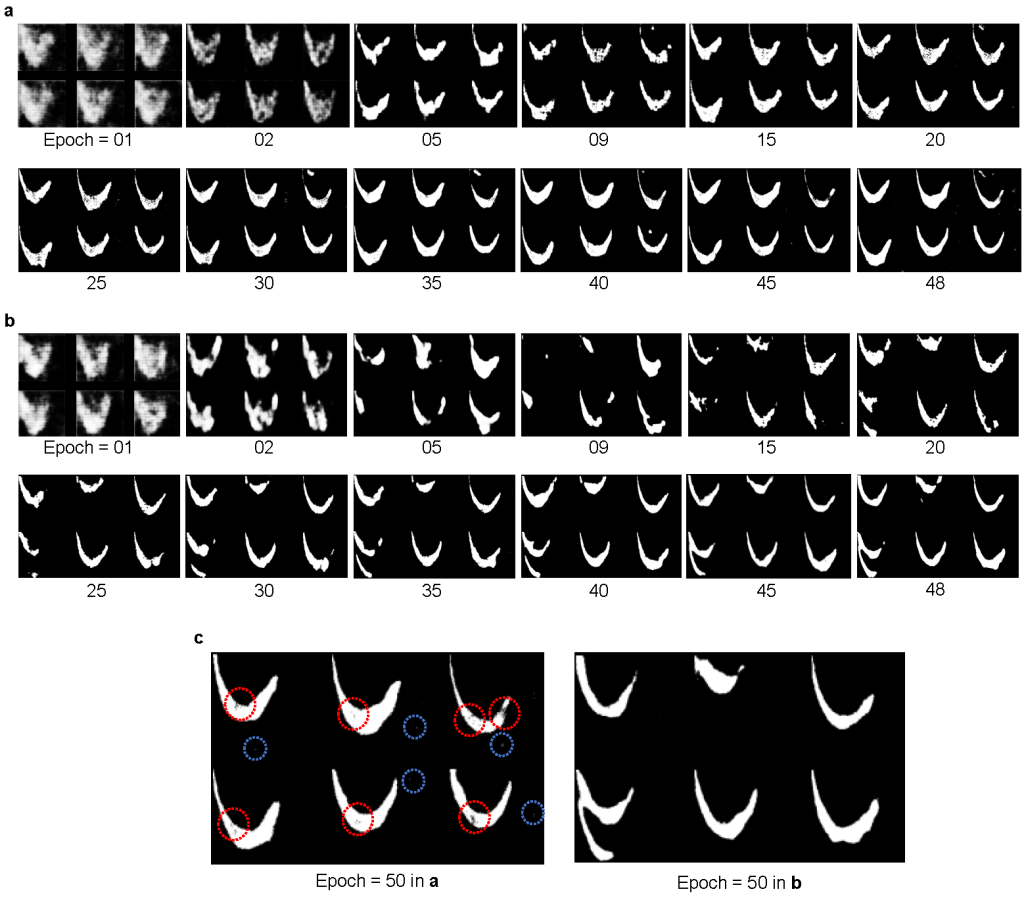

Figure 3.3: **Examples of 6 generated blades as a function of epoch. a**, $coef\_f$ is constant and fixed as 1.4 during the training. Generated images tend to have unfavorable porous surfaces and background noise during the training. **b**, With a gradual increase in $coef\_f$, porous surfaces and background noise are suppressed in the generated images. **c**, After the training, porous areas (red dashed circle) and background noise (blue dashed circle) are detected in **a** (left), whereas binary image quality is much improved in **b** (right).

tries to find a suitable weight matrix in fully connected layers [233], is trained with the training set. Once the training is done, the torque predictor receives a binary image (128 × 128 pixels) as input and provides a torque value (1 × 1) as output (Fig. 3.4**b** (top)). The validation set test indicates a strong correlation of 0.78 between the SIE calculated torques and the predicted torques, as shown in the inset of Fig. 3.4**b** (top right). The trained torque predictor is coupled to a DCGAN to form a nanorotor generator. The DCGAN generates new images which contain features from real images through the adversarial characteristics when the generator and discriminator loss functions are properly designed [187]. Implementing a torque predictor helps the machine acquire insights into the relationship between a geometry and its torque; it is essential to design a forward loss function which is directly affected by the torque values of

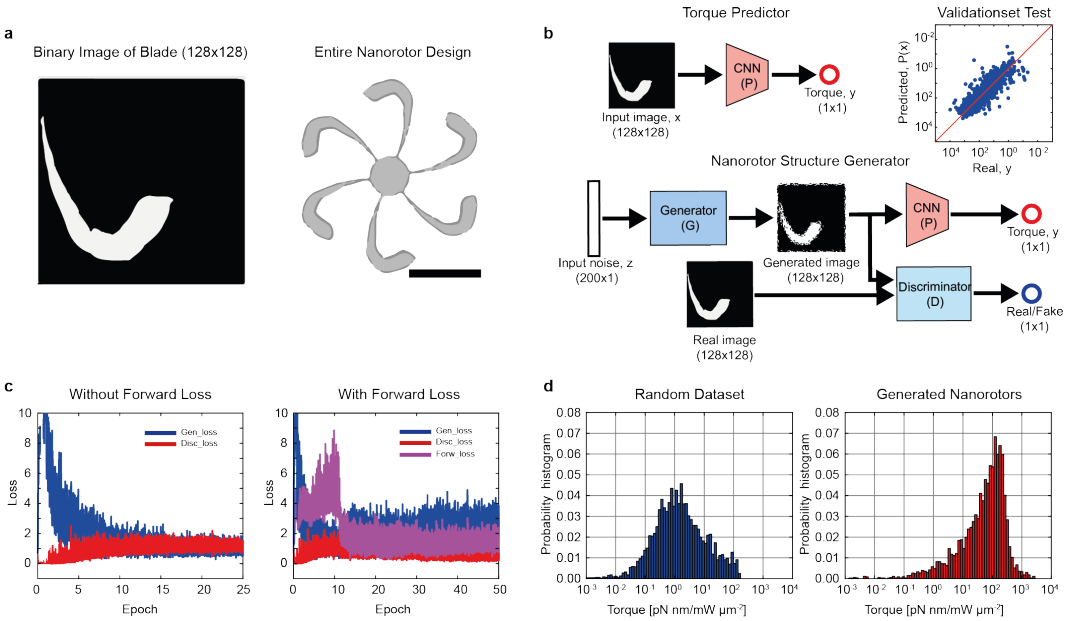

Figure 3.4: **Machine learning algorithm for nanorotors generation. a**, Example of a 128 × 128 binary blade image and a complete nanorotor structure consisting of 6 blades and a central disk (scalebar 100 nm). **b**, Schematics of torque predictor and nanorotor structure generator. The predictor is made of CNN and trained to predict a torque value (1 × 1) from an input image (128 × 128). The inset on the top right is the correlation between predicted and SIE calculated torques from a validation set excluded from the training set. A nanorotor generator is made of a DCGAN and a trained CNN. The algorithm tries to optimize not only the discriminator and generator losses but also the forward loss, which is inversely proportional to the predicted torques from the generated structures. **c**, Objective losses as a function of epoch. The generator and discriminator losses are reduced as a function of the epochs (left). A forward loss term is added and interacts with the conventional losses (right). **d**, Probability histograms of torques for the random dataset used for training (left) and for the generated nanorotors (right) (Fig. 3.5).

the newly generated nanorotors. The detailed training configuration can be found in Fig. 3.2. The generator in the networks receives a random noise input vector (200 × 1) and produces an image (128 × 128) according to its weight matrix.

Without the forward loss (Fig. 3.4**c** (left)), the DCGAN conventionally works such that generator and discriminator losses approach the asymptotic line at a so-called Nash equilibrium and produce nanorotor structures irrespective of torque values [240]. In this case, since it just reproduces the features of randomly generated nanorotor stuructures, the torques distribution resembles the random dataset (Fig. 3.5). To generate structures with improved torques, the forward loss is involved with the generator and discriminator losses, and influences the generator weight matrix training. Forward and generator loss functions are combined and

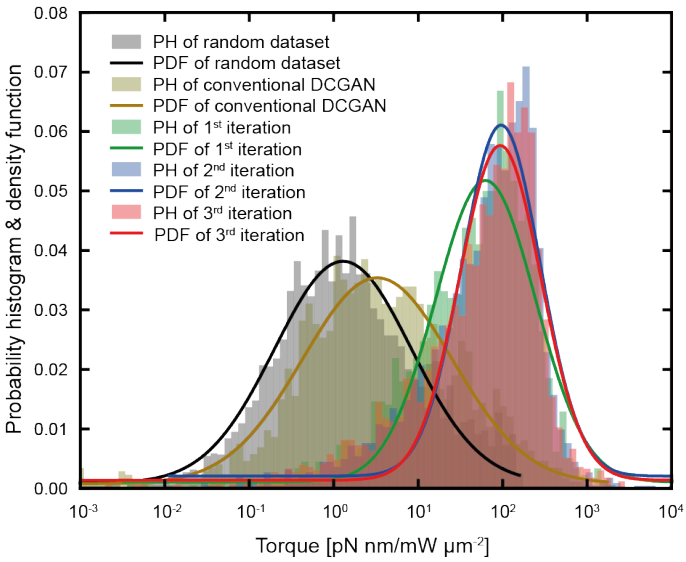

Figure 3.5: **Statistical analysis of output torque improvement.** Probability histogram (PH) and probability density function (PDF) of the random dataset (grey), the output of conventional DCGAN without forward loss (yellow), and the outputs of nanomotor generator with different iterations (green, blue, and red) are present. According to PDF of the random dataset, the random function in Fig. 3.1 produces nanorotors with torques around 1.0 pN nm most. The conventional DCGAN without forward loss produced slightly increased torques since it produces further randomized structures compared to the random function. When a forward loss term is added to the DCGAN, the output torques are improved, the PDF becomes right-shifted at the 1st iteration. The 2nd and the 3rd iteration show even better torques, peak positions at 100 pN nm, and narrower curves in PDF compared to that of random dataset. There is not much difference between these two iterations, which implies the end of learning.

adversarially operate against the discriminator loss function. The relative value weight of the forward loss compared to the generator loss changes by adjusting a forward loss coefficient during the training. At the beginning, the algorithm focuses on the generation of nanorotor-like shapes; then, as the coefficient of the forward loss gradually grows, it gradually increases the torque associated with the generated nanorotors. The forward loss coefficient is zero for epochs 0-10, 0.8 for epochs 11-20, 1.2 for epochs 21-30 epoch, and 1.4 for epochs 31-50 (Fig. 3.4**c** (right)). Consequently, the forward loss decreases as the epochs go by, and the generator and discriminator losses move away from the previous asymptotic line since the nanostructures with improved torques have different geometric features compared to the random training set. After the training, the nanorotor generator provides rotor-like structures with higher torques.

Figure 3.4**d** (left) shows probability histograms of torques for the random training dataset. For those random geometries, the maximum torque is 232 pN nm/mW μm^{-2}, and most of them –

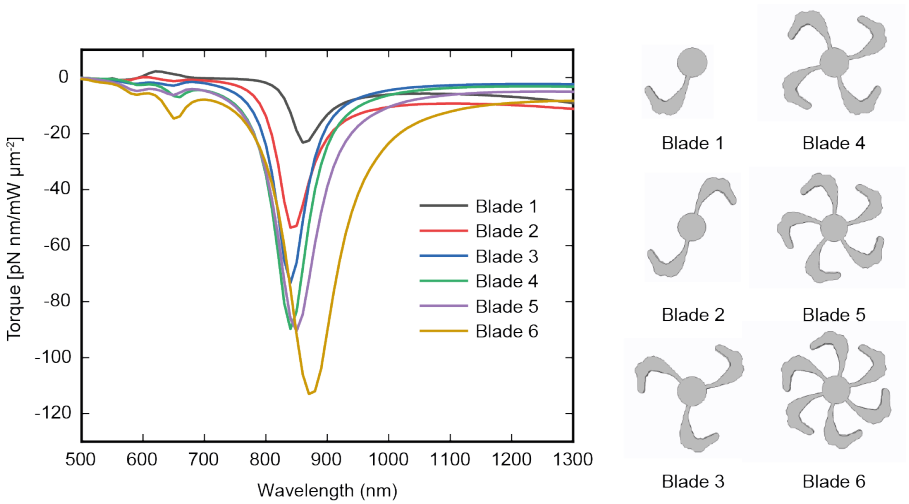

Figure 3.6: **Blade number dependency of the optical torque.** A blade generated by the random ellipse functions is combined with a disk. The optical torque increases with the number of blades while the rotor keeps the same distance between blades. Note that the torque spectra remain almost the same with the number of blades.

corresponding to the broad peak in the left panel of Fig. 3.4**d** – are around 1 pN nm/mW µm^{-2}. On the other hand, the nanorotors created by the trained generator network reach a torque of 2'799.3 pN nm/mW µm^{-2} (right panel). Furthermore, on average, the machine-designed nanorotors exhibit a torque two orders of magnitude larger than the random dataset. Based on the nanofabrication constrains, four rotors were selected for the experiments (Fig. 3.7).

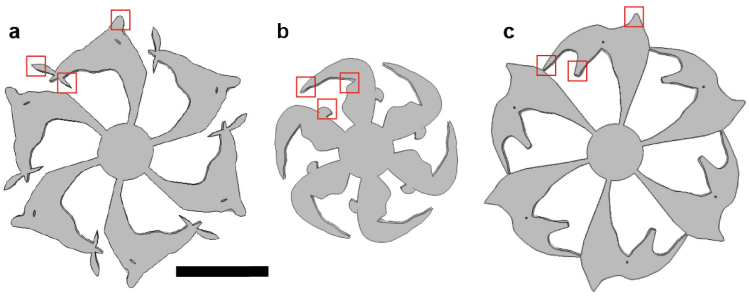

Figure 3.7: **Nanorotors with sub 10 nm features. a**, The nanorotor attains an extremely high theoretical torque 2′799.3 pN nm under a given illumination, 1.0mW/µm^2 (scalebar 100 nm). Unfortunately, this geometry requires sub 10 nm features (red boxes) that are beyond the feasible nanofabrication resolution. Other examples of nanorotors with small features and high torques: **b**, 1′987.7 pN nm and **c**, 1′786.0 pN nm, respectively.

3.3 Numerical analysis of generated structures

3.3.1 Methods

The electromagnetic response of a system is described by Maxwell's equations. In this work, the SIE method, which efficiently solves Maxwell's equations in their surface integral form [234], is used to study various optical properties such as SCS, multipoles moments, polarization states, electric field intensity distribution, Poynting vector flux, optical forces, and torques.

Surface current calculations on an object. The SIE solution provides electric and magnetic surface currents on each part of the triangular mesh that discretizes the surface of the scattering object (the plasmonic nanorotor in this case) [242]. With the surface currents, the parallel components of the fields can be directly obtained by the cross product of the currents and the outward vectors, and the perpendicular component of the fields can also be derived from Maxwell's equations [235]. Adding the two components for each field, the electric and magnetic fields on the surface can be expressed in terms of the surface currents. Using Rao-Wilton-Glisson (RWG) basis functions [243], SIE can expand the surface currents over triangular discretized meshes with the vertices of the triangle and the coefficients related to each vertex.

SCS calculation and multipole decomposition. At specific frequencies, the optical light-matter interaction can be especially strong, corresponding to the excitation of electromagnetic resonances in the system. These resonances are especially strong in plasmonic systems like the nanorotors studied here [244]. They appear as peaks in the SCS and are related to the material properties and the geometry of an object. With the SIE, the surface fields can be directly calculated by the surface currents. And, the scattering and extinction cross-sections are given by integrating the Poynting vectors of the incident and surface fields [245]. The multipole moments of the scattered field can be analysed by using vector spherical harmonic (VSH) basis functions [83]. A sum of VSHs represents the complex electromagnetic far-field, and integrating the complex scattered field on a large sphere (whose radious is 10 µm) allows us to find the decomposed multipole moments [246].

Optical force and torque calculations on a scatterer. Optical forces for arbitrary shapes under illumination have been numerically computed with Maxwell's stress tensor and the outward normal vector to the closed surface. The time-averaged optical force can be calculated by the time-averaged Maxwell stress tensor. From the SIE solutions, the Maxwell stress tensor can be directly expressed in terms of the surface currents [247]. Once the local optical forces acting

on each triangle of the mesh are computed, the optical torques at the center of mass can be calculated by the cross product of the position vector from the center to the centroid of the mesh triangle and the force vector [235].

Electric and magnetic field calculation near a scatterer. The surface currents obtained from the SIE method can also be used to calculate the near-fields surrounding a scatterer [248]. Vectorial solutions of the scattered electric and magnetic fields are obtained directly from the SIE solutions using Green functions. The distribution of the electric field intensity may then be computed by calculating the fields at local points (in this case the resolution is 2 nm). Time-averaged Poynting vectors, which represents the power flow and may also be related to the momentum flow, at each point are calculated by the cross product of electric and magnetic fields. Such flow are useful to understand how a nanorotor scatters light. Moreover, we can associate the collective contributions of each Poynting arrow to the rotary motions of the nanorotor.

Polarization state of the radiation. The polarization of the light scattered by the nanorotor was investigated to understand the origin of the optical torque. The polarization states are calculated using the Stokes parameters as a function of wavelength and then represented on a Poincaré sphere [249]. Since most of the scattered light is linearly polarized from 600 nm to 1700 nm, we conclude that there is no SAM, which indicates that OAM accounts for the angular momentum of light observed in the vicinity of the nanorotor.

3.3.2 Results and discussion

The selected Au nanorotor geometries are presented in Fig. 3.8**a**. The blue, red, green, and purple color frames on the generated images identify the individual rotors throughout. The SIE numerical technique was used to compute the SCS, multipolar decomposition, near-field distribution, time-averaged Poynting vector, optical force and torque for each geometry (see the "Numerical analysis with SIE" section in the Methods) [248, 235]. The nanorotor surface was discretized using a triangular mesh with a typical side length of 4 nm, which provides accurate numerical results for an operating wavelength around $\lambda = 980$ nm [242]; the experimental data from Johnson and Christy were used for the dielectric function of Au [250].

Figure 3.8**b** shows that the generated nanorotors exhibit a plasmon resonance around $\lambda =$ 980 nm, as desired. The SCS multipoles decomposition shows that the electric dipole is dominant, while the magenetic dipole or higher-order multipoles are negligible in the studied wavelength range. It is remarkable to note that all the designed structures are resonant at

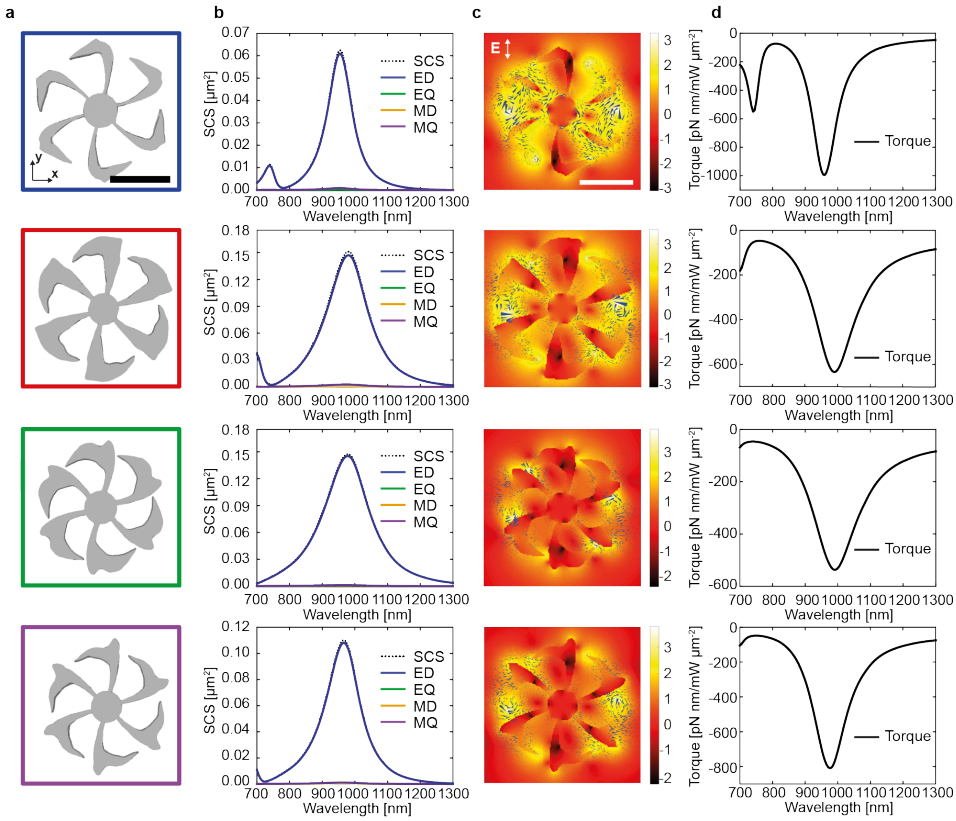

Figure 3.8: **Numerical analysis of the four chosen nanorotors. a**, The selected nanorotor geometries generated by the trained nanorotor generator. The blue, red, green, and purple colors identify the chosen geometries and will be used throughout (scalebar 100 nm). **b**, SCSs and multipoles expansions calculated with the SIE method for vertically polarized illumination at normal incidence; the electric dipole is the dominant multipoles and the rotors exhibit a plasmon resonance around $\lambda = 980\,\text{nm}$. **c**, Electric field intensity distribution (colormap) and time-averaged Poynting vectors (blue arrows) for the nanorotors at $\lambda = 980\,\text{nm}$ for vertically polarized incident light. **d**, optical torques calculated with the SIE method.

$\lambda = 980\,\text{nm}$, although this constrain was not included in the machine learning algorithms.

To gain insights into the mechanisms that lead to an optical torque in those nanostructures, we show in Fig. 3.8**c** the electric field intensity and time-averaged Poynting vector distributions in the x–y plane at the center of the structures. The Poynting vectors are generated by electric and magnetic fields exerted by the multipolar responses under the illumination of light [251]. Hotspots at the edges of each blade are observed at the resonant wavelength [252]. The Poynting vectors – representing a flow of photons with their momentum – point in opposite directions on each side of the structure, thus indicating the origin of the optical torque. Note that the centrifugal and centripetal components of the Poynting vectors do not produce any optical torque whereas the remaining components do contribute since the scattered photons

carry momentum. The nanorotor rotates to satisfy Newton's third law; hence, the rotation originates from the scattering optical torque, not from the absorption optical torque. The latter is a well-known principle, where the rotation direction follows the handedness of the incident circularly polarized light. However, it cannot explain the optical torque generated in the nanorotors considered here because these structures do not exhibit circular birefringent properties.

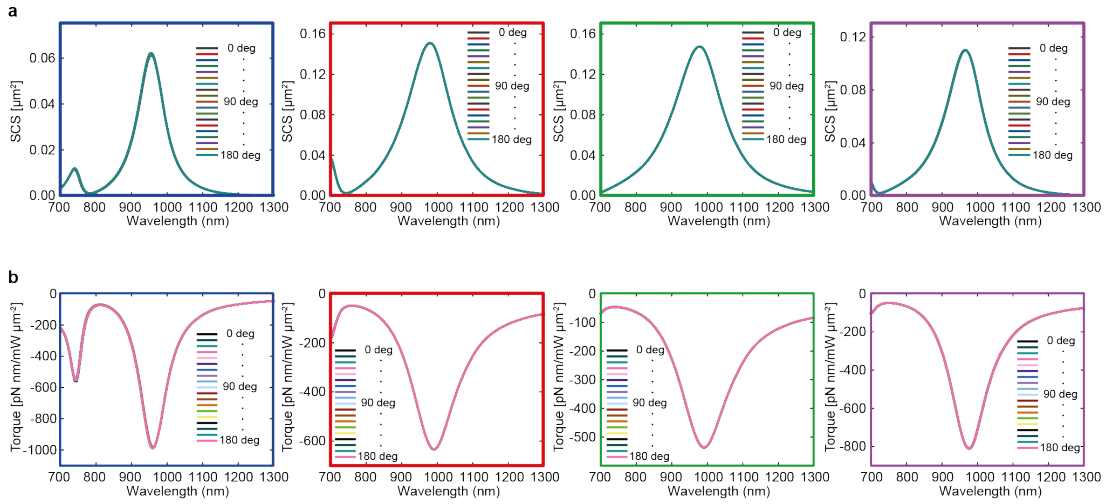

Figure 3.9: **Polarization independency of the selected motors. a,** SCS calculations demonstrate that the response is independent of the illumination polarization. The colors identify the chosen structures. **b**, Optical torques also do not depend on the polarization.

The time-averaged optical force on matter can be calculated by the surface integral of the time-averaged Maxwell stress tensor [247]. (Fig. 3.8**d**). The SCS properties, scattered light Poynting vectors, and the optical torques infer that the resonant optical scattering with plasmonic enhancement in the planar Au nanorotor induce angular momentum in the scattered light which did not exist in the incident light, and the reaction on the nanorotor results in the scattering optical torque.

Note that for incidence normal to the nanorotor plane, the generated torque and SCS resonance are independent of the incident linear polarization orientation. The optical torque peak position and amplitude remains unchanged for different orientations of the incident light polarization, which indicates that the rotor would continuously rotate under the constant application of a linearly polarized incident wave (Fig. 3.9).

The scattered light polarization state represented on the Poincaré sphere over the visible and infrared ranges shows nearly linear polarization (Fig. 3.10), implying that it possesses almost zero SAM. On the other hand, one may understand the existence of optical torques by

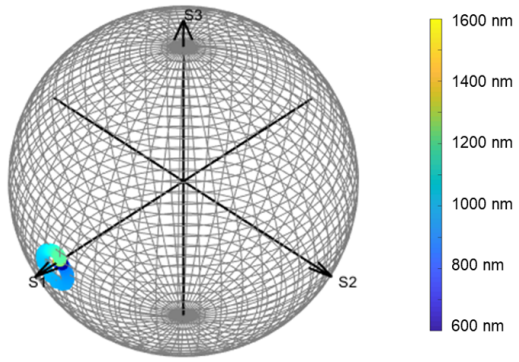

Figure 3.10: **Poincare sphere over the visible and infrared ranges.** The scattered light computed for one nanorotor remains linear polarized over visible and infrared ranges. This indicates that the angular momentum of light has no SAM but OAM.

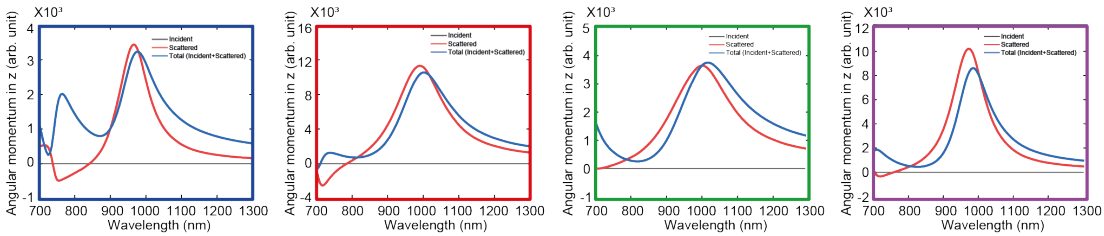

Figure 3.11: **Angular momenta of fields near nanorotors.** The cross products of location vectors from the center of nanorotors to points around the nanorotors and its Poynting vectors are calculated for incident, scattered, and total fields. The Scattered and total fields involve the angular momenta associated with optical torques while the incident fields has no angular momentum.

considering that the cross product of the location vector from the center of the rotor $\mathbf{r}$ and the time-averaged linear momentum density $\langle \mathbf{p} \rangle = \frac{\epsilon_0}{2} \mathrm{Re}[\mathbf{E} \times \mathbf{B}^*]$ produces the time-averaged OAM density $\langle \mathbf{j} \rangle = \mathbf{r} \times \langle \mathbf{p} \rangle$. It follows that the total angular momentum generated near the nanostructure can be calculated by volume-integral of the time-averaged angular momentum density of the total fields. Since the linear momentum density is linearly proportional to the Poynting vector $\langle \mathbf{S} \rangle$, the total angular momentum is thus given by $\int_V \langle \mathbf{j} \rangle \, dV = \frac{1}{c^2} \int_V \mathbf{r} \times \langle \mathbf{S} \rangle \, dV$. The z-components of the angular momentum reveals the reversed responses to the optical torque, which implies that the OAM induced by the off-centered Poynting vectors in the vicinity of the nanostructures mainly contribute to the optical torque on matter (Fig. 3.11).

3.4 Nanofabrication

3.4.1 Process flow

The entire nanofabrication process for free-standing nanomotors was carried out in the class 100 clean room at the the Center of MicroNano Technology of EPFL (CMi). The fabrication details are as follows.

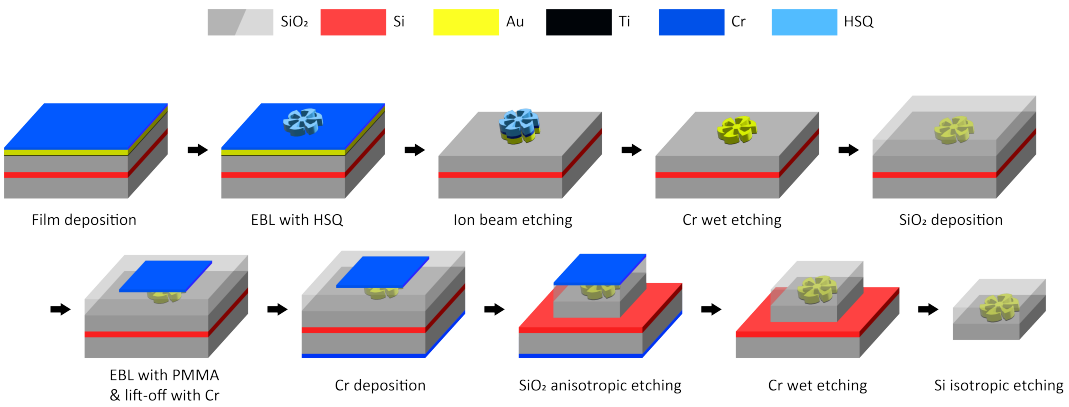

Figure 3.12: **Process flow for nanomotor fabrication.** Au nanorotors were fabricated using standard electron beam lithography (EBL). The HSQ masks protected the Au layer during IBE process. The plasmonic nanorotor was sandwiched between two 300 nm SiO_2 layers. Another EBL process, directional Cr deposition, and lift-off process were followed to form reactive ion etching (RIE) masks. After the lift-off process, RIE fabricated SiO_2 embodiments. Cr wet etching process removes the remaining Cr layers. The XeF_2 isotropic etching system etched the sacrifical Si layer, and detach the nanomotors at the last step from the fused silica substrate. More details are found in the "Nanofabrication process flow" section in the Methods

Substrate selection and cleaning. Fused silica wafers (Siegert Wafer GmbH) were chosen as the fabrication substrates. The diameter was 100 ± 0.5 mm and the thickness was 525 ± 50 µm. It consisted of amorphous SiO_2, 100 %. The root mean square value was 12 Å. There was no specific orientation. The degassing issue was not considered due to the high SiO_2 purity. The substrate wafer was cleaned with a sequential acetone-isopropanol and oxygen plasma (PVA Tepla Gigabatch; power: 200 W, O_2 flow: 200 sccm, pressure: 0.5 mbar, duration: 5 min).

Si and SiO_2 deposition. 200 nm of Si and 300 nm of SiO_2 layers were sequentially deposited on the substrate by sputtering in Pfeiffer Spider600. The deposition of the Si layer was conducted by a DC source (power: 1000 W, Ar: 15 sccm, deposition rate: 58 nm/mn). For SiO_2, reactive sputtering was executed with a RF source (power: 800 W, Ar: 29 sccm, deposition rate: 105 nm/mn). The temperature of the holder increased up to 350 °C during the sputtering process. At the initial stage, a target cleaning recipe with a dummy wafer was performed for

5 min for both targets. To compensate the time when the effective power reach the set point, 10 s were additionally added, assuming the deposition rate linearly increased with the power. Therefore, the deposition time was 2 min 4 s for Si and 5 min 20 s for SiO_2. The Si was used as a sacrificial layer to release the motors from the substrate at the end of the process flow. The SiO_2 layer was the bottom part of the SiO_2 embodiment for nanomotors.

Ti, Au, and Cr metal film deposition. The deposition of the 1 nm of Ti, 30 nm of Au, and 10 nm of Cr was sequentially carried out on the substrate by electron beam evaporation (Leybold Optics LAB 600H, electron gun: Ferrotec EV M8; 10 kW, room temperature, pressure: $1.5\,10^{-6}$ mbar). The Ti layer was used for a good adhesion between SiO_2 and Au films [253]. The thickness of Au layer corresponded to that of the nanorotor geometries for the optical torque calculations in Fig. 3.8. The Cr layer was added for two reasons: it provides significantly better adhesion of HSQ on gold, and as a sacrificial layer for the HSQ etch mask removal after the ion etch process.

EBL process with HSQ. The nanorotor geometries were written by EBL process (Raith EBPG5000, thermal field emission, 100 KeV). HSQ, a negative electron beam resist with low line edge roughness and sub-10 nm resolution, was chosen to form the etch mask for nanorotor structure. The substrate was baked at 180 °C for 5 min, followed by 1 min of cooling at room temperature. HSQ (XR1541 002, DuPont) was spin-coated at 4000 rpm to form a 50 nm film. After drying for 1 min in air and loading the substrate into the EBL chamber, it was exposed to define the nanorotor shapes. HSQ is sensitive to the electron beam doses; over- and under-exposures should be avoid to obtain a proper shape as designed. A dose test for nanorotors was performed between 3300 and 6300 mC/cm^2, with the proper dose depending on the chose geometry. After exposure, the wafer was developed with TMAH25 % (Tetramethylammoniumhydroxide, Honeywell), for 2 min in a protective hood. The sample was rinsed abundantly with deionized water to remove the developer for 10 min. Fig. 3.13 displays the HSQ nanostructures.

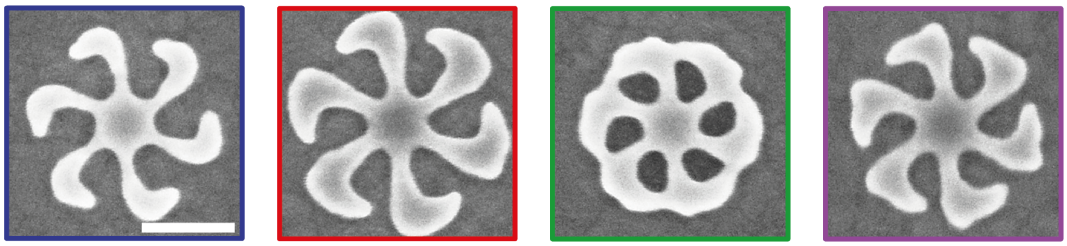

Figure 3.13: **HSQ masks after development.** The colors indentify the selected structures. HSQ masks for the nanorotors are presented. The optimized EBL dose enables feature smaller than 20 nm (scalebar 100 nm).

IBE process. Actual nanorotor structures were realized by Ar IBE (Veeco Nexus IBE350, ICP source with RF plasma: 1.8 MHz and 2 kW maximum, pressure: 10^{-4} mbar for operation and 10^{-7} mbar for base). The uniform and well-collimated ion beam led to directional etching. Cr, Au, and Ti were etched successively outside of the HSQ mask. The process was terminated when the 1 nm Ti starts being etched (Ti is immediately removed according to the etch rate). The stage was tilted at $-10°$ and rotated to minimize re-deposition on the sample sidewalls. Keeping local heating under control during the process was important maintain the etching quality. To this end, a low etch rate (etch rate: 15.4 nm/min for Cr, 30.5 nm/min for Au, and 10.2 nm/min for Ti) was selected to prevent the melting of the nanostructures. Heat dissipation was further promoted by performing 6 cycles of 10 s low etching followed by 1 min of cooling. The process was monitored by the secondary ion mass spectrometry system, which traces atomic masses of materials being etched in real time. Note that a low etch rate prevents the redeposition of material, which causes fences [254].

Cr wet etching. After the IBE, a Cr wet etching process removed the Cr together with the HSQ mask on top (Cr etchant, TechniEtch Cr01, $(NH_4)2Ce(NO_3)_6 + HClO_4$, etch rate: 65 nm/min). The etching time was 12 s for a Cr thickness of 10 nm. Then, the substrate was rinsed with deionized water 3 times. Au nanorotors were henceforth revealed on the substrate.

SiO_2 deposition.: A 300 nm of SiO_2 layer was deposited on the substrate to cover the Au nanorotors and form the upper part of the nanomotor SiO_2 embodiment (sputtering in Pfeiffer Spider600).

PMMA double layer spin-coating for EBL. The SiO_2 cubic embodiment was realized by PMMA double layer and EBL lift-off process. The substrate wafer was baked at 180 °C for 5 min to dehydrate the surface. After 1 min of cooling at room temperature, it was spin-coated with A4 495 kDa PMMA (Micro Resist Technology GmbH) at 6000 rpm and baked at 180 °C for 5 min. A2 950 kDa PMMA (Micro Resist Technology GmbH) was spin-coated at 2000 rpm on top to form a double layer structure and baked at 180 °C for 5 min. The heights of A4 495k PMMA and A2 950k PMMA were 120 nm and 90 nm, respectively. This double-layer resist facilitates the lift-off [255].

Cr conductive film deposition. EBL writing required a conductive substrate. However, the PMMA double layer was non-conductive. An additional Cr layer was deposited by sputtering on the substrate (Alliance-Concept DP 650, room temperature, pressure: $5.0\,10^{-3}$ mbar, Ar: 30 sccm, DC source, power: 200 W, deposition rate: 7.7 Å/s). The thickness of the conductive film was chosen as 10 nm to ensure conductivity and visibility for EBL alignment.

EBL process with alignment. The PMMA layers are positive resists for EBL. The electron beam dose was selected as 800 mC/cm^2 after a dose test. EBL enabled the alignment of the Au nanorotors and SiO_2 embodiments with an accuracy as good as sub 10 nm [256]. The alignment process consisted of 3 steps: overall alignment by the manual stage on the sample holder, automatic pre-alignment by global markers, and automatic local alignment by local markers. After the electron beam exposure, the Cr conductive layer was removed by wet etching. The exposed regions were developed by a developer (MiBK:IPA 1:3) for 1 min and rinsed with isopropanol for 1 min to remove some residual developer.

Cr metal film deposition and lift-off process. 50 nm of Cr, to be used as mask for the subsequent etching step, was deposited on the substrate by electron beam evaporation. Instead of a sputtering, a directional deposition was required to achieve a good yield. Subsequently, lift-off process was conducted with acetone in a glass container overnight or sometimes for a few days.

SiO_2 anisotropic etching. To form the SiO_2 embodiments, the excess of dielectric material was etched away using a SPTS Advanced Plasma System. This required a Cr conductive layer on the backside for electrostatic clamping. After loading the substrate and checking the leak-up-rate (less than 200 mtorr/min when the electrostatic clamping is sufficient), the directional plasma etching started with a C_4F_8/He gas. The etch rate was 440 nm/min. The end point detection system monitored the process in real time and indicated the time to stop etching (Fig. 3.14). After the anisotropic etching, the Cr layers were removed by Cr wet etching.

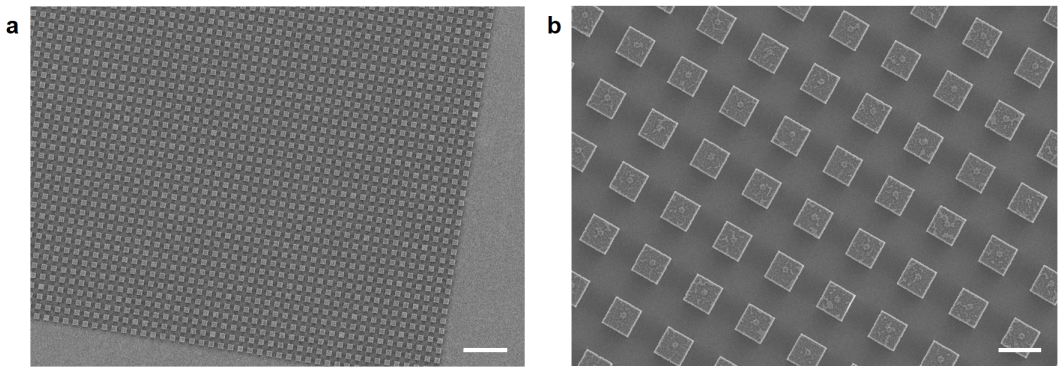

Figure 3.14: **SEM image of massive production of nanomotors. a**, Array of nanomotors (Scalebar 10 µm). As explained in Fig. 3.12, the SiO_2 array is formed by RIE directional etching with Cr masks, showing a nearly perfect yield. **b**, Magnified image, the protrusions on each SiO_2 cube indicate the embedded nanorotors (scalebar 1.5 µm).

Si isotropic dry etching. A XeF_2 etch system, which isotropically etches Si with a XeF_2 gas in pulsed mode, was used to remove the Si sacrifical layer to free the nanomotors from their

substrate. Once a sample was loaded, the chamber was evacuated and purged 30 times with N_2 gas for 5 s to dehydrate the substrate. The dry etching was conducted after these purges, under the following conditions: a duration of 30 s, a pressure of 2000 mTorr, and 20 cycles. After the etching, N_2 purges were used again to clean the chamber for safety. The XeF_2 etching process was optimized to avoid the motors detaching from the substrate.

Transfer from the fabrication substrate to a measurement cover glass. To facilitate the experimental measurement, nanomotors were moved from the fabrication substrate into a micro-chamber. First, a clean cover glass was prepared with a volume spacer (Sigma-Aldrich, GBL654002). A droplet of deionized water containing nanomotors was moved from the fabrication substrate to the clean cover glass with a micro-pipette. To increase the transfer yield, the volume of a droplet decreased down to one tenth of the entire volume of the micro-chamber, and the transfer procedure was repeated 10 times. Another cover glass covered the spacer and completed an isolated micro-chamber for the experimental measurement.

3.4.2 Results and discussion

The entire fabrication process and details are found in Fig. 3.12 and the Methods. Briefly, the four selected nanorotors were fabricated using EBL with the negative tone HSQ resist, which provides the very high resolution required to fabricate some of the very small nanorotors' features [257, 255]. Although the EBL raster size can be chosen as small as 1 nm, the smallest nanostructure feature size for the developed electron beam resist is in the order of 10 nm. After dose optimization, we were able to realize exquisite HSQ nanostructures that reproduced their design extremely closely, as shown in Fig. 3.13. This is of paramount importance for this work since we wish to let machine learning guide the experiments. The HSQ structure is then used as an etch mask for a 30 nm thick Au film. The actual nanorotors are then realized by Ar ion beam etching (IBE), followed by the removal of residual HSQ and Cr adhesion layer by wet etch, Fig. 3.15**a** indicates that these nanostructures match very well the designs obtained by machine learning shown in Fig. 3.8**a**. Some minute expansions are detected along the nanorotors' side walls; they occur due to the fencing effect of the IBE [254]. Even so, the fabricated nanostructures exhibit a minimum feature size of 17 nm, which is close to the best that can be achieved with nanofabrication technologies.

In addition to the Au rotor, a suitable nanomotor embodiment is required to prevent such a nanoscale motor to be subject to Brownian motion or to become unstably trapped in the optical beam due to its high aspect ratio (width / thickness $\simeq 8.0$). A SiO_2 cube satisfies these requirements and has been successfully used for other nanomotors in the literature [23, 115].

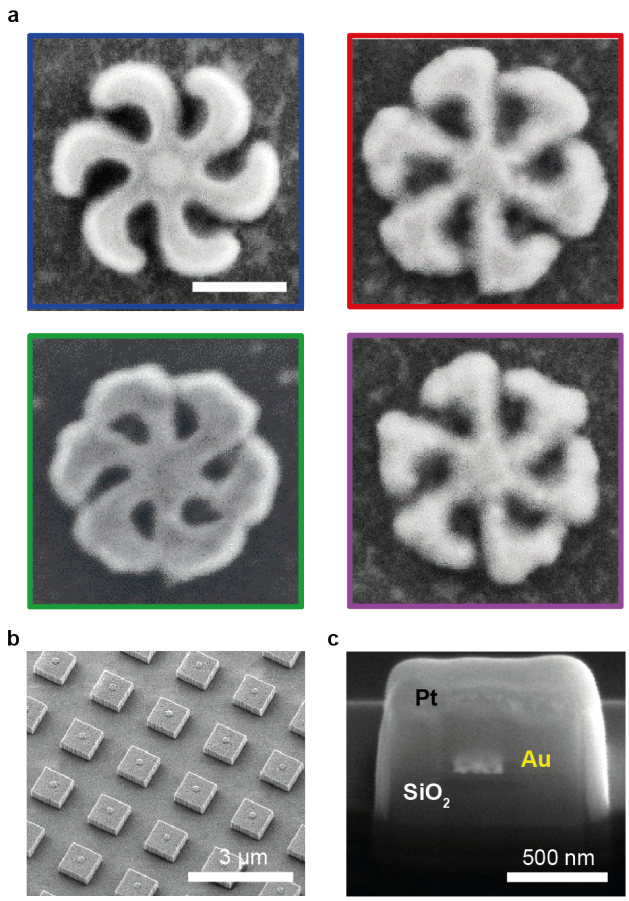

Figure 3.15: **Selected nanorotors and their embodiement in SiO_2 cubes. a**, SEM images of the fabricated nanorotors (scalebar 100 nm). **b**, 25° tilted-view of a nanomotor array, each SiO_2 cube contains an individual rotor (the round bumps indicate their locations). **c**, Cross-section of a nanorotor embedded in its SiO_2 cube, the Au nanorotor shape inside is recognizable (the cross-section was obtained by focused ion beam milling, requiring a 150 nm Pt protective layer deposited on the top to preserve the morphology).

Embedding a nanostructure in SiO_2 has the advantage of maintaining its details and hence its optical response. The SiO_2 cube that surrounds the nanorotor was patterned by EBL. Figure 3.15**b** shows an array of nanorotors embedded in SiO_2, the small protrusion in the middle of each structure is caused by the embedded Au rotor and demonstrates the excellent alignment of the SiO_2 cube with the Au rotor. The optimized fabrication process over large areas has an almost perfect yield and typically 90'000 nanomotors can be fabricated at once on the same substrate (Fig. 3.14). The cross-section of a motor is shown in Fig. 3.15**c** with a 52° tilt. The Au rotor structure can be recognized in the middle of the SiO_2 cube. Although part of the rotor was cut by focused ion beam milling for imaging purpose, the spiral shape of the remaining part is well recognized. This indicates that the nanorotors are not damaged and

maintain their shape during the nanofabrication process.

3.5 Experimental measurement

3.5.1 Setups

Two different measurement setups were utilized for the scattering intensity measurements and the rotation measurements. For the former purpose, back-scattered light was collected using a dark-field illumination mode [258]. The latter one included the laser illumination from top to avoid the disturbance of the gravity, and a bright-field mode to analyze the rotational motion.

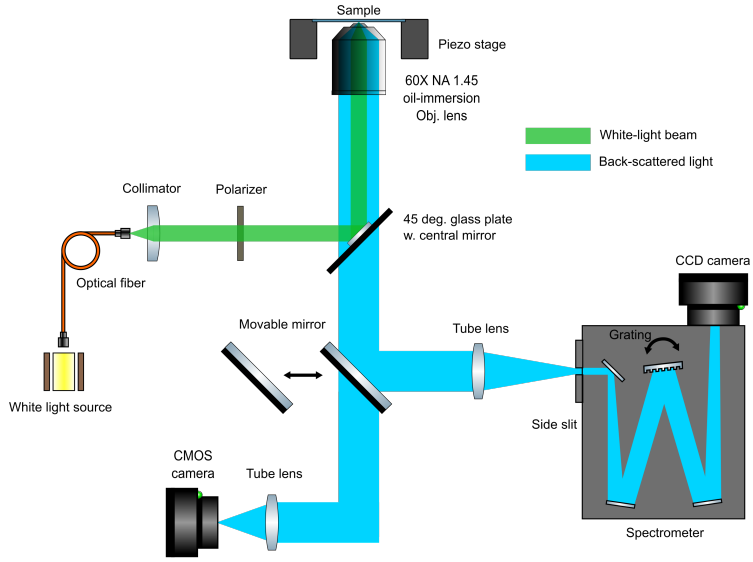

Figure 3.16: **Dark-field scattering intensity measurement setup.** White light is introduced from the bottom and focused by the objective lens. Reflected light from the specimen is directed by the mirror and guided toward a CMOS camera and a spectrometer.

Scattering intensity measurement setup. A reflection type dark-field optical microscope setup was used for the single nanorotor spectrum measurement (Fig. 3.16). The setup mainly consisted of the incident light source, 60X oil-immersion objective lens (NA 1.45), 3 mirrors, 2 tube lens, a CMOS camera, and a spectrometer. The incident light beam from a halogen lamp was transferred into the microscope via an optical fiber, collimated, and reflected by a central mirror whose diameter was smaller than the back pupil diameter of the objective. The focused incident beam was incident on the sample, and the back-scattered light was collected by the same objective. The scattered light from a nanorotor was transmitted to a CMOS camera or a spectrometer, depending on the position of the movable mirror.

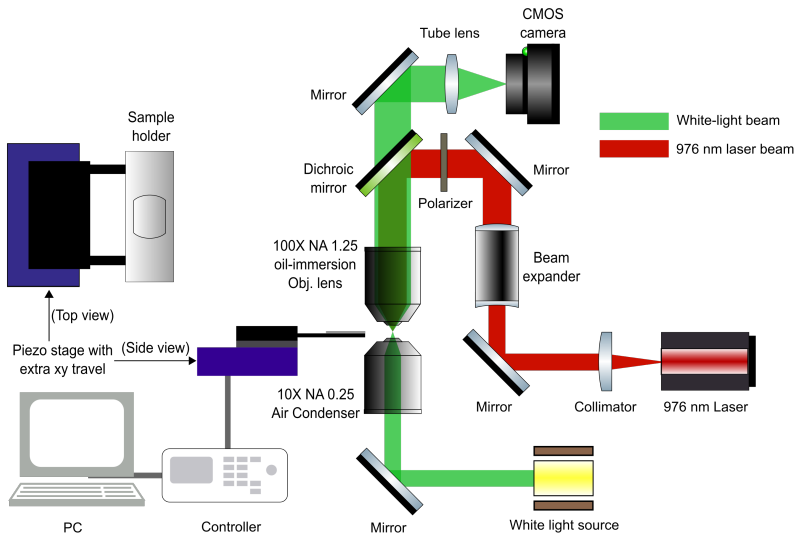

Figure 3.17: **Schematic of the rotation experiment setup.** A 976-nm laser is collimated and deflected by a pair of mirrors, which are focused on the specimen for the rotation measurements. The sample holder is mounted onto a 3D stage and imaged using a CMOS camera, with a LED providing the illumination.

Nanomotor rotation measurement setup. An optical experiment setup was built to perform the rotation measurement (Fig. 3.17). The requirements were a monochromatic laser illumination for the wavelength of 980 nm, a high NA objective lens to focus on the sample, precise sample stage control, and an imaging component. To fulfill these requirements, a modular optical tweezers system (OTKB, Thorlabs) was selected and used for the measurements. A 976-nm laser beam was transferred into the system through a single-mode optical fiber. Then, the beam was collimated, expanded, and illuminated from the top of a 100X oil-immersion objective (Nikon, NA 1.25, WD 0.23 mm). The focused beam passed through oil, cover glass, and deionized water in order to reach the specimen. The camera with a tube lens was positioned after the objective and a dichroic mirror. A white light beam for imaging was introduced from the bottom and focused by a 10X condenser (Nikon, NA 0.25, WD 7.0 mm). The cage system held the elements and provided the same optical axis for stable measurements. A 3-axis piezo stage with a kinesis controller was installed on the top of the 2-axis linear translation stage (13 mm travel), and precisely moved the sample holder.

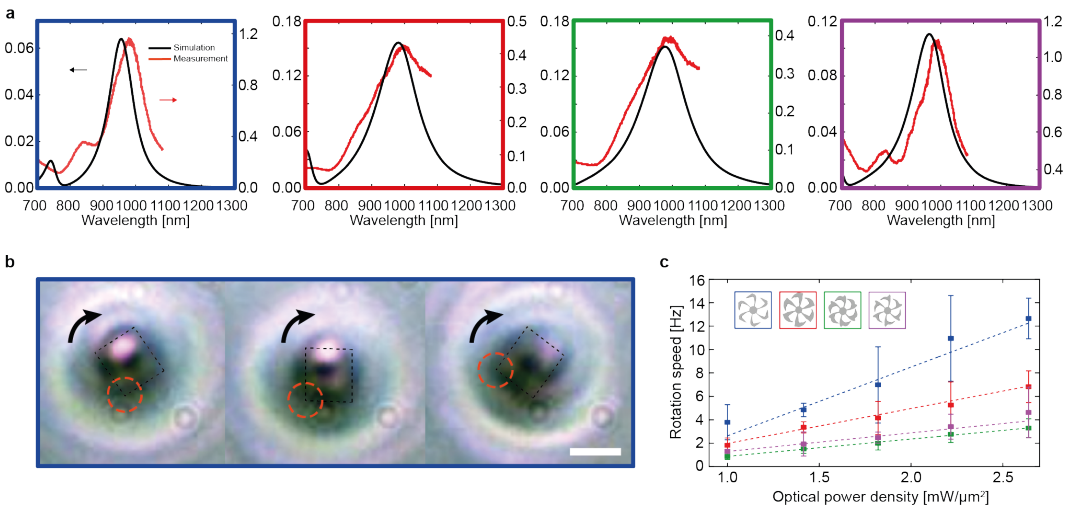

Figure 3.18: **SCS and rotation measurements. a**, SCS [μm^2] simulations (black lines) and experimental scattering intensity [a. u.] measurements (red lines). The color frame indicates the geometry, as in Fig. 3.15**a**. **b**, Example of capture rotation motion; the motor rotates clockwise (scalebar 1 μm). **c**, Rotation speed as a function of the laser power intensity, for the four selected geometries. The error bars correspond to the measurements of 5 different samples.

3.5.2 Results and discussion

To investigate their optical scattering properties, nanorotors simply fabricated on a SiO_2 substrate and covered with a SiO_2 layer (without cubic embodiment) were measured individually using a darkfield optical microscope setup (Fig. 3.18**a** and Fig. 3.16). The measured scattering intensities (red lines) agree very well with the SCS simulations (black lines) and exhibit a main peak around $\lambda = 980$ nm. The slight difference, in the order of 13–24 nm, between the measured resonance wavelength and the theoretical one can be explained by shrinkage or expansion of the effectively fabricate nanostructures (Fig. 3.19 and Fig. 3.20).

For the rotation measurements, the nanomotors were transferred into a micro-chamber containing deionized water. The measurement setup in Fig. 3.17 is described in detail in Methods. The chamber is illuminated from the top with a linearly polarized laser beam ($\lambda = 980$ nm through an 100× 1.25NA objective, Nikon). The optical power density at the sample location for the measurements ranges between 1.0 and 2.6 mW/μm^2. White light for imaging is also introduced from the bottom using a 10× condenser and the rotation measurements are performed in bright field mode on the top of the bottom cover slip. The SiO_2 platform is advantageous for the rotation measurements, as it suppresses Brownian motion, stabilizes the nanomotor for normal incidence, produces gravitational pull, and provides a symmetric environment for the nanorotor. The rotary motions are recorded and

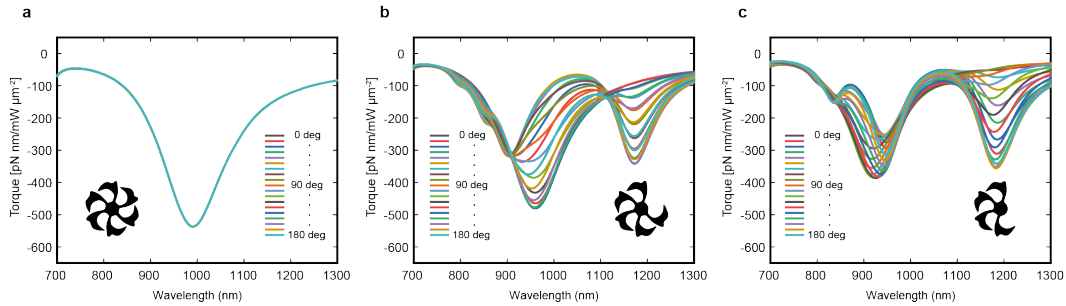

Figure 3.19: **Torque calculations on missfabricated structures. a,** The torque for an ideal structure does not have dependency to the polarization of incident light. **b**, This is not the case for a miss-fabricated structure missing one blade, which also exhibits and additional mode around 1200 nm, implying that destroyed structures have different spectral responses. **c**, When two blades are lost from the ideal structure, the torque values decrease and show additional resonances.

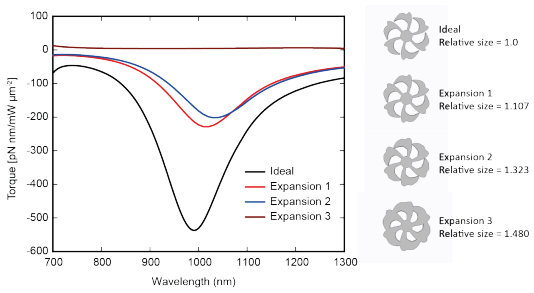

Figure 3.20: **Torque calculations on expanded structures.** To study the influence of nanofabrication accuracy, one of the selected motors is presented with relative size factors (Ideal = 1.0, Expansion 1 = 1.107, Expansion 2 = 1.323, and Expansion3 = 1.480). The larger the expanstion, the lower the generated torque. A red-shift in the torque spectrum is also observed.

analyzed, as shown in Fig. 3.18**b**. The rotation direction is clockwise, which is consistent with the negative torque retrieved from the numerical analysis. We observed the continuous rotation as well as the rotation speed increase with the optical power and the distance between the focal spot and the motor. When a focused laser beam is focused and introduced in the vicinity of a nanomotor, it is optically trapped around the focal center (Representative videos [241]), and starts continuously rotating under illumination. Figure 3.18**c** shows the rotation speeds measured for the selected rotors as a function of the illumination power [241]. Among the four different rotor geometries investigated, the blue motor exhibits the fastest speed for a given optical power density. There could be mainly two reasons for that. One is that it shows the highest torque according to the SIE calculations in Fig. 3.8. Another is the difficulty in achieving completely the identical structure as the design. Compared to other motor shapes, the red one retains the geometrical features in terms of the fact that each blade keeps the distance to one another despite the expansion. (Fig. 3.15 and Fig. 3.20). Further

advances in nanofabrication that allow feature sizes less than 10 nm would be required to verify this issue.

3.6 Summary

We have used machine learning to design optically-driven nanomotors and shown that machine learning as a global solution is beneficial for generating nanorotor structures with extremely high torques. The nanorotor generator, which combines DCGAN and a torque predictor, has suggested geometries that exceed the conventional intuitive structures and exhibit much higher optical torques compared to planar nanomotors reported so far in the literature. The experimental realization of some of these nanomotors has demonstrated that complex designs could be translated from the virtual computational world into effective nanoscale devices.

Careful process optimization has enabled the remarkable control of geometrical features down to 17 nm. However, the machine learning algorithm has also suggested nanorotor geometries with even higher torques that would require smaller feature sizes (Fig. 3.7). We can therefore anticipate that in the future, as nanotechnologies develop further, they will enable additional degrees of freedom to unleash the full potential of machine-driven designs.

Dark-field measurements have confirmed that the nanorotors exhibit resonances near the wavelength of 980 nm at which the machine learning algorithm aimed, indicating that the nanorotors scatter most strongly at the wavelength. In rotation experiments, each motor has performed rotational motion under linear polarization and presented a linear increase in rotation speed with laser power density, indicating that the rotary motion can be steered by the light intensity.

Plasmonic nanomotors can play an important function as transducers between optical and mechanical energies. The improved nanomotors presented here perform this function in an especially efficient way and can be used for optical manipulations in biology, energy harvesting, and advanced micro-fluidics. In addition, the suggested designing protocol consisting of CNN and DCGAN paves the way for the utilization of artificial intelligence to design nano-optical devices that overperform intuitive structures such as disks, triangles, rods, and other elementary shapes.

3.7 Future work

3.7.1 Pump in microfluidics

As an application of nanomotors, the generation of rotary motion has promising potential in microfluidics and lap-on-a-chip (Fig. 3.21). In order to fabricate a suitable microfluidic channel, there are several choices such as polydimethylsiloxane (PDMS) channel, 3D printing with two-photon polymerization, and the anisotropic etching process. PDMS is a polymer commonly used for the fabrication of microfluidic chips. The fabrication of the PDMS channel is a series of mold fabrication, PDMS pouring, baking for curing, demolding and surface activation for bonding which becomes further complicated as the required size decreases down to the sub 5 um scale. For channels with a few micrometers, filling the channel with water can be done by capillary forces. However, PDMS is a hydrophobic material and only one facet is a hydrophilic glass when the PDMS channel is attached to the cover glass. Also, for optical measurement, the oil immersion objective is optimized for the thin cover glass whose refractive index is 1.51 different from that of PMDS (1.43). 3D printing materials have the same issues as PDMS had above. To overcome the issues aforementioned, anisotropic etching technology can be selected for microchannel fabrication. It readily enables sophisticated adjustment in channel cross-section. For example, the width of a channel depends on laser writing patterns or masks while the depth is controlled by the etching time. Once we obtain microchannel patterns on a bottom glass, it can be combined with a flat top glass thanks to molding at a $520 - 10^{\circ}$ in oven. Consequently, a glass microchannel where the surfaces are hydrophilic is completed. The fabrication process flow of microchannels is illustrated in Fig. 3.22.

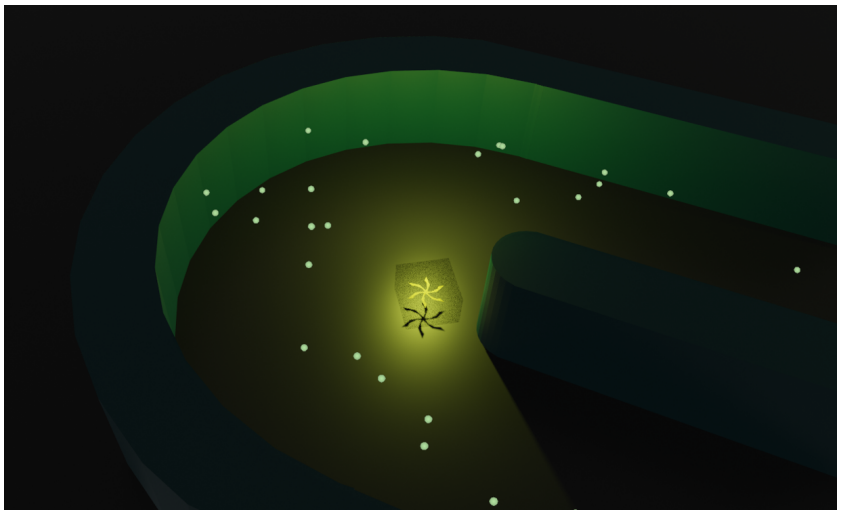

Figure 3.21: **Flow control of a nanomotor in a microchannel for pumping.** A microchannel whose width and height are comparable to a nanomotor can be built using an etching process. The capillary force fills the microchannel with nanoparticles suspended in water.

Step	Process description	Cross-section after process
01	**Substrate cleaning** 4 inch float glass wafer (D263 150 um thick) Acetone Piranha solution DI water Machine: UFT Piranha	SiO_2
02	**Cr deposition on the back** Machine: DP650 Recipe: rtf_Cr Thickness: 50 nm	SiO_2 / Cr
03	**Negative photoresist coating** Machine: ACS200 Resist: AZ nLOF 2020 Thickness: 1.4 um	PR / SiO_2 / Cr
04	**i-line laser writing** Machine: MLA150 Laser: 375 nm Dose: 190 mJ/cm² 1st Mask: CD = 5 µm Inluding markers	PR / SiO_2 / Cr
05	**Development** Machine: ACS200 Developer: AZ 726 MIF (with PEB)	PR / SiO_2 / Cr
06	**Al film deposition** Machine: EVA760 Recipe: Al Thickness: 50 or 100 nm	Al / Al PR Al / SiO_2 / Cr
07	**Lift-off process** PR remover: Acetone	Al Al / SiO_2 / Cr
08	**SiO_2 dry etching** Machine: SPTS Gas: C4F8/He Depth: 3.0 – 5.0 µm	Al Al / SiO_2 / Cr
09	**Cr wet etch** Machine: Arias acid bench Recipe: TechniEtch Cr01	Al Al / SiO_2
10	**Al wet etch** Machine: Arias acid bench Recipe: TechniEtch Al80	SiO_2
11	**Dicing with protection PR** Machine: DAD321 PR: AZ 1512 HS	PR / SiO_2
12	**PR removal and O_2 plasma treatment** Machine: Rem1165 and Tepla GiGAbatch Recipe: Surface activation	SiO_2
13	**Preheating** Machine: Neytech Qex Furnace Temps: 400 °C Time : 8 h	SiO_2
14	**Fusion bonding** Machine: Neytech Qex Furnace Temps: 580 °C Time : 8 h	SiO_2 / SiO_2

Figure 3.22: **Etching process flow for microchannels.**

4 Ion beam etching (IBE) optimization for plasmonic nanostructures

Some of the results in this chapter are in preparation for publication.

4.1 Introduction

Electron beam lithography (EBL) combined with subsequent lift-off or ion beam etch (IBE) processes are, nowadays, well-established nanofabrication schemes [259]. Following the trend to smaller dimensions, small-scale effects such as surface diffusion but also redeposition become more and more dominant, which compromises the quality of the output [255]. Compared to IBE, lift-off approaches using positive tone resists such as PMMA provide bumpy topologies with fuzzy edges due to surface diffusion, especially for highly mobile materials like gold. For plasmonic structures comprising small features it has been confirmed that using IBE the resulting nanostructures are more uniform and show better agreement with their targeted shape.

In addition, further optimization on IBE has been conducted to suppress parasitic sidewall fences that occur during the etching process [260, 261, 262]. During that process, the predefined mask protects the materials underneath and, ideally, the final structures represent an accurate projection of the shape of the etch mask. However, species released by physical sputtering processes have, typically, energies in a range with high sticking probability [263]. Therefore, and due to the angular distribution of the sputtered material [264], the ejected material is partly redeposited on the sidewalls of the etch mask and etched structures. The angular distribution of the ejected species depends on the ion energy [265] and the type of the sputtered material [261]. Actually, taking advantage of redeposition, 3D nanostructures with high aspect ratios have been fabricated [266, 262]. In this context redeposition phenomena

are of notable interest since various materials such as Au, Cu, Ni Pt, Pd, Sn, and oxides have particularly sticking properties [262]. Undesired redeposition leading to unwanted structural variations can be minimised at the microscale by adjusting the incident angle and rotating the sample [267] while further sophisticated techniques are required at the nanoscale [254]. Redeposited species fence the lateral sidewalls and block and deviate the ions leading to extended dimensions at the bottom of the structures [268]. As in the microscale range fencing can be suppressed to a large extent by tilting and rotating the sample. However, for features in the ten's of nm range this tactic cannot completely solve redeposition issues. Particularly for plasmonic applications, enlargement due to fences might be a critical issue since plasmonic field enhancement, coupling, resonances and modes are very sensitive to the geometry of the structures [266, 255].

Material removal by ion bombardment occurs at ion energies above a few tens of eV [269]. An energy of a few hundreds of eV are applied using standard IBE processes [270], whereas FIB milling requires much higher energies, typically 30 keV, in order to obtain suitable beam diameters [271]. For FIB, similar to IBE, redeposition may represent a bothersome issue, which is quite well studied in the context of FIB milling [271, 272, 273, 274]. Montecarlo simulations revealed manly two redeposition mechanisms, namely direct redeposition and secondary scattering [275]. Redeposition at the bottom side, arising from secondary scattering, reduces drastically the effective etch rate [276]. Experiments milling Si with Ga^+ show that redeposited materials on the sidewalls, caused by direct redeposition, are of amorphous nature containing Ga^+ but also an amorphous layer without Ga^+ has been observed because the impinging ions induce a collision cascade that breaks the long-range order of the poly-crystalline film [273]. The energy of ions involved in IBE processes is too low for causing substantial ion implantation. In contrast, using FIB techniques generates significant Ga^+ implantation close to the surface of the substrate [277] which influences the electrical properties of the sample due to knock-on damage and spatial defects [272, 278]. Surface damages associated with FIB process lead to a distorted morphology, which cripples the fabrication of small nanofeatures, whereas IBE is suitable for downsizing structures [279]. The redeposition rate is strongly affected by the confinement, particularly by the aspect ratio of the structure, and the milling rate for both FIB and IBE [274]. Reactive ion milling using FIB and IBE processes provides a possible strategy to reduces considerably the redeposition of sputtered material [280, 281]. However, this strategy is efficient only if the reaction products are volatile and can, therefore, desorb into the gas phase. This does not happen for some inorganic compounds such as gold since their products may adsorb on the surface. A further strategy, recently proposed, to prevent the fencing issue, is addition of a supplementary layer to protect the region of interest [282, 283]. For IBE of Pt, it

has been shown that a fenceless Pt structure can be produced by careful adjustment of the thicknesses of the Pt and photoresist layers. In addition, mixing Ar with Cl_2 generates water soluble chlorine compounds which can be removed applying a subsequent rinse step [268].

In this work, an optimised Ar^+ IBE process is presented to fabricate gold nanostructures, having features down to 10 nm, starting from a gold film with a thickness of 30 nm. Fencing due to redeposition, as described above, is one of the major hindrance for successful fabrication of structures with features in the 10 nm range. In the configuration studied in this work a gold film as thin as 30 nm has been used and exposed Hydrogen Silsesquioxane (HSQ) served as a hard mask for the IBE. A sacrificial Cr layer, acting as adhesion layer and serving for subsequent HSQ stripping, has been added. The thicknesses of the HSQ and Cr has been thoroughly adjusted in the course of this work. Polymerised HSQ [284], upon e-beam irradiation, exhibits similar optical properties than SiO_2 [285, 286]. The refractive index of HSQ is 1.450 at $\lambda = 632.8$ nm. In this regard, the minimum thickness of Cr is considered for applications where the Au structure is completely embedded in a SiO_2 structure [255]. The fences on the sidewalls evolve from redeposition of sputtered material stemming from the vicinity of the HSQ mask. Therefore, the structures of interest can be screened through addition of surrounding HSQ structures. Such dummy structures lower redeposition going along with a reduction of undesired fences. Rotating and tilting the sample during the IBE process turns out to further reduce sidewall redeposition. Finally, once the structural configuration, with respect to redeposition, is optimised, the feasibility of applying an Au wet etch process to ultimately reduce the fencing effects is considered.

This optimisation process has been applied to patch-type antennas, flowers, T-shapes, spirals, gammadions, and arbitrary shape structures. Therefore, this study provides a general fabrication strategy to greatly improve quality, reproducibility and reliability of even more complex nanostructures with feature sizes on the order of 10 nm. In addition, it gives valuable insights into the mechanism by which the structure expands due to redeposition during IBE. This general approach can be applied to nanofabrication with other sticky materials.

4.2 Method

EBL and IBE methods are well described in the previous paper of our group [255]. Briefly, HSQ (FOX16, DuPont) negative tone resist is exposed to e-beam irradiation (EBPG5000, Raith) and subsequently developed. The remaining polymerised HSQ serves as a hard mask for the Ar^+ (IBE IBE350, Veeco Nexus, Inductively coupled plasma (ICP) source with RF plasma: 1.8 MHz

and 2 kW maximum) applied afterwards. IBE etching has been performed applying an ion energy of 150 eV per second (300 V and 500 mA) at a pressure of 10^{-3} mbar. Rotation speed and tilt angle have been 10 rpm and 5°, respectively. A 3 grid optics enables collimated uniform Ar^+ irradiation over the entire sample surface. In the following, if not stated otherwise, the thickness of the Au layer is fixed at 30 nm and a 1 nm thick Ti layer has been added. Fig. 4.1 displays the overall process flow.

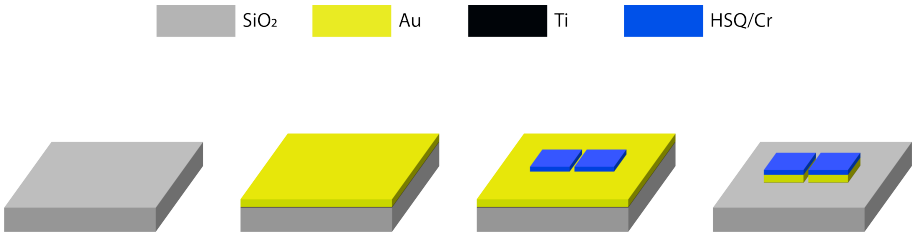

Figure 4.1: **Fabrication process flow for plasmonic nanostructures.** Au plasmonic nanostructures were patterned using standard EBL and IBE processes. The HSQ masks are formed by spin-coating and electron beam exposure. After development with TMAH 25 %, Ar ion beam etching removes the unprotected material. The remaining HSQ mask can be removed by Cr wet etching process if necessary.

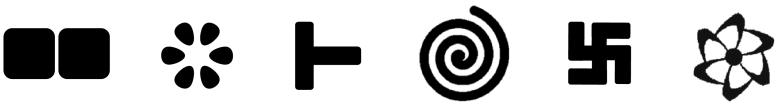

Figure 4.2: **Representative plasmonic nanostructures.** Six widely used plasmonic nanostructures such as nanoantenna, nanoflower, T-shape, spiral-shape, gammadion, and a more complex randomly generated, central symmetric wheel structure are selected. The nanoantenna and nanoflower structures are nanoparticle trapping sites when they generate hotspots in response to the incident light. They reduce the laser power density requirement density due to the plasmonic resonance properties. The T-shape structure is used for second harmonic generation. The spiral shape structure has optical responses sensitive to the handedness of the circularly polarized light. The gammadion shape shows chiral responses with non isotropic environment in the z-axis. A challenging structure whose minimum feature size is sub 10 nm is randomly generated in order to approach the limits of the current nanofabrication facilities. All the nanostructures are realized starting from a Au layer with subsequent EBL and IBE.

In this section, the variation of the degree of expansion with respect to the height of the HSQ and Cr layer is investigated. Furthermore, the impact of dummy structures, as described above, and Au wet etch post-processing is described.

During the etch process the HSQ mask is partially removed which reduces its influence in the

course of the etch process. At the end, the residual HSQ mask is removed by wet etching the Cr (TechniEtch ACI2, KI + I_2 based, MicroChemicals GmbH) adhesion layer between the Au and HSQ layers.

Six representative plasmonic structures have been selected: nanoantenna [3], nanoflower, T-shape [287], spiral [288, 289], gammadion [290], and more complex nanostructures (Fig. 4.2).

The entire fabrication process is carried out using facilities in a ISO 5 (class 100) cleanroom environment. Parameters such as type of resist, structure density and ratio exposed to non exposed area influence the most adequate electron dose to use. Therefore, dose tests have been performed to find the proper doses for each structure. It has been found that suitable doses which reproduce the original design in HSQ are 4500, 3900, 3600, 3600, 4750, and 4750 micro C/cm^2 in order from Fig. 4.2. Once the HSQ mask is correctly patterned, the conditions for IBE can be optimized. To suppress non-uniformity and reduce redeposition the sample holder has been rotated and tilted in the etching chamber, respectively. The tilting angle is 5° with respect to the vertical and the rotation speed has been 10 rpm. The etching process has been carried out at low power and sequenced into a repetitive cycle of 10 s of etching and 1 min of cooling. While repeating the cycle, the species of interest in the sputtered plume has been monitored using secondary ion mass spectroscopy (SIMS). The initial heights for HSQ and Cr have been 75 and 10 nm, respectively. The thickness of HSQ has been determined to be sufficient to withstand the etching process using the corresponding etch rates R_HSQ = 40 nm/min, R_Au = 72 nm/min and R_Cr = 30 nm/min. 10 nm of Cr guarantees good adhesion between Au and HSQ and proper removal of residual HSQ using Cr etchant (TechniEtch Cr01 (NH4)2Ce(NO3)6 + HClO4, Microchemicals GmbH).

4.3 Results and Discussion

Gammadion and wheel structures as shown in Fig. 4.2, have been selected for optimisation of HSQ and Cr heights since they contain sub 10 nm features and gaps fitting the addressed challenges. Fig. 4.3 shows the unprocessed HSQ masks and structures after the etch process in the left and right columns, respectively. The HSQ/Cr heights are 75/10 nm, 75/1 nm, 45/20 nm, 45/10 nm, 45/1 nm, and 25/1 nm starting from left to right in Fig. 4.3. Although, the top views of bare HSQ structures exhibit no significant variations for all thicknesses, the structures after the etch process differ considerably from the original design, depending on the heights of the HSQ and Cr layers. The comparison of Fig. 4.3**a** and **b** indicates that for a HSQ thickness of 75 nm, a reduction of Cr layer from 10 nm to 1 nm decreases fences and significantly improves the

contour of the inner and outer slopes. For HSQ thickness of 45 nm the etch process completely destroys the nanostructures when using a Cr layer of 20 nm as illustrated in Fig. 4.3**c**, whereas, with a Cr layer of 10 nm the structures have been withstood. This is because the HSQ thickness was not large enough for 20 nm Cr and 30 nm Au. As the Cr thickness decreases, the quality of the nanostructures improves, and the enlargement is further suppressed (Fig. 4.3**d** and **e**). When the HSQ thickness is further decreased to 25 nm while keeping the Cr layer at 1 nm, a shrinkage of the structures sets in since the HSQ thickness is not large enough to provide a reliable mask for the wheel structure with its features below 10 nm (Fig. 4.3**f**). However, for the gammadion structure with a width of 40 nm, the final shape approaches the HSQ mask very closely.

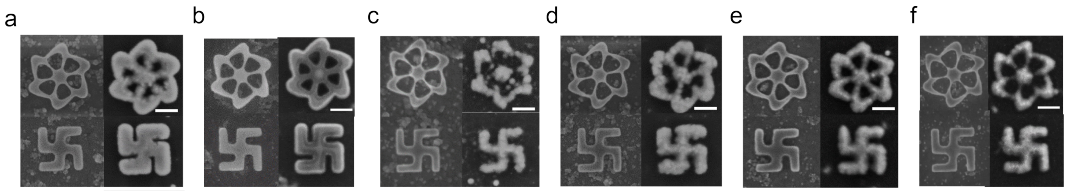

Figure 4.3: **Top view of nanostructures with different heights of HSQ and Cr.** The electron beam dose for HSQ exposure was 4750 mC/cm^2 for each case. The height conditions for HSQ/Cr are 75/10 nm (**a**), 75/1 nm (**b**), 45/20 nm (**c**), 45/10 nm (**d**), 45/1 nm (**e**), 25/1 nm (**f**).

To reduce the complexity of the problem of structural enlargement, a simpler structure, namely nanoantennas, has been investigated (Fig. 4.4). Two 300 × 300 nm^2 HSQ squares, separated by a 40 nm gap, have been written using EB. IBE has been carried out for two different HSQ/Cr configurations, namely 75/1 nm and 25/1 nm. The 75/1 nm, shown in Fig. 4.4**a** shows a much smaller gap due to redeposition effects. The cross-section reveals that the outer part has redeposited Au on the sidewall of HSQ (Fig. 4.4**b**). The zoomed-in view in Fig. 4.4**c** clearly shows that redeposition leads to an enlargement. In contrast, with a thinner HSQ layer, 25 nm, (Fig. 4.4**d**), the 40 nm gap remains. However, as indicated by the cross-section in Fig. 4.4**d**, the final structures end up in trapeziodal shapes. Due to higher etch rate at the corners with respect to planar surfaces with small ion incident angle, the shape of the mask changes in the course of the etch process. Consequently, when using thin masks the corners of the structures are laid bare, which causes truncation or faceting of the structures [291, 292].

A cross-section analysis of the wheel structure has been carried out for 3 different HSQ thicknesses with 1 nm of Cr: 75 nm, 45 nm, and 25 nm (Fig. 4.5). The cross-sections reveal, especially for a 75 nm mask, fencing effects are more pronounced at the outer than at the inner enclosed sidewalls. The volume to etch inside the inner boundaries is very small and therefore only little amounts of sputtered material can be potentially redeposited onto the

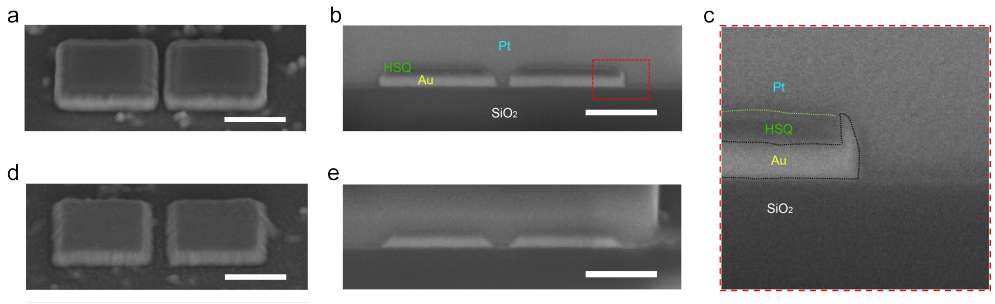

Figure 4.4: **54° Tilted view and cross-section of nanoantennas. a**, 75 nm HSQ/ 1 nm Cr masks are used for IBE. **b-c**, Cross-section of **a** shows that the outer sidewall of HSQ masks are covered by redeposited Au materials. **d**, 25 nm HSQ/ 1 nm Cr masks are used for IBE. **e**, The sidewall deposition is not observed due to the consumption of the HSQ mask during IBE. (Scalebar: 200 nm)

inner sidewalls. (Fig. 4.5**a**). In the 45/ 1 nm configuration fences are suppressed due to the lower thickness of HSQ (Fig. 4.5**b**). Using a thinner mask, the angle for the sputtered material to escape is increased and, therefore, less material can be redeposited onto the sidewalls. The thinnest HSQ layer is almost completely consumed before the IBE process is complete (Fig. 4.5**c**) and, consequently, faceting, as described above, becomes visible.

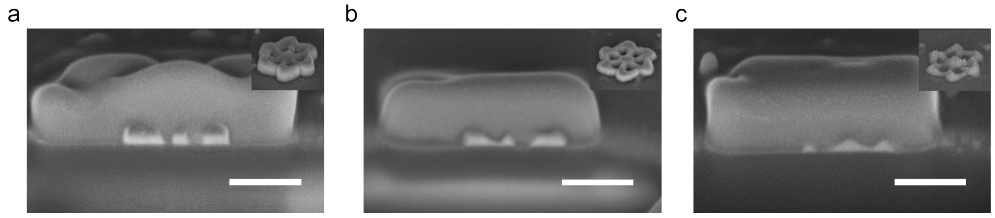

Figure 4.5: **Cross-section of arbitrary shape with/without fences. a**, 75 nm HSQ/ 1 nm Cr masks are used for IBE. The outer part of the HSQ masks are covered by redeposited Au. The inset is the nanostructure before the cross-section analysis. **b**, 45 nm HSQ/ 1 nm Cr masks are used for IBE. In the cross-section, the partially consumed HSQ structures are observed after IBE. The fences on the sidewall are supressed. **c**, 25 nm HSQ/ 1 nm Cr masks are used for IBE. In the cross-section, the HSQ structures are barely observed due to the consumption during IBE. The shape of Au represents an isosceles trapezoid.

The aforementioned results give valuable insights to optimise the IBE process. First, thinner mask and Cr layer lead to more accurate nanostructures. Second, small features require thicker masks. Third, thin masks induce faceting since the mask starts to be completely consumed at the edges. Ergo, optimisation of redeposition and faceting need diametrical requirements, low and high mask thickness to minimise fence and facet effects, respectively. The nanostructures introduced in Fig. 4.2 are realized using IBE under optimized conditions, namely, 45 nm of HSQ and 1 nm of Cr for the dimer and wheel structures and 25 nm of HSQ and 1 nm of Cr

for the nanoflower, T-shape, spiral and gammadion structures. The results are displayed in Fig. 4.6.

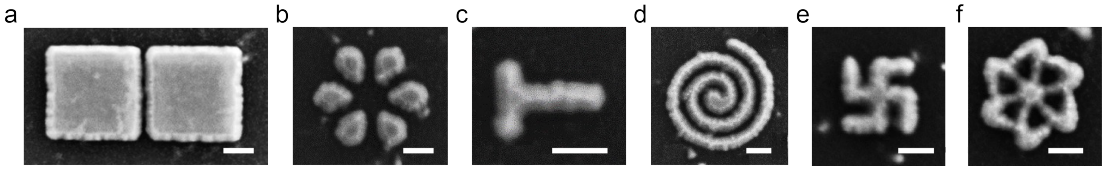

Figure 4.6: **Nanostructures with optimized HSQ and Cr heights.** Sub 10 nm gap nanoantenna (**a**), nanoflower (**b**), T-shape (**c**), spiral shape (**d**), gammadion (**e**), and arbitrary structures (**f**) are fabricated using EBL and IBE. The original design is represented in Fig. 4.2. 45 nm HSQ/1 nm Cr masks are used for **a and f**. 25 nm HSQ/1 nm Cr masks are used for **b, c, d, and e**.

The achieved sub 10 nm gaps of the dimer (Fig. 4.6**a**) and the wheel shape (Fig. 4.6**f**) appear well-defined using the 45 nm HSQ/1 nm Cr configuration. Using this configuration, fence and facet effects are substantially suppressed and very accurate structures, including the sub 10 nm features, emerge. In plasmonic systems such as nanoflowers (Fig. 4.6**b**), spirals (Fig. 4.6**d**) and Gammadion shapes (Fig. 4.6**e**), near-field coupling strongly depends on the distance between the individual structures. To achieve the required optical response, fencing effects should be minimised to a maximal extent. This has been accomplished using a 25 nm HSQ/1 nm Cr configuration. Using the same mask configuration the structural integrity of the T-shape (Fig. 4.6**c**) is attained, which plays an important role for its polarisation dependent response.

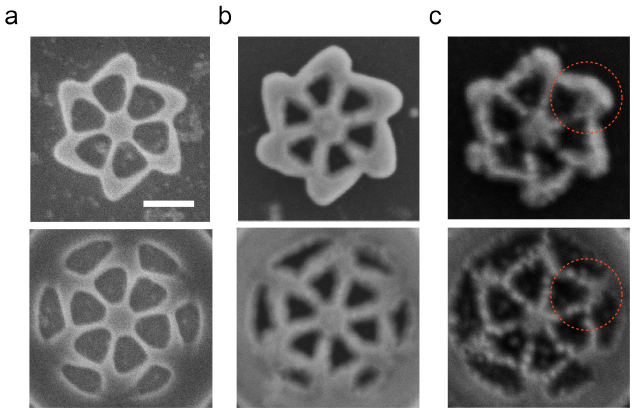

Figure 4.7: **Role of additional dummy structure in the vicinity. a**, HSQ structures of 45 nm HSQ/ 1 nm Cr masks are prepared for IBE without ring (top) and with a ring (bottom). **b**, Nanostructures of **a** are presented after IBE process. Although fencing is somewhat suppressed, it is not that obvious. **c**, IBE is further performed to figure out the effect of the dummy structure. The difference within red dashed rings on the top and bottom indicates that covering materials around the nanostructures prevents the materials nearby from being redeposited.

After the optimisation of thickness of the HSQ and Cr layers, redeposition stemming from the surrounding material is prevented by adding a circular dummy structure close to the structure of interest. A doughnut structure was additionally introduced around the wheel structure to test this hypothesis. For the resulting HSQ mask of the wheel structures, after e-beam exposure and development, the additional dummy structure does not reveal a significant impact. (Fig. 4.7**a**). However, after performing IBE, it can be observed that the original structure changes due to redeposition (Fig. 4.7**b**). This becomes more obvious after IBE has further been performed. It becomes evident, that the additional dummy structure adopt the role of a shielding obstacle (Fig. 4.7**c**).

Au films deposited by electron beam evaporation exhibits preferentially a poly-crystalline morphology. In contrast, redeposited Au due to Ar^+ bombardment during IBE is supposed to be amorphous and, therefore, exhibits a faster etch rate compared to the more stable poly-crystalline morphology when applying a wet etch process. To remove undesired redeposited material a subsequent wet etch step with a highly diluted (300:1) Au etchant has been applied for 5 s. Prior to the wet etch fences due to redeposition can clearly be observed Fig. 4.8**a, c**. After applying the Au wet etching process for 5 s, the redeposited Au on the outer part vanished (Fig. 4.7**b, d**).

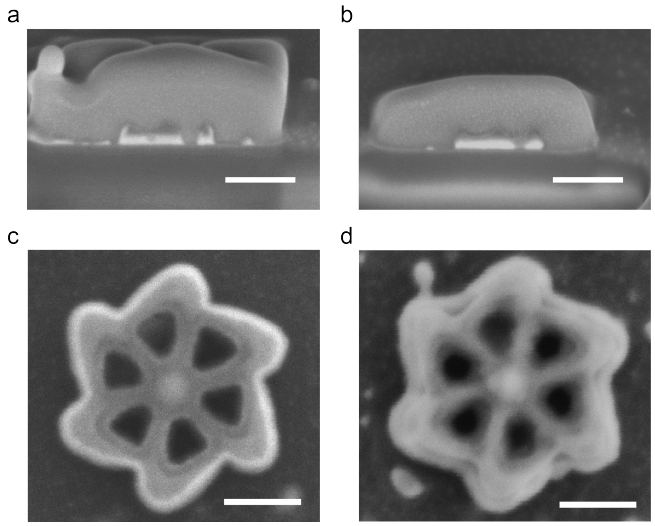

Figure 4.8: **Au wet etching to remove the sidewall fences. a**, IBE was conducted with HSQ structures of 75 nm HSQ/ 1 nm Cr. The outer fences due to redeposition are observed. **b**, After 10 s of Au wet etching process, the sidewall fences are removed. **c**, Top view of **a** shows the fences inner and outer parts. **d**, Top view of **b** reveals the original rim of the HSQ mask. However, a residue in the form of a melted shape is observed around the mask.

4.4 Summary

Following our previous paper which described a comparison of IBE and lift-off process for plasmonic nanostructures, this chapter elucidated even further subtle effects related to IBE for sophisticated nanostructures. To do so, we considered not only the common parameters such as ICP energy, electron beam doses, stage rotation speed, tilt angle, and cooling time but also the heights of HSQ/Cr masks, dummy structures, and Au wet etchant. We have detailed the origin of fences that appear during IBE and strategies to avoid them.

According to the results obtained, HSQ/Cr heights can be adjusted to suppress structural expansions during IBE. This provides us with a useful guideline when fabricating nanostructures. Since the sub 10 nm features require a sufficient thickness of HSQ, we have to choose whether to save the bulk part with a thin HSQ thickness or the sub 10 nm features with a slightly thicker HSQ, depending on the purpose desired. After the height optimization, Au wet etching and doughnut dummy rings have been considered. Both approaches provide further improvements.

This chapter has presented solutions to minimize expansion due to fences redeposited during IBE by capturing basic, but easy-to-miss, details when performing IBE. Therefore, it will be a very useful method for those who want to increase the degrees of freedom in the fabrication of nanoplasmonic structures or to implement challenging nanostructures.

5 Optical trapping with fluorescence resonance energy transfer (FRET)

5.1 Introduction

Since the introduction of optical trapping using a focused beam, discovered by Ashkin in 1986 at Bell laboratory, the so-called optical tweezer has become a significant technique in the fields of optics, chemistry, and biology [1]. The optical tweezers make use of the forces generated by an intensively focused light to trap and manipulate small objects such as nanoparticles, molecules, DNA, and biopolymers [293]. A small object scaling from tens of nanometers to few micrometers in the vicinity of the highly focused light is drawn by gradient forces. The gradient force is generated by the intensity gradient that is the origin of the trapping potential, while the direction of the gradient force is toward the center of the light focus. [2]. Plasmonic nanoantennas that give rise to a locally confined field enhancement can significantly improve trapping stiffness [3]. In addition to particle trapping, assemblies within a volume using optical tweezers have attracted researchers due to their promising applications [294]; for ecample, opto-thermoelectric manipulation demonstrates both trapping and assembling of particles [295, 296].

In the case of tightly trapped or assembled particles, the distance between the trap site and the particles can be sub 20 nm or even zero. The goal of the fluorescence resonance energy transfert (FRET) experiment was to measure the distance between a trapped particle and a surface, using the distance-dependence of the FRET efficiency [297, 298]. To achieve that goal, we have investigated various trapping platforms, such as plasmonic trapping using a nanohole array, a single nanoaperture, corrugated gratings, and the opto-thermophoretic trapping of two PS particles. To make a link between FRET and optical trapping, FRET pairs are selected and prepared with the surface functionalization technologies using the carbodiimide peptide

bond synthesis method. Valuable applications in tight optical trapping and assembling can be considered thanks to the ability to qualify the trapping and assembling performances via the FRET signal.

5.2 Theory

5.2.1 Optical trapping with plasmonic nanostructures

Subwavelength aperture

One of the plasmonic nanostructures is a small aperture in a thin metal film. When the diameter of this aperture has a subwavelength dimension, it can interact with an electromagnetic wave at a resonance determined by the geometry of the aperture and the optical properties of the incident electromagnetic wave. In 1944, Bethe theoretically studied the behavior of light as it passes through a single subwavelength aperture (Fig. 5.1), smaller than the wavelength of the light in a perfectly conducting thin metal film [299]. According to his description, the transmitted intensity dramatically decreases with the $4^{\mathbf{th}}$ power of the light wavelength, $(r/\lambda)^4$. In the case of a perfect metal, the transmission efficiency through the aperture in a metallic film is given by:

$$\eta = 64(kr)^4/27\pi^2, \tag{5.1}$$

where r is the hole radius and the wave vector of the incident light, k, is $2\pi/\lambda$. According to Beth's equation, it is clear that the transmission efficiency, η, can decrease significantly when the wavelength of light, λ, becomes much larger than the radius of the hole, r. In addition, the transmission efficiency can be further reduced when the thickness of the hole is considered. Beth's theory describes a dramatic reduction in transmission efficiency, η, in the cutoff wavelength condition, $\lambda > 4r$. If the wavelength λ, is smaller than r, the transmission efficiency, which represents the flux of photons per unit area, will converge to 1. The cutoff wavelength, which is used as a reference point for this reduction, is summarized by Cohn [300]. In other words, the transmission of light with a wavelength larger than the cutoff wavelength is supposed to be suppressed. For a circular hole of radius r, the cutoff wavelength is determined by the following expression, $\lambda_c = 3.4r$. It may increase in real structures because of the skin-depth, which represents the penetration of the light in the wall of the aperture [301].

Note that the transmission efficiency near the cutoff wavelength in Fig. 5.1 is greater than 1. There is a resonance phenomenon that leads to transmission efficiency enhancement at the resonant wavelength. The presence of localized surface plasmon (LSP) was also proved by

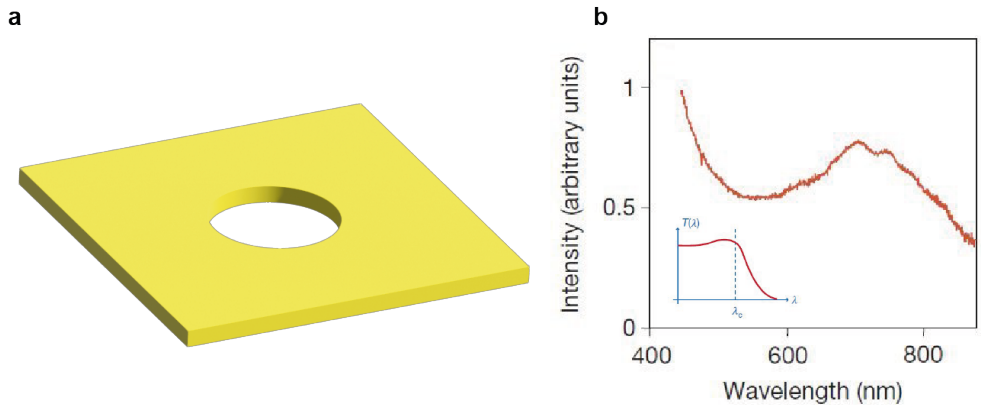

Figure 5.1: **Single nanoaperture and its transmission spectrum. a,**SEM image of a subwavelength aperture in a 200 nm thick Au film (scale bar: 150 nm). **b**, Transmission spectrum for an aperture with the cutoff wavelength. The inset shows a simulation result for the aperture.

theoretical studies[302, 303]. In experiments, we can also see a peak in Fig. 5.1 that doesn't exist in Beth's theory[304]. This resonant peak can be understood as the excitation of a LSP mode occurring in the edges of the hole. In the case of rectangular apertures, LSP modes are still present and depend on the polarization direction of light[305].

The transmission efficiency can be enhanced further by adding structures that can provide the enhancement [306]. When we have a periodic grating around a single aperture, the grating plays the role of coupling the incident light of a specific wavelength into the surface plasmon polaritons (SPPs). As a result, transmission efficiency through the aperture is enhanced and a characteristic spectrum appears. The propagating wavelength at the resonance is determined by the periodicity of the corrugation, which provides the required momentum to allow for SPPs along a surface in the dispersion relation plot. In addition, if the corrugation pattern is also on the other side of the metal film, a transmitted light with much less divergence and enhanced intensity than a single aperture can be produced. This is because the light transmitted from the aperture is coupled to the periodic structure of the output side and scatters the surface wave modes into a light propagating in free space. This causes interference with the light passing through the aperture, resulting in a better defined beam.

Periodic array of apertures

When it comes to a periodic array of apertures (Fig. 5.3), the ability to easily tune and enhance the transmission spectra by adjusting its periodicity allows us to have many applications [307]. One simple example is a color filter that can select the transmitted color by adjusting the

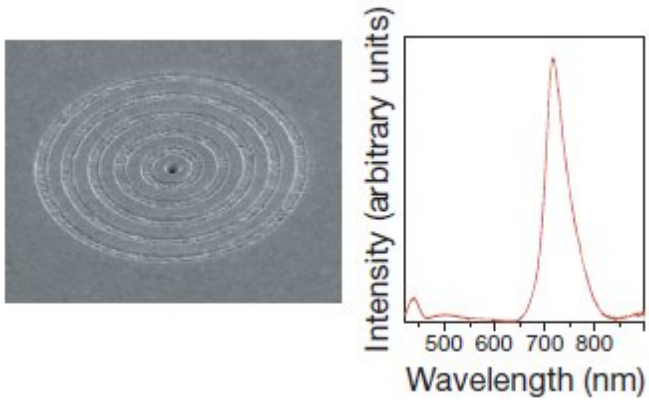

Figure 5.2: **Nanoaperture with periodic corrugations.** A single apertures surrounded by periodic corrugations (left). Transmission spectrum of a single hole surrounded by periodic corrugations (right, hole diameter 300 nm, period 650 nm) [306].

period of the geometry [308]. This color selection is enabled by the periodicity of the array providing the momentum required for the coupling process where the incident light couples to SPPs. In other words, if the periodicity changes, the momentum provided by the periodicity of the array is modified, and the required incident wavelength to generate the SPPs changes accordingly.

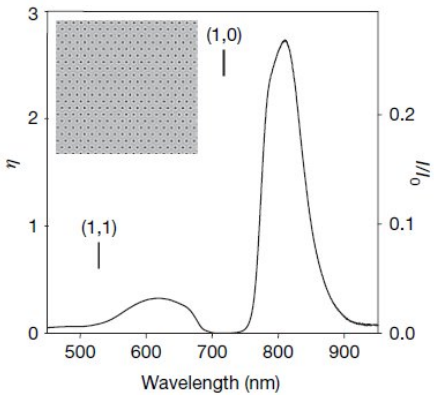

Figure 5.3: **Transmission spectrum of an array of apertures.** The triangular aperture array was fabricated on a 225 nm thick Au film (aperture diameter 170 nm, period 520 nm). The collimated white light was used as a light source. The inset shows the SEM image of the actual array [309].

In 1998, A study on this surprising light behavior has been demonstrated and named as an extraordinary optical transmission (EOT). For a two-dimensional periodic array, the coupling of each nanoaperture with the incident light gives rise to a much stronger transmitted light intensity than expected[310]. The EOT comes from the interaction between constructive interferences and surface plasmons. In EOT, the transmitted spectrum has several modes,

which are associated with the surface plasmon modes and depend on the periodicity of the array. The peak positions of the EOT due to periodicity in the transmission spectrum can be obtained by the following equations.

$$\vec{k}_{SPP} = \vec{k}_{in} + \vec{k}_R, \tag{5.2}$$

where $\vec{k}_{SPP}$ is the wave vectors of the SPP and $\vec{k}_{in}$ is the x-component (parallel to the surface) of the incident light wave vector. The wave vector of the reciprocal lattice, $\vec{k}_R$, is given by:

$$\vec{k}_R = n\vec{b}_i + m\vec{b}_j \qquad (i, j = 0, 1, 2, \cdots), \tag{5.3}$$

where $n\vec{b}_1$ and $m\vec{b}_2$ are the primitive vectors for a square lattice with $|\vec{b}_1| = |\vec{b}_2| = 2\pi/a_0$. To make an approximation, a surface plasmon dispersion relation for a smooth film is applied, ignoring the fact that the apertures on the film may change the properties in the plasmon dispersion:

$$|\vec{k}_{SPP}| = \frac{\omega}{c}\sqrt{\frac{\epsilon_S \epsilon_M}{\epsilon_S + \epsilon_M}}, \tag{5.4}$$

Based on the above equations, (5.2) and (5.4), we can derive a formula for the predicted peak positions at normal incidence $\theta = 0$ [311].

$$\lambda_{max}(i, j) = \frac{a_0}{\sqrt{i^2 + j^2}}\sqrt{\frac{\epsilon_S \epsilon_M}{\epsilon_S + \epsilon_M}}, \tag{5.5}$$

where a_0 is the periodicity of the square aperture array; i and j represent integer mode indices, and ϵ_S and ϵ_M are the dielectric constants for the substrate and the metal, respectively. As we discussed before, in Eq. (5.5), the positions of the peaks can be designed and tuned for specific wavelengths [312, 309, 313]. Figure 5.3 shows the transmission of the periodic array of apertures in experiments, which exhibits the two modes $(1,0)$ and $(1,1)$. However, the peak positions predicted in Eq. (5.5) do not correspond to the actual positions. This is because the equation does not consider the scattering losses due to the presence of the nanoapertures and ignores the resonance shift due to the interference phenomenon [314].

To display the difference between the theory described above and the real experiments, the zero-order experimental transmission intensity distribution as a function of photon energy and $\vec{k}_x$ is presented with the predicted energy dispersion of surface plasmons (solid lines) and the locations of Wood's anomaly (dashed lines) in Fig. 5.4. The x-component of the incident wave vector along the plane of the sample, $\vec{k}_x$, varies with the incident angle, as described in Eq. (5.2). The maxima and minima in zero-order transmission spectra respectively represent

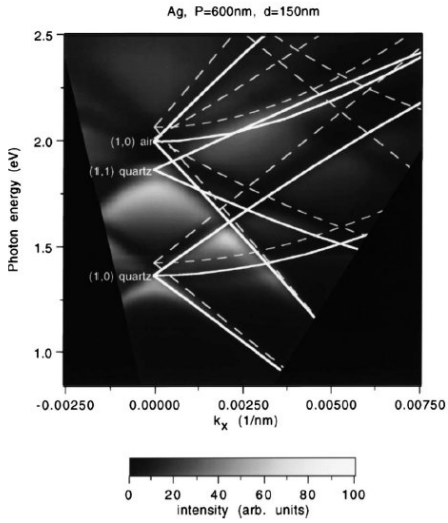

Figure 5.4: **Transmitted intensity with surface plasmons and Wood's anomaly.** The transmitted intensity is shown on a gray scale, the solid line is related to the excitation of a SPP on a flat surface, and the dashed lines are predicted by the Wood-rayleigh anomaly equation [311].

the surface plasmons and locations of Wood's anomaly, which corresponds to the predicted solid and dashed lines.

Plasmonic structures for optical trapping

To overcome the fundamental limitations of the conventional optical tweezers, plasmonic nanostructures can be utilized to increase the local optical intensity through the confinement of light [315, 316, 317], surpassing the diffraction limit. These characteristics lower the required optical power while maintaining accuracy in trapping nanoparticles. The conventional optical tweezers that are discussed in the previous chapters trap nanoparticles on a laser focal spot with a gradient force predominating over the scattering force. On the other hand, the gradient force and the trapping potential change with the $3^{\mathbf{rd}}$ power of the particle size, so high laser power is required to trap small particles stably. Plasmonic tweezers that lower the required high power to trap nanoparticles have been studied in various forms such as nanoholes [318], pairs of gold particles on glass substrates [319], and nanopillars protruding from a gold film [320].

Nanostructures with plasmonic resonances mentioned above are particularly useful for controlling light at the nanoscale. They can be engineered to be effectively coupled with the propagating light and to concentrate the light onto a highly localized optical field. This is usually called hot spots and is represented in Fig. 5.5**a** by two red dots at each end of the gold nanorod. While making the confinement effect and trapping potential deeper, plasmonic

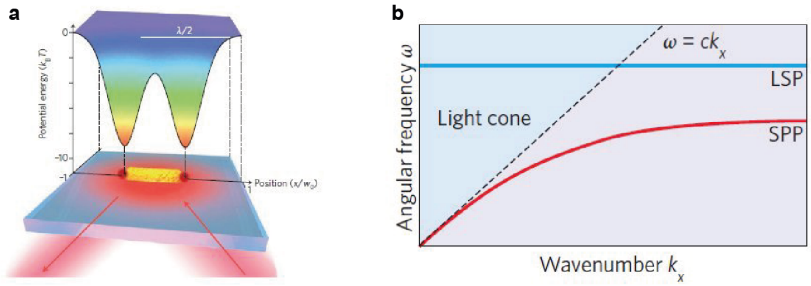

Figure 5.5: **Example of an plasmonic optical tweezer. a**, Schematic of optical potential emerging from the light illumination on a gold nanorode. The half-wavelength bar shows the approximate size scale [321]. **b**, Dispersion curves of LSP (blue line) and SPP (Red line).

structures give more opportunities for optical trapping at the nanoscale.

Two different surface plasmons, SPP and LSP, distinguished according to their generation mechanism and their propagation, are examined to see how each is coupled with incident light and generates an intense and confined surface wave. Both modes require a negative dielectric function that originates from the electron plasma in a metal. First, the LSPs require a subwavelength structure and exist in a limited frequency range, according to their finite dimensions as shown in Fig. 5.5**b**. The spectral position of their resonance is closely associated with structure dielectric function, size, and shape. LSPs can be directly coupled with the incident light, unlike SPP. When it comes to the SPPs, these propagating surface waves are supported by the free electrons in the metal surface and represent evanescent modes that exponentially decay when moving away from the surface. To generate SPPs, a special technique is required to overcome the momentum mismatch between free propagating planewaves and the SPPs, as illustrated in Fig. 5.5**b**. This is usually done by placing a glass prism with a higher refractive index on the metal surface and causing total internal reflection. An efficiently coupled SPP mode leads to intense and confined surface waves whose intensity close to the surface is much larger than that of the incident light.

Figure 5.6 shows a schematic for optical trapping of 100 nm PSs using a 310 nm subwavelength aperture. It achieved more than an order of magnitude reduction in intensity for optical trapping, compared to conventional optical tweezers. For the experiment, the Au film with the aperture was installed in a liquid chamber with 0.05 %w/v polystyrene spheres (PSs). The chamber was mounted upside down. A 1064 nm wavelength laser was used and focused on the aperture by a x40 microscope objective (0.65 NA). The beam spot size was 2 µm, and the optical power density was 1.0 mW/µm^2. The fact that the transmission resonance of the aperture is sensitive to the local refractive index can be used to track whether the particle is

trapped near the aperture. Once a PS is trapped, the transmitted intensity jumps up because PSs have higher refractive index than the surrounding medium.

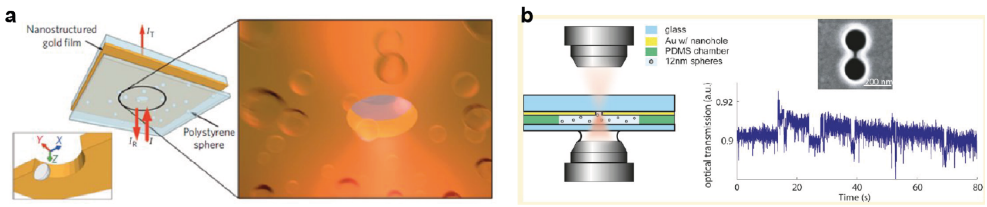

Figure 5.6: **Example of optical trapping using apertures. a**, Schematic diagram of trapping PSs in water with an aperture in a metallic film from [10]. **b**, Double nanohole structure in an Au film for trapping of 12 nm silca nanospheres. The gap size is approximately 15 nm [36].

Optical trapping of PSs of 50 nm and 100 nm with a single aperture was proved above. To trap much smaller particles such as 12 nm silica nanospheres, another structure called double nano hole (DNH) was presented by milling two apertures close to each other so that there is a tiny gap as shown in Fig. 5.6. The gap size in DNH was 15 nm in a 100 nm thick gold film. For the experiment, the confined 80 µm height chamber was made including DNHs on the film and water solution containing 12 nm silica nanospheres. A x100 oil immersion microscope objective (1.25 NA) was used to provide 1.1 µm beam diameter and less than 10 mW optical power was used. Then, trapping events were observed in the time evolution of the transmitted intensity, showing abrupt jumps.

5.2.2 FRET theory

FRET is a mechanism depicting energy transfer between two fluorophores, donor and acceptor [39]. The emission energy of the donor is required to be comparable to the excitation energy of the acceptor, as shown in Fig. 5.7**a**. The donor can be excited by an incident light whose energy is larger than the bandgap ($S_1 - S_0$). Excited electrons at the higher energy and vibration states may lose some energy and return to the lowest singlet exited state (S_1) due to vibrational relaxation. When it come to a single dye molecule, the excited electrons at S_1 relax back to the ground state (S_0) with simultaneous fluorescent light emission. On the other hands, with an acceptor molecule nearby, FRET may occur and transfer the energy to excite electrons in the acceptor molecule. Subsequently, fluorescent emission of the acceptor molecule occurs. The distance between both fluorophores must be less than 20 nm and the mechanism is governed by a short-range dipole-dipole coupling.

The FRET requires an overlap between the emission spectrum of donor and the excitation

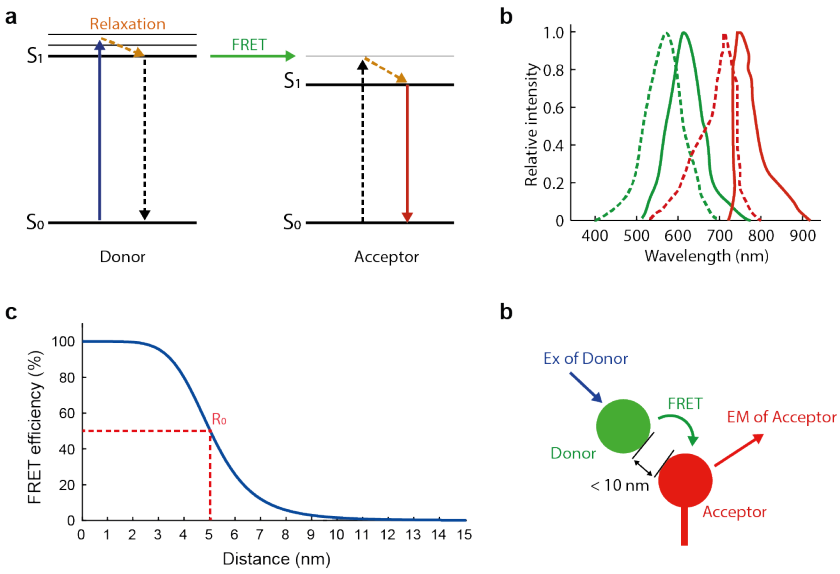

Figure 5.7: **Principle of FRET. a**, Band structure of donor and acceptor molecules. **b**, Spectral intensity of excitation and emission spectra of donor and acceptor. **c**, FRET efficiency is as a function of the distance between donor and acceptor. **d**, Schematic of FRET mechanism.

spectrum of acceptor (Fig. 5.7**b**). The energy transfer rate, k_t, given by [297]:

$$k_t = 8.785 \times \frac{10^{-25} k^2 J(\lambda) k_F}{r^6 \mu^4}, \tag{5.6}$$

where k is the mutual orientation of the dipole moments for both fluorophores, $J(\lambda)$ is the spectral overlap between the emission of the donor and the excitation of the acceptor, k_f resents the fluorescent transition, r is the distance between both fluorophores, and μ is the refractive index of the surrounding medium. Fig. 5.7**c** shows the efficiency E_{FRET} defined as

$$E_{FRET} = \frac{R_0^6}{R_0^6 + r^6}, \tag{5.7}$$

where R_0 is the Förster distance (FRET is also sometimes called Förster resonance energy transfert). FRET pairs can be chosen accordingly, by considering the spectral overlap, the Förster distance, and the energy transfer rate. The schematic of the FRET mechanism between donor and acceptor is depicted in Fig. 5.7**d**.

5.3 Methods

Process flow

For the optical measurement, a micro-chamber containing plasmonic structures and solution is built with a spacer. The process flow is sequentially presented in Fig. 5.8. First of all, SiO_2 substrates are cleaned with Acetone and IPA. 1 nm of Cr for the adhesion and 100 nm (or 200 nm) of Au films are deposited on the substrate. FIB milled nanoscale structures. A buffer layer (-OH functionalized multi walled carbon nanotubes 30–50 nm) can be implemented to avoid the quenching of emission from dyes on the surface. Subsequently, the surface functionalization immobilizes molecules with dyes. The micro-chamber is completed by putting a 120 µm spacer on the side, filling up with solute (functionalized PS beads) and solvent, and covering with a top cover glass.

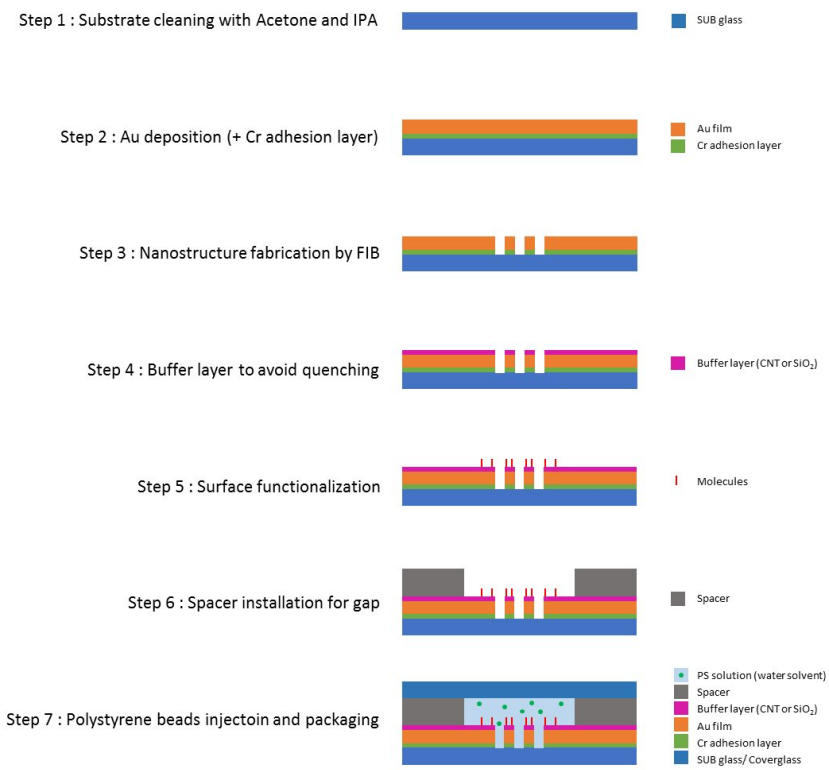

Figure 5.8: **Process flow for optical trapping and FRET experiment.**

Plasmonic structures fabrication using focused ion beam (FIB) milling

The FIB system (Nova 600 NanoLab) in CMi is a dual beam SEM/FIB for nanoscale characterization and analysis. It joins ultra-high resolution field emission SEM and FIB etch and deposition. The eucentric working distance for both SEM and FIB is 5 mm. An oil-free vacuum system is applied to allow for operation at ultra high vacuum, 10^{-10} mbar. The electron source is a Schottky field emitter with a voltage ranging from 200 V to 30 kV and a beam current less than 20 nA. The resolution goes down to 1.1 nm. Secondary electrons and back scattered electrons are detected. For the ion beam, the liquid Gallium ion emitter is used with a voltage ranging from 5 kV to 30 kV and a beam current of 20 nA. The minimum resolution is 7 nm. A CDEM detector is used for direct ion detection. A gas injection system enables the machine to conduct insulator deposition, Pt deposition, insulator etch, and selective carbon mill. FIB is used to fabricate nanoaperture structures in this project.

FRET pair preparation

The Thiol–Au bonding with Mercaptoacid ($C_nH_{2n}O_2S$) leads to carboxyl groups (-COOH) on the surface [322]. The functionalization using carbodiimide crosslinking chemistry has been selected to immobilize dye molecules on the surface [323]. EDC ($C_8H_{17}N_3$) is one of the most used carbodiimide compounds to support carboxyl-to-amine crosslinking [324]. The chemical reaction between EDC and carboxylic acid groups results in the formation of an O-acylisourea intermediate which can be replaced by nucleophilic reaction from primary amino groups. The primary amine, then, constructs a peptide bond with the carboxyl group. The by-product of the reaction, which is a soluble urea derivative, is detached. The efficiency of EDC crosslinking is maximum in an acid buffer (around pH 4.5). MES buffer (4-morpholinoethanesulfonic acid) has been used for the carbodiimide reaction. NHS ($C_4H_5NO_3$) can be often added in EDC carbodiimide crosslinking to enhance the efficiency. The coupling of NHS to carboxyls forms an NHS ester that is much more stable compared to the O-acylisourea intermediate. The ester enables the conjugation to primary amines to be more efficient at around pH 7.4. For the coupling of dye molecules on PS beads, carboxylated PS beads with 100 nm, 200 nm, and 500 nm in diameter are purchased from Polyscience, Inc. The carboxylic acid group of the beads are also coupled to the amine group of Atto dyes (Atto-tec) by the carbodiimide method (Technical data sheet 238C, Polyscience).

Buffer layer deposition

Generally, when a fluorescent molecule and a metal surface have a distance of 5 nm or less, the fluorescent light emitted from a molecule experiences a close-range quenching phenomenon in which the metal absorbs energy [325]. To avoid this quenching issue, a thin buffer layer can be used between the fluorescent groups and the metal surface. One such buffer layer candidate is multi wall carbon nanotubes (MWCNTs). MWCNTs with carboxyl (-COOH), whose thickness is 20 nm, are used to functionalize the Au surface. To immobilize MWCNTs, thiol molecules, which are hydrophilic and attract CNTs containing -COOH, are used to functionalize the Au surface with apertures. The dicyclohexylcarbodiimide method bonds the carboxyl groups of thiol and MWCNTs [326].

Measurement setup

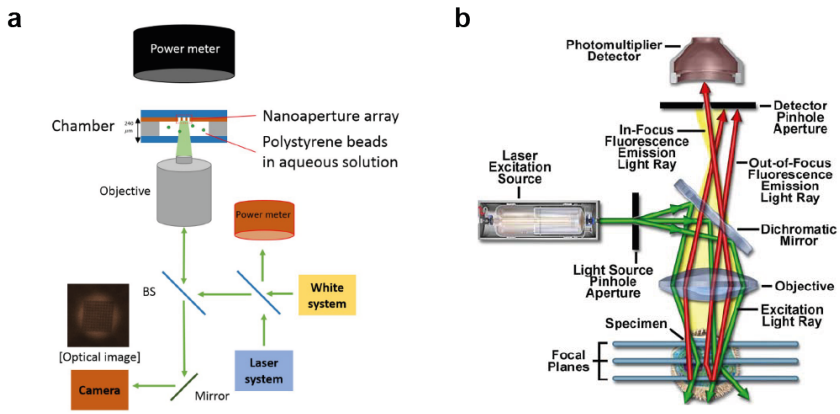

Figure 5.9: **Schematics of experimental measurement setup. a**, Transmitted light intensity measurement setup, which is designed for optical trapping with nanoapertures. **b**, Confocal laser scanning microscopy setup built with a pinhole and PMT detectors [327].

A measurement setup for the optical trapping is built based on the commercial microscope (IX71, Olympus) with objective lenses (NA0.7, 60X, Olympus and NA0.35, 20X, Spindler & Hoyer) and a powermeter (1918-C, Newport), as illustrated in Fig. 5.9**a**. White light from a halogen lamp is introduced from the bottom. The 1064 nm laser (Roithner LaserTechnick) is guided to the objective lens and is focused onto plasmonic nanostructures in a microchamber. The powermeter behind the microchamber measures the transmitted light intensity. A camera is installed to record the experiment. A reference powermeter is placed to control the trapping signal. A dark-field setup has also been used for opto-thermophoretic trapping (Fig. 3.16. Figure 5.9**b** shows a schematic of a confocal microscope. A pinhole aperture in front of the photomultiplier (PMT) detector blocks out-of-focus light so that it enhances optical resolution

and contrast. For the confocal microscopy measurement, Leica SP8 FLIM and Leica SP8 STED 3X setups are used in BIOP, EPFL.

5.4 Experimental results

5.4.1 Plasmonic nanostructures and their spectral properties

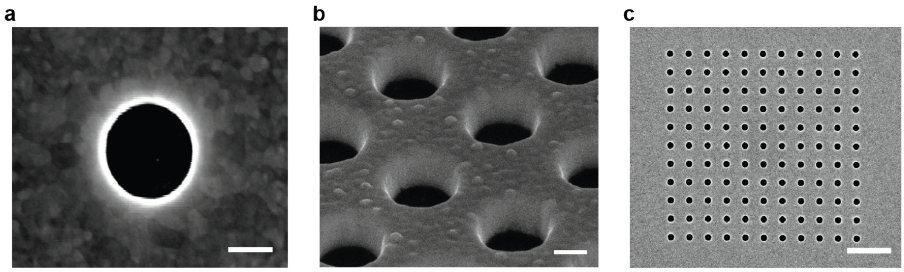

Figure 5.10: **SEM images of nanoapertures. a**, Subwavelength aperture is milled in a 200 nm thick Au film (scale bar: 150 nm). **b**, Tilted view of an 11 × 11 array of nanoapertures is presented. The period of the array is 600 nm (scale bar: 150 nm). **c**, Top view of the same array is displayed (scale bar: 1.5 μm).

We fabricated nanoplasmonic structures and investigated their optical properties in experiment and simulation. A 300 nm single nanoaperture was selected to reproduce self-induced back-action trapping in [10] (Fig. 5.10**a**). The cutoff wavelength of the nanoaperture is 990 nm, and the transmission dramatically decreases for longer wavelengths. Figure 5.10**b** and **c** show an array of nanoapertures, which exert the EOT effect.

The characterization of the aperture arrays for different periodicities has been done experimentally and numerically in Fig. 5.11 for different periods between 440 nm and 760 nm, and the diameter of aperture varying from 200 nm to 400 nm. Figure 5.11**a** shows that surface plasmon modes are red-shifted with a larger period, which corresponds to the simulation results by SIE in Fig.5.11**b**. This is because the periodicity is proportional to the positions of the modes in transmission as shown by Eq. (5.5). In Fig. 5.11**c** and **d**, the aperture diameter is also varied for experiments and simulations. The diameter does not change the positions of the modes but it increases the intensities in transmission.

To understand the optical trapping of nano particles with a periodic array of apertures, a computation has been done with SIE. A simple structure has been designed so that a 350 nm aperture in a 100 nm thick Au thin film exists on a 680 nm × 680 nm glass substrate. After the geometry definition, triangular meshes are generated on the surface to discretize its surfaces. We decrease the mesh size near the aperture rim to obtain accurate results. For the refractive

indices of Au and Silicon dioxide, Johnson and Christy data are used[250].

The SIE system calculates electric and magnetic currents, assuming the simple structure is a unit cell and repeats in both directions. The incident light, whose wavelength is 765 nm, polarized in x- or y-direction propagates along the -z direction. In Fig. 5.12 the cross-sections of the computed near-field distributions of the total intensities are drawn in the x-z plane. In the x-polarized electric field, two hot spots are seen along the rim of the structure, which corresponds to the trapping sites. Meanwhile, relatively weak fields are observed in the vicinity of the rim with the y-polarized incident electric field. The electric field hot spots lead to strong gradients that can trap particles.

Another way to generate SPPs is to fabricate corrugated grooves around an aperture. The normalized transmission intensity peak can be adjusted with the periodicity of the grooves (Fig. 5.13). The enhancement of transmitted light derives from the coupling of the incident light to SPPs through the grating near the aperture. Note that a single nanoaperture without corrugated gratings also includes surface plasmons. The plasmonic modes are distinct from SPPs propagating on a grating because they are LSPs on the nanoaperture ridge [304]. The LSP excitation results in broad peaks in the transmission spectra. The enhancement in transmission is not strong compared to that of SPPs exerted along a corrugated grating, therefore its spectral modes can be invisible with SPPs.

Surface functionalization with CNTs

In the process flow Fig. 5.8 "Step 4: Buffer layer" is conducted after "Step 3: Nanostructure fabrication by FIB". The order of step 3 and step 4 may be swapped if necessary. Figure 5.14 CNTa is a SEM image of nanoapertures array with MWCNT buffer layer that is made by the swapped order of step 3 and step 4. A droplet of 0.1 mg/mL MWCNT solution with ethanol solvent is dropped on a 200 nm thick Au film on a glass substrate. After the functionalization, nano structures are fabricated on the area where CNTs are deposited by FIB milling. As a result, no CNT appear on apertures whereas CNTs fully cover the metallic surfaces. Figure 5.14 CNTb and CNTc are SEM images of the results after functionalization using thiol between step 3 and 4. The difference in density of CNTs comes from an additional process, oxygen plasma, right after CNT deposition. The oxygen plasma is applied to reduce somewhat the -COOH groups.

The transmission spectrum of the array of apertures with noCNT, CNTa, CNTb, and CNTc are plotted as a function of wavelength in Fig. 5.14. Without CNT (black curve), three peaks at 580 nm, 720 nm, and 830 nm are observed due to EOT modes, corresponding to the experimental

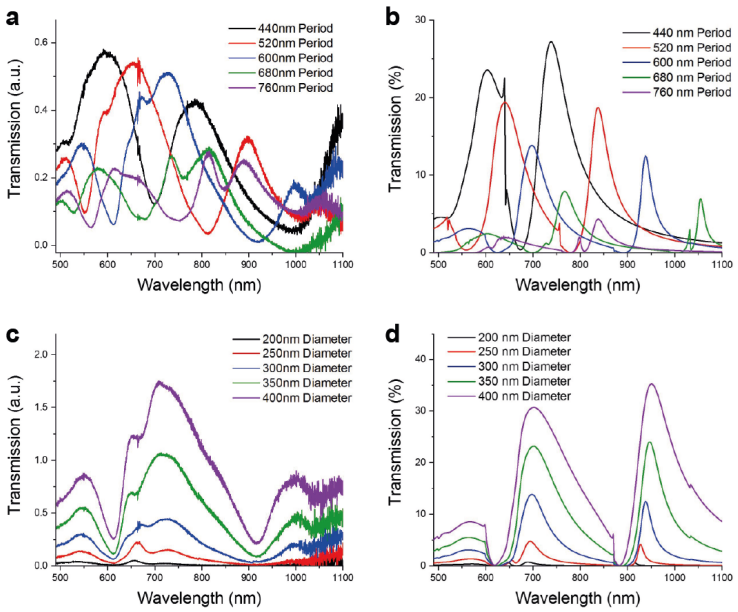

Figure 5.11: **Extraordinary optical transmission.** Experimental (**a**) and computed (**b**) transmission of 440, 520, 600, 680 and 760 nm Period arrays with 300 nm diameter apertures in a 200 nm thick Au film. Experimental (**c**) and computed (**d**) transmission of 600 nm period arrays with 200, 250, 300, 350 and 400 nm diameter apertures in a 200 nm thick Au film. The experimental results are measured by Jobin Yvon TRIAX 550 Spectrometer.

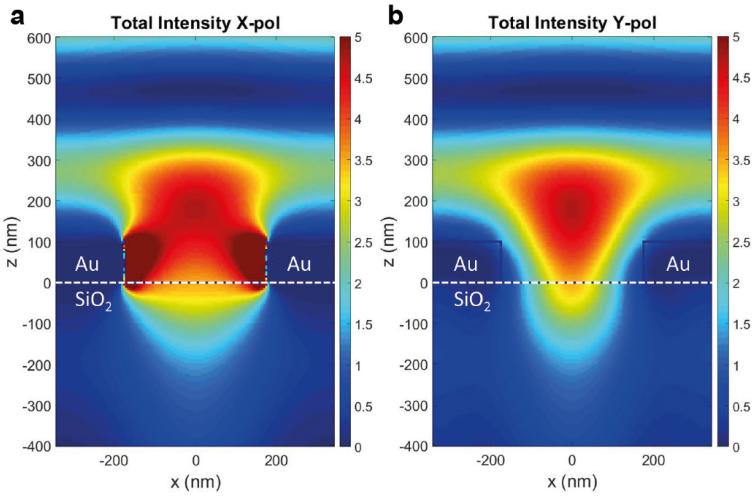

Figure 5.12: **Field intensity distribution. a**, X-polarized light and **b**, Y-polarzied light in x-z plane. Hot spots are observed at the edges of the aperture rim along the direction of the polarization.

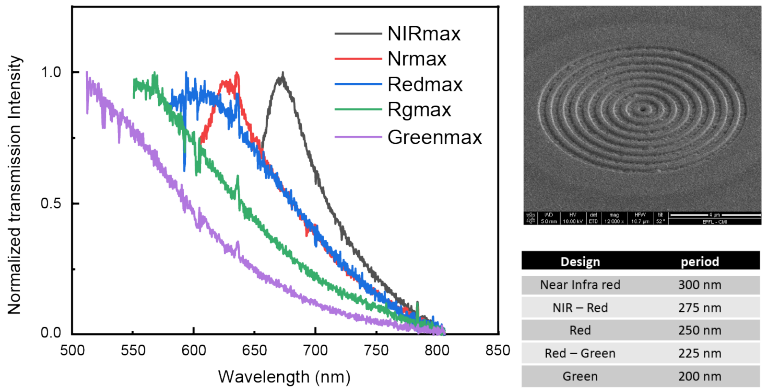

Design	period
Near Infra red	300 nm
NIR – Red	275 nm
Red	250 nm
Red – Green	225 nm
Green	200 nm

Figure 5.13: **Transmission of a nanoaperture with periodic corrugation.** The peak position varies with the period of the corrugation (left). One nanostructure example is imaged by SEM (top right). The table indicates the period and the optical response (bottom right).

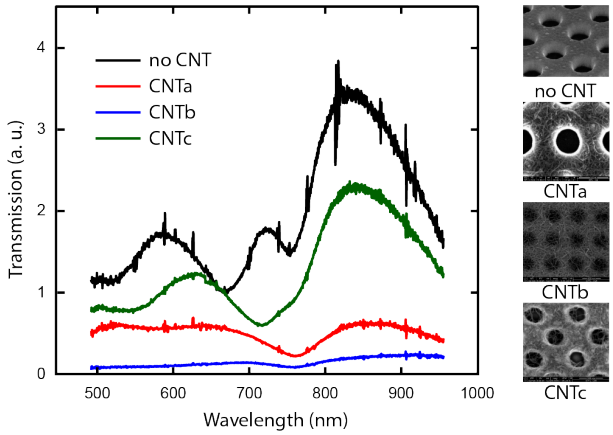

Figure 5.14: **Transmission spectrum with carbon nanotube deposition.** The aperture diameter is 300 nm and the period is 680 nm. The film thickness is 100 nm. Without CNT, plasmonic modes of EOT are present (Black line). CNTa indicates that FIB milling fabricates apertures after CNT film deposition (Red line). CNTb and CNTc obtained CNT films after FIB milling, with different CNT concentrations (Blue and Green lines).

and simulated results in Fig. 5.11. The intensities in transmission dwindle with CNT layers while the overall trajectory is kept due to the almost flat absorption spectrum of MWCNT. CNTb type where CNTs fully cover the apertures and the metal surface has the weakest transmission, as the incident light is incapable of reaching the metal surface. The type of CNTa has fully opened apertures, and CNTs still cover its metal surface. In the red line on Fig. 5.14, the intensity in transmission slightly increases, and the spectrum has a valley at 770 nm. In the case of CNTc, the hydrophilic thiol groups are reduced such that the concentration of CNTs becomes less dense than others. Even though some CNTs exist on aperture, two clear peaks at 680 nm and 840 nm and one weak peak at 750 nm are seen in transmission in the green curve in Fig. 5.14.

There are two remarkable features in these results. One is a red-shift of EOT modes with the CNT functionalization, and another one is a decrease of the 750 nm peak in the green curve. We expect that the red-shift comes from the larger dielectric constant of CNT than air. For the decrease, the difference between local and propagating surface plasmon modes is probably related to the phenomenon. We assume that two local modes at 580 nm and 830 nm still survive and a propagating mode at 720 nm diminishes the most because of CNTs covering the metallic film.

5.4.2 Optical trapping for FRET

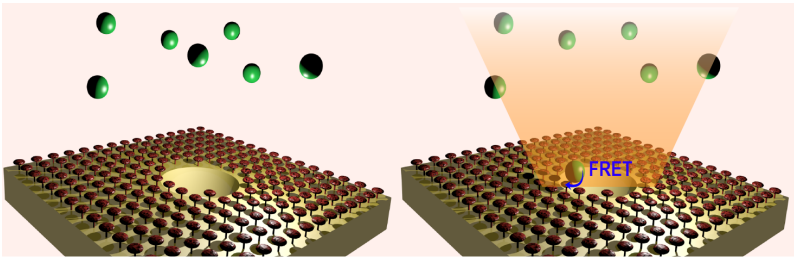

Figure 5.15: **Schematic of FRET experiments.** A metallic film is functionalized with FRET acceptors and has an aperture in the center (left). When a focused laser beam is turned on, a particle coated with FRET donor is trapped in the vicinity of the aperture (right). When the two FRET pairs are close enough, FRET occurs and release the emission of acceptors.

As described in the Motivation section and calculated in SIE (Fig. 5.12), the confinement of the field intensity is exploited with plasmonic nanostructures for optical trapping. This phenomenon means that the trapping place and the trapping target get closer. When they are close enough, FRET can occur as described in Fig. 5.15. For this, FRET pairs were first selected and I checked then to see if the energy transfer between them took place.

Control experiment for FRET

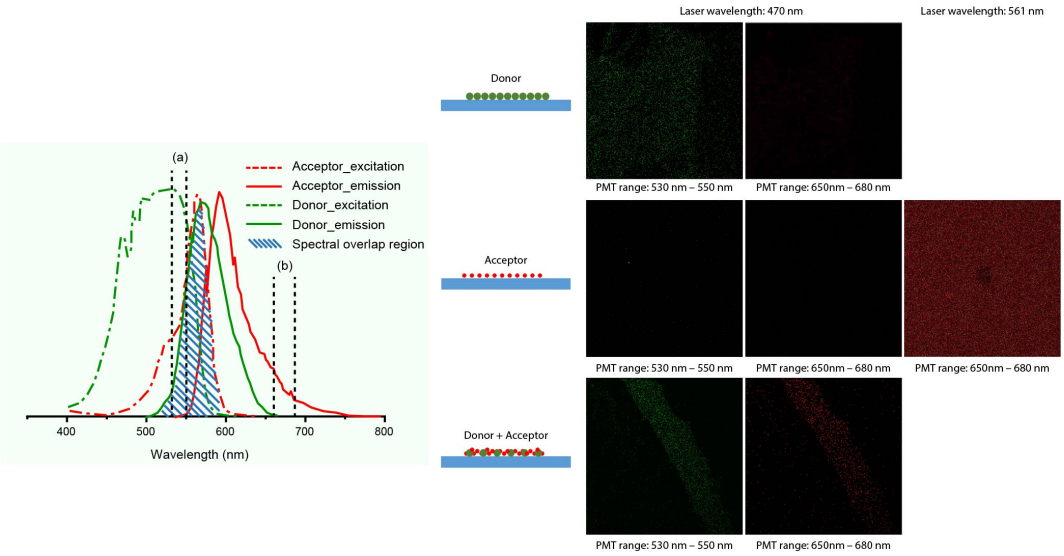

Figure 5.16: **Specification of the selected donor and acceptor FRET pair.** Spectral overlap region exists over the emission of acceptor and the excitation of donor. (a) and (b) regions are the regions of interest for the measurements (left) and the FRET control experiments (right). Thin films of donor and/or acceptor are spin-coated on the glass substrate. Two laser wavelengths are selected as 470 nm and 561 nm to excite both donor and acceptor. PMT has two ranges, from 530 nm to 550 nm and from 650 to 680 nm. A FRET response is detected at PMT range from 650 nm to 680 nm with the 470 nm laser.

Excitation and emission spectra of the donor and acceptor are presented in Fig. 5.16 (Left). The deviant crease lines indicate spectral overlap for FRET. The photomultiplier tubes (PMT) have two detection ranges, one is from 530 nm to 550 nm (a) and the other is from 650 to 680 nm (b). Two dyes are dispersed in ethanol and are spin-coated on glass substrates. Figure 5.16 (Right) shows that a 470 nm laser can excite donor molecules and get the signal from (a). The same laser is used to excite the acceptor molecules. However, there is no significant signal from (a) and (b). With a 561 nm laser, it shows the signal almost everywhere due to the surface functionalization. A mixture of donor and acceptor molecules gives the signal from (a) and (b). According to the FRET theory, the excited donor transfers its energy to the acceptor and radiates no light. Nevertheless, the donor aggregate still shows the signal since the upper parts of the aggregates are far from the acceptors on the surface.

Optical trapping

Variations in the transmission intensity can track the presence of particles in the vicinity of the nanostructure because of the change of surrounding refractive index near the structure.

PS beads used for trapping have a refractive index n = 1.57, which is larger than that of water, n = 1.3. PS beads trapped make the nanostructure appear larger, thereby increasing the transmitted intensity [10]. A 1064 nm laser beam is focused by a X60 (0.70 NA) objective and keeps illuminating more than 30 min to be stabilized before the trapping experiment starts. The power intensity linearly increases as the percent of output power grows. The beam diameter used in the measurement was around 2 μm. The reliable power density for the optical trapping in the literature is approximately 0.16 - 0.32 mW/μm^2 (0.5 mW to 1 mW, in intensity within 2 um of beam diameter) [10]. We observe in Fig. 5.17 that the illumination power is sufficient for trapping. In Fig. 5.17 the laser is exposed on the sample chamber, and the transmitted intensities are measured. The overall power is approximately three orders of magnitude weaker than that of the incident light because of the chamber and sample. Nevertheless, the transmitted intensity still linearly increases with the laser intensity. It is found that sudden jumps are observed in the time evolution of the intensity. Two distinguishable states occur. When the trapping laser is on again after release by a shutter, the intensity always starts at the low state. It implies that PS beads immediately move away from the trap site due to the Brownian motion. With a higher refractive index than water, a PS particle trapped in the aperture enables the aperture to appear larger, which provides for more transmitted light at longer wavelengths than the cutoff point. Figure 5.18 shows a sequence of optical trapping and exhibits the enlargement of the aperture due to trapping.

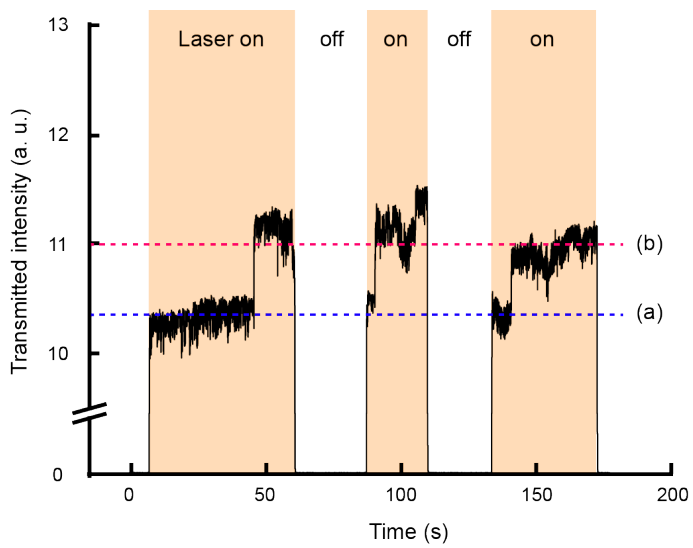

Figure 5.17: **Optical trapping of PS beads.** The time evolution of transmission intensity is plotted. When the laser shutter is on, initial transmission intensity is close to (a) position (Blue dashed line). After a while (40 s in the case of the first "laser on"), an abrupt increase in intensity is detected around (b) position (Red dashed line).

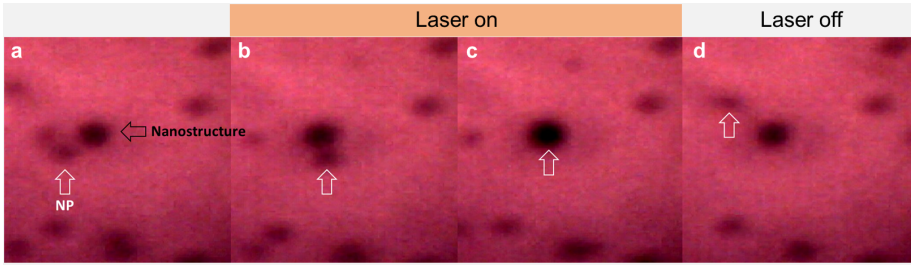

Figure 5.18: **Sequence of optical trapping of a PS bead.** Nanoparticle (NP) and nanoaperture are indicated by white and black arrows, respectively. **a**, the NP is in the vicinity of the nanoaperture. **b – c**, the NP is dragged toward the nanoaperture when the laser is on and focused around the nanostructure. once the NP is trapped, the black hole of the nanoaperture becomes bigger and darker. **d**, without laser, the NP is released.

Optical trapping for FRET

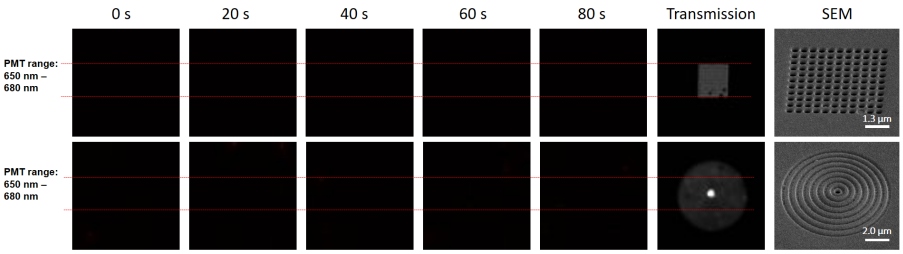

Figure 5.19: **FRET experiments with confocal microscopy.** PMT ranges are set according to Fig. 5.16. A nanoaperture array and a bull's eye structure with functionalized surfaces are used to perform the experiments.

In the confocal setup (Fig. 5.9**b**), the optical trapping experiment for FRET was conducted (Fig. 5.19). On the far right, SEM images show the nanofabrication results. The brighter parts of the transmission column indicate the enhancement of transmitted light through the plasmonic structures. The red dashed lines indicate the position of the trap site. PMT with a range for the acceptor detected no signal: it was difficult to measure the FRET signal. Two possibilities can be considered for that, the first one is the absence of the FRET phenomenon, and the second one is that the signal was too weak to be detected. The first hypothesis means that the distance between both fluorophores is too large to transfer their energy (> 20 nm). We decided to conduct another trapping mechanism, opto-thermophoretic manipulation, to check the distance issue.

This trapping mechanism can control the particle-particle gap from a few nanometers to tens of nanometers [295] (Fig. 5.20). Two donor and acceptor dyes are separately functionalized on PS beads. Although dark-field imaging can distinguish two greenish and reddish colors

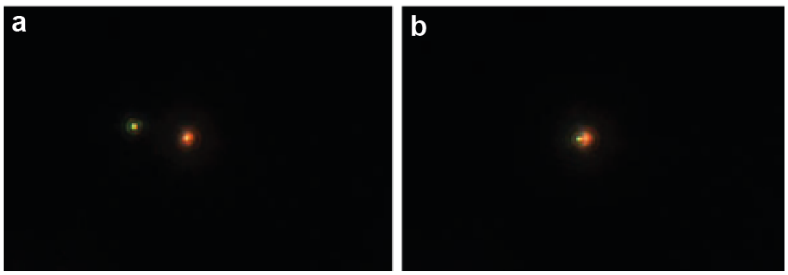

Figure 5.20: **FRET experiments using opto-thermophoretic trapping. a**, Two different dyes are implemented on the nanoparticles before the opto-thermophoretic trapping experiment. **b**, The trapping laser is on, and two particles are combined.

from donors and acceptors, it still doesn't show the FRET signal. So we can think about the aforementioned second possibility. Subsequently, we have tried to increase the exposure time up to 10 min to obtain more signal. Nevertheless, the detection of the FRET signal was not possible. A series of robust measurement tools, a combination of dark-field and confocal setups with flexibility for various laser wavelength injection and a high-performance spectrometer, would be required to pursue these experiments further. Adjusting the distance between the particles and the trap site might be challenging, so it would be better to start experiments for particles assembling onto the surface. This would give us maximum efficiency for the FRET exchange 5.7. Optical assembling for FRET would solve the two issues mentioned above, which indicates that the distance between the FRET pairs becomes almost zero and the FRET efficiency is maximized [328, 329, 330].

5.5 Summary

The visualization of optical trapping with FRET has started with the motivation that it would have useful applications in optical trapping and manipulation. The theoretical studies on aperture-type plasmonic nanostructures, optical trapping, and FRET mechanism have been described. Nanoaperture arrays and a single aperture with corrugated gratings have been selected and fabricated to trap particles with donor molecules. Acceptor molecules have been immobilized on the trap site for FRET.

The different methods for these experiments have been described in detail. FIB milling has fabricated plasmonic nanostructures for trapping experiments. SEM images have shown outstanding yields in nanofabrication. The periodicities of the array and bull's eye structure have controlled their spectral responses. To avoid the quenching issue, buffer layers have been implemented between the fluorescent dyes and the metallic substrate. The FRET pair selection

has been carried out, considering the spectral overlap, the FRET signal distinguishability, and the energy transfer rate. The carbodiimide method using EDC and NHS has formed peptide bonds between carboxyl and amine groups. A microchamber has integrated the plasmonic structure, and FRET pairs with a 150 µm height spacer. For the measurement, a standard optical microscope, a dark-field setup, and a confocal microscope were used.

The experimental results have shown that optical trapping with plasmonic structures was successful. The time evolution of the transmitted intensity abruptly increased when a particle, whose refractive index was higher than the surrounding medium, was trapped. In bright field imaging, the nanoaperture appeared larger with a trapped particle. The FRET pair control experiment proved that FRET occurred when the pairs were close enough. Unfortunately, the combination of optical trapping and FRET has not yet been successful. Also, the Opto-thermophoretic trapping hasn't been able to show the FRET effect. To move forward, optical assembling would be meaningful prior to optical trapping for FRET.

6 Conclusion and outlook

This thesis has mainly been dedicated to developing nanofabrication technologies in order to implement optical manipulations such as the rotation and the trapping of particles at the nanoscale. In particular, rotary motion can be realized in various configurations such as reflection, refraction, absorption, and scattering, although the main principle is as simple as to transfer light momentum into mechanical momentum. I reviewed published papers in chronological order to see how advanced the technology has been so far and what needs to be done to move forward. Then, I found the fact that there is some degrees of freedom in the geometry of nanostructures for rotational movement. Machine learning technologies that currently influence diverse science fields have become mature enough to be implemented. Accordingly, I have tried to apply machine learning algorithms to generate nanostructures with improved optical torques by developing a torque predictor and a nanorotor generator. Subsequently, I have faced difficulties in realizing the structures suggested by the nanorotor generator due to the inherent fabrication limit in up-to-date nanofabrication technologies. Nevertheless, to reach the best results, the IBE process has been optimized as much as possible.

In Chapter 2, a comprehensive literature review has been carried out to show the chronological advances of optically-driven micro- and nano-motors. First, the physical properties and applications of three light momenta driving motors were elucidated. Subsequently, the energy transfer methods from each light momentum to mechanical motions of the motors were described in detail. Intriguingly, it was apparent that these advances were made possible by advances in micro- and nano-fabrication, as the required feature size gradually decreased. Furthermore, the plasmonic resonances observed at the subwavelength size in metal structures have also been applied to enhance the devices efficiencies. As an outlook, new directions such as machine learning, new materials, and metasurfaces were also presented. Those three

methods proposed to improve the motor's performance are very promising and synergies can be built among them.

In Chapter3, optically-driven nanomotors are designed by machine learning algorithms, numerically analyzed with the SIE method, and realized using nanofabrication technologies. All the tasks started from a computation calculating an optical torque from a specific geometry. The torque value remains with any orientations of incident polarization, which is suitable for a rotary motor. To generate nanorotor structures with improved torques, a torque predictor and a nanorotor generator have been considered. The torque predictor consisting of convolutional layers has been trained to predict a torque value from an input image. The random number function in Matlab was used to produce the random set of motor geometries for the training. The nanorotor generator was created by combining a conventional DCGAN with the previously trained torque predictor. The combined torque predictor provides torques of newly generated motors as an additional objective loss function during the training. After several iterations, the trained nanorotor generator produces nanorotor designs with improved torques of more than two orders of magnitude on average, compared to the randomly generated motors. The optical properties of generated motors have been computed using SIE to figure out the torques origin. A maximum optical torque was observed at the plasmon resonance, when field intensity hotspots are excited around the sharp geometrical features of the rotor. Complicated Poynting vector distributions are observed near these hotspots. The angular momentum of the scattered light, corresponding to the integral of the vector product between location and Poynting vectors of the scattered light around the nanorotors, exhibits the opposite responses to the optical torque while the incident light possesses no angular momentum. This implies that momentum exchange occurs between the scattered light and the nanorotor. After the optimization of the machine learning algorithms and the numerical analysis using SIE, the fabrication process flow for free-standing nanomotors was developed. Top-down approaches using EBL have been applied to the fabrication of the motors. To realize the nanorotors with feature sizes around 10 nm, the IBE process was used with HSQ masks patterned by EBL. For nanomotors, a lift-off process with PMMA and anisotropic dielectric etching was used to form SiO_2 embodiments. Finally, an isotropic dry etching process released the nanomotors from the substrate. Nanomotors exhibit much improved rotational speed with a given laser power density in the measurement. However, some of them showed lower performances compared to the theoretical calculations. According to SIE calculations for damaged structures with expansion or shrinkage, this performance degradation might come from an imperfect structure. I believe that it will be solved with the advent of improved nanofabrication technologies.

The optimization of the IBE described in this thesis (Chapter 4) has become an essential step to make a bridge connecting an ideal suggestion from machine learning algorithms and an actual real nanostructure. Without the optimization, the angular distribution of material during etching leads to fences on the sidewall due to the redeposition of etched materials nearby, although the EBL with HSQ resists provides almost perfect nanostructures as designed. I optimized the IBE process to manufacture plasmonic structures such as antennas, flowers, T-shapes, spirals, wheel motors with arbitrary design, and gammadions. Consequently, the extent of this fencing was sensitive to the thickness of the HSQ and Cr layers. Dummy structures and Au wet etching suppressed the formation of fences. The optimized configuration will be beneficial to precisely fabricate plasmonic nanostructures and metasurfaces.

Besides, the visualization of optical trapping with plasmonic structures using FRET (Chapter 5) has been attempted experimentally. The trap sites, nanoaperture structures, have been fabricated using FIB milling on Au films with periodic configurations. Using the carbodiimide crosslinker, FRET pairs, donor and acceptor, were immobilized on trapping particles and trap sites. The optical trapping with nanoapertures has been carried out within a microchamber. The transmission intensity suddenly increased due to the increase in the surrounding refractive index when a particle with a higher refractive index than water is trapped in the aperture. Two FRET pairs were selected considering the energy transfer rate and purchased from an industrial company. Although each experiment has proved successful, the results of the combined experiment have yet to meet the target. The two main reasons that may be presented for this are the following: First, optical trapping may not be able to shrink the distance between the two FRET pairs sufficiently, and second, the emission intensity from the acceptor is too weak to be measured by microscopy. To confirm these issues, an optical trapping experiment can be replaced with an optical assembling experiment in which particles are completely attached to the trap site. This is a completely new experiment, and all the requirements have to be thoroughly looked at from the onset.

As an outlook, machine learning has rapidly developed and applied to diverse fields since it revealed its great potential in the middle of 2010. Therefore, it will certainly contribute more and more to optimizing various optical properties in nano-optics. On the other hand, the solutions suggested by machine learning contain no physical insights that explain the basis of the improvement. Therefore, various methods for interpreting this are also expected to develop at the same time. In this thesis, the machine learning algorithms improved the optical torques for planar Au nanostructures. An interesting extension would be the same thing in 3D. Dielectric and metallic motors described the state-of-the-art in Chapter 2 have developed from

2D to 3D, enhancing their performances. The optimization of the algorithm and fabrication for 3D plasmonic motors might be challenging but worth trying. One can easily imagine that other optical devices, such as metasurfaces and phase gratings, can also be improved further thanks to the globality of machine learning algorithms. The input parameters that I paired were a nanorotor geometry and an optical torque value. The latter can be replaced with any other optical property. The fundamental limits of the nanofabrication have restricted the realization of all the suggestions from the nanorotor generator, although the IBE optimization led to nanostructure feature sizes close to 10 nm. As the resolution of the nanofabrication is gradually improving thanks to the tremendous efforts made by research and industry, the feasible nanofabrication resolution will end up satisfying the suggestions from the machine learning algorithms.

In conclusion, this thesis unfolds a diverse range of possible future directions, where the different technologies I have introduced could be further improved and applied for applications in nano-optics, nanomotors, trapping, and nanofabrication.

Bibliography

[1] A. Ashkin, J. M. Dziedzic, J. E. Bjorkholm, and S. Chu. Observation of a single-beam gradient force optical trap for dielectric particles. *Opt. Lett.*, 11(5):288–290, 1986.

[2] David G. Grier. A revolution in optical manipulation. *Nature*, 424(6950):810–816, 2003.

[3] Domna G Kotsifaki and Síle Nic Chormaic. Plasmonic optical tweezers based on nanostructures: fundamentals, advances and prospects. *Nanophotonics*, 8(7):1227–1245, 2019.

[4] Keir C. Neuman and Attila Nagy. Single-molecule force spectroscopy: optical tweezers, magnetic tweezers and atomic force microscopy. *Nature Methods*, 5(6):491–505, 2008.

[5] Hu Zhang and Kuo-Kang Liu. Optical tweezers for single cells. *Journal of the Royal Society interface*, 5(24):671–690, 2008.

[6] M. D. Wang, H. Yin, R. Landick, J. Gelles, and S. M. Block. Stretching dna with optical tweezers. *Biophysical journal*, 72(3):1335–1346, 1997.

[7] Kenneth B Crozier. Quo vadis, plasmonic optical tweezers? *Light: Science & Applications*, 8(1):1–6, 2019.

[8] Daehan Yoo, Kargal L Gurunatha, Han-Kyu Choi, Daniel A Mohr, Christopher T Ertsgaard, Reuven Gordon, and Sang-Hyun Oh. Low-power optical trapping of nanoparticles and proteins with resonant coaxial nanoaperture using 10 nm gap. *Nano letters*, 18(6):3637–3642, 2018.

[9] Weihua Zhang, Lina Huang, Christian Santschi, and Olivier J. F. Martin. Trapping and sensing 10 nm metal nanoparticles using plasmonic dipole antennas. *Nano Letters*, 10(3):1006–1011, 2010.

[10] Mathieu L Juan, Reuven Gordon, Yuanjie Pang, Fatima Eftekhari, and Romain Quidant. Self-induced back-action optical trapping of dielectric nanoparticles. *Nature Physics*, 5(12):915, 2009.

[11] Brian J Roxworthy, Kaspar D Ko, Anil Kumar, Kin Hung Fung, Edmond KC Chow, Gang Logan Liu, Nicholas X Fang, and Kimani C Toussaint Jr. Application of plasmonic bowtie nanoantenna arrays for optical trapping, stacking, and sorting. *Nano letters*, 12(2):796–801, 2012.

[12] Yasuyuki Tsuboi, Tatsuya Shoji, Noboru Kitamura, Mai Takase, Kei Murakoshi, Yoshihiko Mizumoto, and Hajime Ishihara. Optical trapping of quantum dots based on gap-mode-excitation of localized surface plasmon. *The Journal of Physical Chemistry Letters*, 1(15):2327–2333, 2010.

[13] Michael P MacDonald, Gabriel C Spalding, and Kishan Dholakia. Microfluidic sorting in an optical lattice. *Nature*, 426(6965):421–424, 2003.

[14] Jun Chen, Jack Ng, Zhifang Lin, and Che Ting Chan. Optical pulling force. *Nature photonics*, 5(9):531–534, 2011.

[15] Zijie Yan, Raman A Shah, Garrett Chado, Stephen K Gray, Matthew Pelton, and Norbert F Scherer. Guiding spatial arrangements of silver nanoparticles by optical binding interactions in shaped light fields. *ACS nano*, 7(2):1790–1802, 2013.

[16] Gavin Sinclair, Pamela Jordan, Johannes Courtial, Miles Padgett, Jon Cooper, and Zsolt John Laczik. Assembly of 3-dimensional structures using programmable holographic optical tweezers. *Optics Express*, 12(22):5475–5480, 2004.

[17] D. L. Gao, W. Q. Ding, M. Nieto-Vesperinas, X. M. Ding, M. Rahman, T. H. Zhang, C. Lim, and C. W. Qiu. Optical manipulation from the microscale to the nanoscale: fundamentals, advances and prospects. *Light-Science & Applications*, 6, 2017.

[18] P. Galajda and P. Ormos. Rotors produced and driven in laser tweezers with reversed direction of rotation. *Applied Physics Letters*, 80(24):4653–4655, 2002.

[19] R. A. Beth. Mechanical detection and measurement of the angular momentum of light. *Physical Review*, 50(2):115–125, 1936.

[20] M. E. J. Friese, J. Enger, H. RubinszteinDunlop, and N. R. Heckenberg. Optical angular-momentum transfer to trapped absorbing particles. *Physical Review A*, 54(2):1593–1596, 1996.

[21] M. E. J. Friese, T. A. Nieminen, N. R. Heckenberg, and H. Rubinsztein-Dunlop. Optical alignment and spinning of laser-trapped microscopic particles. *Nature*, 394(6691):348–350, 1998.

[22] L. Shao, Z. J. Yang, D. Andren, P. Johansson, and M. Kall. Gold nanorod rotary motors driven by resonant light scattering. *Acs Nano*, 9(12):12542–12551, 2015.

[23] M. Liu, T. Zentgraf, Y. M. Liu, G. Bartal, and X. Zhang. Light-driven nanoscale plasmonic motors. *Nature Nanotechnology*, 5(8):570–573, 2010.

[24] Z. J. Yan and N. F. Scherer. Optical vortex induced rotation of silver nanowires. *Journal of Physical Chemistry Letters*, 4(17):2937–2942, 2013.

[25] E. Higurashi, O. Ohguchi, T. Tamamura, H. Ukita, and R. Sawada. Optically induced rotation of dissymmetrically shaped fluorinated polyimide micro-objects in optical traps. *Journal of Applied Physics*, 82(6):2773–2779, 1997.

[26] P. Galajda and P. Ormos. Complex micromachines produced and driven by light. *Applied Physics Letters*, 78(2):249–251, 2001.

[27] C. L. Lin, G. Vitrant, M. Bouriau, R. Casalegno, and P. L. Baldeck. Optically driven archimedes micro-screws for micropump application. *Optics Express*, 19(9):8267–8276, 2011.

[28] A. Lehmuskero, R. Ogier, T. Gschneidtner, P. Johansson, and M. Kall. Ultrafast spinning of gold nanoparticles in water using circularly polarized light. *Nano Letters*, 13(7):3129–3134, 2013.

[29] P. H. Jones, F. Palmisano, F. Bonaccorso, P. G. Gucciardi, G. Calogero, A. C. Ferrari, and O. M. Marago. Rotation detection in light-driven nanorotors. *Acs Nano*, 3(10):3077–3084, 2009.

[30] Z. J. Yan, J. Sweet, J. E. Jureller, M. J. Guffey, M. Pelton, and N. F. Scherert. Controlling the position and orientation of single silver nanowires on a surface using structured optical fields. *Acs Nano*, 6(9):8144–8155, 2012.

[31] Y. E. Lee, K. H. Fung, D. Jin, and N. X. Fang. Optical torque from enhanced scattering by multipolar plasmonic resonance. *Nanophotonics*, 3(6):343–350, 2014.

[32] L. Shao and M. Kall. Light-driven rotation of plasmonic nanomotors. *Advanced Functional Materials*, 28(25), 2018.

[33] J. W. Liaw, Y. S. Chen, and M. K. Kuo. Rotating au nanorod and nanowire driven by circularly polarized light. *Optics Express*, 22(21):26005–26015, 2014.

[34] Wei Ma, Zhaocheng Liu, Zhaxylyk A Kudyshev, Alexandra Boltasseva, Wenshan Cai, and Yongmin Liu. Deep learning for the design of photonic structures. *Nature Photonics*, 15(2):77–90, 2021.

[35] Pau Mestres, Johann Berthelot, Srdjan S Aćimović, and Romain Quidant. Unraveling the optomechanical nature of plasmonic trapping. *Light: Science & Applications*, 5(7):e16092–e16092, 2016.

[36] Yuanjie Pang and Reuven Gordon. Optical trapping of 12 nm dielectric spheres using double-nanoholes in a gold film. *Nano letters*, 11(9):3763–3767, 2011.

[37] Xue Han, Viet Giang Truong, and Síle Nic Chormaic. Efficient microparticle trapping with plasmonic annular apertures arrays. *Nano Futures*, 2(3):035007, 2018.

[38] Amr AE Saleh and Jennifer A Dionne. Toward efficient optical trapping of sub-10-nm particles with coaxial plasmonic apertures. *Nano letters*, 12(11):5581–5586, 2012.

[39] Robert M Clegg. Fluorescence resonance energy transfer. *Current opinion in biotechnology*, 6(1):103–110, 1995.

[40] J. P. Lafleur, A. Jonsson, S. Senkbeil, and J. P. Kutter. Recent advances in lab-on-a-chip for biosensing applications. *Biosensors & Bioelectronics*, 76:213–233, 2016.

[41] J. X. Li, B. E. F. de Avila, W. Gao, L. F. Zhang, and J. Wang. Micro/nanorobots for biomedicine: Delivery, surgery, sensing, and detoxification. *Science Robotics*, 2(4), 2017.

[42] Jinxing Li, Wei Gao, Renfeng Dong, Allen Pei, Sirilak Sattayasamitsathit, and Joseph Wang. Nanomotor lithography. *Nature communications*, 5(1):1–7, 2014.

[43] Geoffrey A Ozin, Ian Manners, Sébastien Fournier-Bidoz, and André Arsenault. Dream nanomachines. *Advanced Materials*, 17(24):3011–3018, 2005.

[44] K. Kim, J. Guo, Z. X. Liang, F. Q. Zhu, and D. L. Fan. Man-made rotary nanomotors: a review of recent developments. *Nanoscale*, 8(20):10471–10490, 2016.

[45] Richard P. Feynman, Robert B. Leighton, and Matthew L. Sands. *The Feynman lectures on physics*. Addison-Wesley Pub. Co., Reading, Mass., 1963.

[46] X. Z. Chen, M. Hoop, F. Mushtaq, E. Siringil, C. Z. Hu, B. J. Nelson, and S. Pane. Recent developments in magnetically driven micro- and nanorobots. *Applied Materials Today*, 9:37–46, 2017.

[47] L. L. Xu, F. Z. Mou, H. T. Gong, M. Luo, and J. G. Guan. Light-driven micro/nanomotors: from fundamentals to applications. *Chemical Society Reviews*, 46(22):6905–6926, 2017.

[48] K. J. Rao, F. Li, L. Meng, H. R. Zheng, F. Y. Cai, and W. Wang. A force to be reckoned with: A review of synthetic microswimmers powered by ultrasound. *Small*, 11(24):2836–2846, 2015.

[49] F. Peng, Y. F. Tu, and D. A. Wilson. Micro/nanomotors towards in vivo application: cell, tissue and biofluid. *Chemical Society Reviews*, 46(17):5289–5310, 2017.

[50] Bradley J Nelson, Ioannis K Kaliakatsos, and Jake J Abbott. Microrobots for minimally invasive medicine. *Annual review of biomedical engineering*, 12:55–85, 2010.

[51] A. Chalupniak, E. Morales-Narvaez, and A. Merkoci. Micro and nanomotors in diagnostics. *Advanced Drug Delivery Reviews*, 95:104–116, 2015.

[52] George Chatzipirpiridis, Olgaç Ergeneman, Juho Pokki, Franziska Ullrich, Stefano Fusco, José A Ortega, Kartik M Sivaraman, Bradley J Nelson, and Salvador Pané. Electroforming of implantable tubular magnetic microrobots for wireless ophthalmologic applications. *Advanced healthcare materials*, 4(2):209–214, 2015.

[53] J. Wang. Cargo-towing synthetic nanomachines: Towards active transport in microchip devices. *Lab on a Chip*, 12(11):1944–1950, 2012.

[54] E. Hasman. Plasmonics new twist on nanoscale motors. *Nature Nanotechnology*, 5(8):563–564, 2010.

[55] Sabrina Simoncelli, Samuel Johnson, Franziska Kriegel, Jan Lipfert, and Jochen Feldmann. Stretching and heating single dna molecules with optically trapped gold–silica janus particles. *Acs Photonics*, 4(11):2843–2851, 2017.

[56] J. W. Judy. Microelectromechanical systems (mems): fabrication, design and applications. *Smart Materials and Structures*, 10(6):1115–1134, 2001.

[57] KL Ekinci and ML Roukes. Nanoelectromechanical systems. *Review of scientific instruments*, 76(6):061101, 2005.

[58] A. A. G. Requicha. Nanorobots, nems, and nanoassembly. *Proceedings of the Ieee*, 91(11):1922–1933, 2003.

[59] JTM Van Beek and Rob Puers. A review of mems oscillators for frequency reference and timing applications. *Journal of Micromechanics and Microengineering*, 22(1):013001, 2011.

[60] H. A. Stone, A. D. Stroock, and A. Ajdari. Engineering flows in small devices: Microfluidics toward a lab-on-a-chip. *Annual Review of Fluid Mechanics*, 36:381–411, 2004.

[61] Wen Zeng, Ian Jacobi, David J Beck, Songjing Li, and Howard A Stone. Characterization of syringe-pump-driven induced pressure fluctuations in elastic microchannels. *Lab on a Chip*, 15(4):1110–1115, 2015.

[62] J. Leach, H. Mushfique, R. di Leonardo, M. Padgett, and J. Cooper. An optically driven pump for microfluidics. *Lab on a Chip*, 6(6):735–739, 2006.

[63] Hamid A Toliyat and Gerald B Kliman. *Handbook of electric motors*, volume 120. CRC press, 2018.

[64] Yuichi Hiratsuka, Makoto Miyata, Tetsuya Tada, and Taro QP Uyeda. A microrotary motor powered by bacteria. *Proceedings of the National Academy of Sciences*, 103(37):13618–13623, 2006.

[65] V. Magdanz, S. Sanchez, and O. G. Schmidt. Development of a sperm-flagella driven micro-bio-robot. *Advanced Materials*, 25(45):6581–6588, 2013.

[66] A. M. Fennimore, T. D. Yuzvinsky, W. Q. Han, M. S. Fuhrer, J. Cumings, and A. Zettl. Rotational actuators based on carbon nanotubes. *Nature*, 424(6947):408–410, 2003.

[67] D. L. Fan, F. Q. Zhu, R. C. Cammarata, and C. L. Chien. Controllable high-speed rotation of nanowires. *Physical Review Letters*, 94(24), 2005.

[68] Hyung Ju Kim, Sang Ho Lee, Aniruddha A. Upadhye, Insoo Ro, M. Isabel Tejedor-Tejedor, Marc A. Anderson, Won Bae Kim, and George W. Huber. Plasmon-enhanced photoelectrochemical water splitting with size-controllable gold nanodot arrays. *ACS nano*, 8(10):10756–10765, 2014.

[69] L. Zhang, T. Petit, Y. Lu, B. E. Kratochvil, K. E. Peyer, R. Pei, J. Lou, and B. J. Nelson. Controlled propulsion and cargo transport of rotating nickel nanowires near a patterned solid surface. *Acs Nano*, 4(10):6228–6234, 2010.

[70] K. Keshoju, H. Xing, and L. Sun. Magnetic field driven nanowire rotation in suspension. *Applied Physics Letters*, 91(12), 2007.

[71] Nicole Pamme. Magnetism and microfluidics. *Lab on a Chip*, 6(1):24–38, 2006.

[72] Ambarish Ghosh and Peer Fischer. Controlled propulsion of artificial magnetic nanostructured propellers. *Nano letters*, 9(6):2243–2245, 2009.

[73] J. Burdick, R. Laocharoensuk, P. M. Wheat, J. D. Posner, and J. Wang. Synthetic nanomotors in microchannel networks: Directional microchip motion and controlled manipulation of cargo. *Journal of the American Chemical Society*, 130(26):8164–+, 2008.

[74] Qilu Zhang, Renfeng Dong, Yefei Wu, Wei Gao, Zihan He, and Biye Ren. Light-driven au-wo3@ c janus micromotors for rapid photodegradation of dye pollutants. *ACS applied materials & interfaces*, 9(5):4674–4683, 2017.

[75] Mingjun Xuan, Zhiguang Wu, Jingxin Shao, Luru Dai, Tieyan Si, and Qiang He. Near infrared light-powered janus mesoporous silica nanoparticle motors. *Journal of the American Chemical Society*, 138(20):6492–6497, 2016.

[76] Zhiguang Wu, Tieyan Si, Wei Gao, Xiankun Lin, Joseph Wang, and Qiang He. Superfast near-infrared light-driven polymer multilayer rockets. *Small*, 12(5):577–582, 2016.

[77] A. L. Balk, L. O. Mair, P. P. Mathai, P. N. Patrone, W. Wang, S. Ahmed, T. E. Mallouk, J. A. Liddle, and S. M. Stavis. Kilohertz rotation of nanorods propelled by ultrasound, traced by microvortex advection of nanoparticles. *Acs Nano*, 8(8):8300–8309, 2014.

[78] Suzanne Ahmed, Wei Wang, Lamar O Mair, Robert D Fraleigh, Sixing Li, Luz Angelica Castro, Mauricio Hoyos, Tony Jun Huang, and Thomas E Mallouk. Steering acoustically propelled nanowire motors toward cells in a biologically compatible environment using magnetic fields. *Langmuir*, 29(52):16113–16118, 2013.

[79] Yuchao Chen, Xiaoyun Ding, Sz-Chin Steven Lin, Shikuan Yang, Po-Hsun Huang, Nitesh Nama, Yanhui Zhao, Ahmad Ahsan Nawaz, Feng Guo, and Wei Wang. Tunable nanowire patterning using standing surface acoustic waves. *ACS nano*, 7(4):3306–3314, 2013.

[80] L. K. Yang, K. Cai, J. Shi, and Q. H. Qin. Significance tests on the output power of a thermally driven rotary nanomotor. *Nanotechnology*, 28(21), 2017.

[81] Carl Sagan. *Cosmos*, volume 1. Edicions Universitat Barcelona, 2006.

[82] Sybil P Parker. *McGraw-Hill encyclopedia of science & technology.* McGraw-Hill Companies, 1997.

[83] John David Jackson. *Classical Electrodynamics.* Wiley, New York, 3rd edition, 1999.

[84] John Henry Poynting. Xv. on the transfer of energy in the electromagnetic field. *Philosophical Transactions of the Royal Society of London*, 175(175):343–361, 1884.

[85] M Abraham. Zur elektrodynamik bewegter körper, rend. circ. mat. palermo 28 (1909) 1-28; m. abraham. *Sull'elettrodinamica di Minkowski, Rend. Circ. Mat. Palermo*, 30:33–46, 1910.

[86] Hermann Minkowski. Die grundgleichungen für die elektromagnetischen vorgänge in bewegten körpern. *Nachrichten von der Gesellschaft der Wissenschaften zu Göttingen, Mathematisch-Physikalische Klasse*, 1908:53–111, 1908.

[87] Reginald Victor Jones and JCS Richards. The pressure of radiation in a refracting medium. *Proceedings of the Royal Society of London. Series A. Mathematical and Physical Sciences*, 221(1147):480–498, 1954.

[88] A Ashkin and JM Dziedzic. Radiation pressure on a free liquid surface. *Physical Review Letters*, 30(4):139, 1973.

[89] Reginald Victor Jones and B Leslie. The measurement of optical radiation pressure in dispersive media. *Proceedings of the Royal Society of London. A. Mathematical and Physical Sciences*, 360(1702):347–363, 1978.

[90] GB Walker and G Walker. Mechanical forces in a dielectric due to electromagnetic fields. *Canadian Journal of Physics*, 55(23):2121–2127, 1977.

[91] Y. N. Obukhov and F. W. Hehl. Electromagnetic energy-momentum and forces in matter. *Physics Letters A*, 311(4-5):277–284, 2003.

[92] R. V. Jones. Radiation pressure of light in a dispersive medium. *Proceedings of the Royal Society of London Series a-Mathematical Physical and Engineering Sciences*, 360(1702):365–371, 1978.

[93] Rodney Loudon, Stephen M Barnett, and C Baxter. Radiation pressure and momentum transfer in dielectrics: the photon drag effect. *Physical Review A*, 71(6):063802, 2005.

[94] R. Loudon. Radiation pressure and momentum in dielectrics. *Fortschritte Der Physik-Progress of Physics*, 52(11-12):1134–1140, 2004.

[95] M. Mansuripur. Radiation pressure and the linear momentum of the electromagnetic field. *Optics Express*, 12(22):5375–5401, 2004.

[96] James P. Gordon. Radiation forces and momenta in dielectric media. *Physical Review A*, 8(1):14–21, 1973.

[97] R. N. C. Pfeifer, T. A. Nieminen, N. R. Heckenberg, and H. Rubinsztein-Dunlop. Colloquium: Momentum of an electromagnetic wave in dielectric media. *Reviews of Modern Physics*, 79(4):1197–1216, 2007.

[98] E. F. Nichols and G. F. Hull. A preliminary communication on the pressure of heat and light radiation. *Physical Review*, 13(5):307–320, 1901.

[99] Carlos J Bustamante, Yann R Chemla, Shixin Liu, and Michelle D Wang. Optical tweezers in single-molecule biophysics. *Nature Reviews Methods Primers*, 1(1):1–29, 2021.

[100] P. Meystre, E. M. Wright, J. D. McCullen, and E. Vignes. Theory of radiation-pressure-driven interferometers. *Journal of the Optical Society of America B*, 2(11):1830–1840, 1985.

[101] Osamu Mori, Hirotaka Sawada, Ryu Funase, Mutsuko Morimoto, Tatsuya Endo, Takayuki Yamamoto, Yuichi Tsuda, Yasuhiro Kawakatsu, Jun'ichiro Kawaguchi, and Yasuyuki Miyazaki. First solar power sail demonstration by ikaros. *Transactions of the Japan Society for Aeronautical and Space Sciences, Aerospace Technology Japan*, 8(ists27):To_4_25–To_4_31, 2010.

[102] A. Ashkin. Applications of laser radiation pressure. *Science*, 210(4474):1081–1088, 1980.

[103] A. Rohrbach and E. H. K. Stelzer. Trapping forces, force constants, and potential depths for dielectric spheres in the presence of spherical aberrations. *Applied Optics*, 41(13):2494–2507, 2002.

[104] David J Wineland and Wayne M Itano. Laser cooling of atoms. *Physical Review A*, 20(4):1521, 1979.

[105] Uroš Delić, Manuel Reisenbauer, Kahan Dare, David Grass, Vladan Vuletić, Nikolai Kiesel, and Markus Aspelmeyer. Cooling of a levitated nanoparticle to the motional quantum ground state. *Science*, 367(6480):892–895, 2020.

[106] Olivier Arcizet, Tristan Briant, Antoine Heidmann, and Michel Pinard. Beating quantum limits in an optomechanical sensor by cavity detuning. *Physical Review A*, 73(3):033819, 2006.

[107] Albert Einstein. On the development of our views concerning the nature and constitution of radiation. *Phys. Z*, 10(22):817–825, 1909.

[108] TV Liseykina, SV Popruzhenko, and A Macchi. Inverse faraday effect driven by radiation friction. *New Journal of Physics*, 18(7):072001, 2016.

[109] RM Georgevic. The solar radiation pressure on the mariner 9 mars orbiter. *Astronautica Acta*, 18(2):109–115, 1973.

[110] Jerome L Wright. *Space sailing*. Taylor & Francis, 1992.

[111] Harry A Atwater, Artur R Davoyan, Ognjen Ilic, Deep Jariwala, Michelle C Sherrott, Cora M Went, William S Whitney, and Joeson Wong. Materials challenges for the starshot lightsail. *Nature materials*, 17(10):861–867, 2018.

[112] S. Matsuo, S. Kiyama, Y. Shichijo, T. Tomita, S. Hashimoto, Y. Hosokawa, and H. Masuhara. Laser microfabrication and rotation of ship-in-a-bottle optical rotators. *Applied Physics Letters*, 93(5), 2008.

[113] S. Maruo, A. Takaura, and Y. Saito. Optically driven micropump with a twin spiral microrotor. *Optics Express*, 17(21):18525–18532, 2009.

[114] X. F. Lin, G. Q. Hu, Q. D. Chen, L. G. Niu, Q. S. Li, A. Ostendorf, and H. B. Sun. A light-driven turbine-like micro-rotor and study on its light-to-mechanical power conversion efficiency. *Applied Physics Letters*, 101(11), 2012.

[115] Y. Y. Tanaka, P. Albella, M. Rahmani, V. Giannini, S. A. Maier, and T. Shimura. Plasmonic linear nanomotor using lateral optical forces. *Science Advances*, 6(45), 2020.

[116] Satoshi Kawata, Hong-Bo Sun, Tomokazu Tanaka, and Kenji Takada. Finer features for functional microdevices. *Nature*, 412(6848):697–698, 2001.

[117] Andrei V Kabashin, P Evans, S Pastkovsky, W Hendren, Gregory A Wurtz, Ron Atkinson, R Pollard, VA Podolskiy, and Anatoly V Zayats. Plasmonic nanorod metamaterials for biosensing. *Nature materials*, 8(11):867–871, 2009.

[118] J. P. Kottmann, O. J. F. Martin, D. R. Smith, and S. Schultz. Plasmon resonances of silver nanowires with a nonregular cross section. *Physical Review B Condensed Matter and Materials Physics*, 64(23):235402/1–10, 2001.

[119] John B Pendry, Anthony J Holden, David J Robbins, and WJ Stewart. Magnetism from conductors and enhanced nonlinear phenomena. *IEEE transactions on microwave theory and techniques*, 47(11):2075–2084, 1999.

[120] AV Rogacheva, VA Fedotov, AS Schwanecke, and NI Zheludev. Giant gyrotropy due to electromagnetic-field coupling in a bilayered chiral structure. *Physical review letters*, 97(17):177401, 2006.

[121] E. Messina, E. Cavallaro, A. Cacciola, R. Saija, F. Borghese, P. Denti, B. Fazio, C. D'Andrea, P. G. Gucciardi, M. A. Iati, M. Meneghetti, G. Compagnini, V. Amendola, and O. M. Marago. Manipulation and raman spectroscopy with optically trapped metal nanoparticles obtained by pulsed laser ablation in liquids. *Journal of Physical Chemistry C*, 115(12):5115–5122, 2011.

[122] Matthew Pelton, Mingzhao Liu, Hee Y. Kim, Glenna Smith, Philippe Guyot-Sionnest, and Norbert F. Scherer. Optical trapping and alignment of single gold nanorods by using plasmon resonances. *Optics Letters*, 31(13):2075–2077, 2006.

[123] L. M. Tong, V. D. Miljkovic, and M. Kall. Alignment, rotation, and spinning of single plasmonic nanoparticles and nanowires using polarization dependent optical forces. *Nano Letters*, 10(1):268–273, 2010.

[124] S. Maruo and H. Inoue. Optically driven micropump produced by three-dimensional two-photon microfabrication. *Applied Physics Letters*, 89(14), 2006.

[125] Eugene Hecht and A Zajac. Optics, chapter 9. *Addison-Wesley*, 3:384–441, 2002.

[126] CV Raman and S Bhagavantam. "experimental proof of the photon spin. *Indian Journal of Physics*, 6:353–366, 1931.

[127] John Henry Poynting. The wave motion of a revolving shaft, and a suggestion as to the angular momentum in a beam of circularly polarised light. *Proceedings of the Royal Society of London. Series A, Containing Papers of a Mathematical and Physical Character*, 82(557):560–567, 1909.

[128] D. Normanno, M. Capitanio, and F. S. Pavone. Spin absorption, windmill, and magneto-optic effects in optical angular momentum transfer. *Physical Review A*, 70(5), 2004.

[129] Takafumi Fujita, Kazuhiro Morimoto, Haruki Kiyama, Giles Allison, Marcus Larsson, Arne Ludwig, Sascha R Valentin, Andreas D Wieck, Akira Oiwa, and Seigo Tarucha. Angular momentum transfer from photon polarization to an electron spin in a gate-defined quantum dot. *Nature communications*, 10(1):1–6, 2019.

[130] D. R. Abujetas and J. A. Sanchez-Gil. Spin angular momentum of guided light induced by transverse confinement and intrinsic helicity. *Acs Photonics*, 7(2):534–545, 2020.

[131] Wikipedia. Spin Angular Momentum of Light. https://en.wikipedia.org/wiki/Spin_angular_momentum_of_light, 2022. [Online;].

[132] M. E. J. Friese, T. A. Nieminen, N. R. Heckenberg, and H. Rubinsztein-Dunlop. Optical torque controlled by elliptical polarization. *Optics Letters*, 23(1):1–3, 1998.

[133] K. Miyakawa, H. Adachi, and Y. Inoue. Rotation of two-dimensional arrays of microparticles trapped by circularly polarized light. *Applied Physics Letters*, 84(26):5440–5442, 2004.

[134] Marco Capitanio, Davide Normanno, and Francesco Saverio Pavone. High-precision measurements of light-induced torque on absorbing microspheres. *Optics letters*, 29(19):2231–2233, 2004.

[135] S. L. Neale, M. P. Macdonald, K. Dholakia, and T. F. Krauss. All-optical control of microfluidic components using form birefringence. *Nature Materials*, 4(7):530–533, 2005.

[136] MEJ Friese, H Rubinsztein-Dunlop, Julie Gold, Petter Hagberg, and Dag Hanstorp. Optically driven micromachine elements. *Applied Physics Letters*, 78(4):547–549, 2001.

[137] A. La Porta and M. D. Wang. Optical torque wrench: Angular trapping, rotation, and torque detection of quartz microparticles. *Physical Review Letters*, 92(19), 2004.

[138] A. I. Bishop, T. A. Nieminen, N. R. Heckenberg, and H. Rubinsztein-Dunlop. Optical microrheology using rotating laser-trapped particles. *Physical Review Letters*, 92(19), 2004.

[139] G. Knoner, S. Parkin, N. R. Heckenberg, and H. Rubinsztein-Dunlop. Characterization of optically driven fluid stress fields with optical tweezers. *Physical Review E*, 72(3), 2005.

[140] L. Allen, M. W. Beijersbergen, R. J. C. Spreeuw, and J. P. Woerdman. Orbital angular-momentum of light and the transformation of laguerre-gaussian laser modes. *Physical Review A*, 45(11):8185–8189, 1992.

[141] L. Allen, J. Courtial, and M. J. Padgett. Matrix formulation for the propagation of light beams with orbital and spin angular momenta. *Physical Review E*, 60(6):7497–7503, 1999.

[142] L Allen, MJ Padgett, and M Babiker. Iv the orbital angular momentum of light. In *Progress in optics*, volume 39, pages 291–372. Elsevier, 1999.

[143] L. Marrucci, C. Manzo, and D. Paparo. Optical spin-to-orbital angular momentum conversion in inhomogeneous anisotropic media. *Physical Review Letters*, 96(16), 2006.

[144] SJ Van Enk and G Nienhuis. Eigenfunction description of laser beams and orbital angular momentum of light. *Optics Communications*, 94(1-3):147–158, 1992.

[145] M. Padgett, J. Courtial, and L. Allen. Light's orbital angular momentum. *Physics Today*, 57(5):35–40, 2004.

[146] G. Molina-Terriza, J. P. Torres, and L. Torner. Twisted photons. *Nature Physics*, 3(5):305–310, 2007.

[147] S. Franke-Arnold, L. Allen, and M. Padgett. Advances in optical angular momentum. *Laser & Photonics Reviews*, 2(4):299–313, 2008.

[148] Alison M Yao and Miles J Padgett. Orbital angular momentum: origins, behavior and applications. *Advances in Optics and Photonics*, 3(2):161–204, 2011.

[149] E. Karimi, G. Zito, B. Piccirillo, L. Marrucci, and E. Santamato. Hypergeometric-gaussian modes. *Optics Letters*, 32(21):3053–3055, 2007.

[150] Leslie Allen, Stephen M Barnett, and Miles J Padgett. *Optical angular momentum*. CRC press, 2003.

[151] S. M. Barnett and L. Allen. Orbital angular-momentum and nonparaxial light-beams. *Optics Communications*, 110(5-6):670–678, 1994.

[152] Melvin Lax, William H Louisell, and William B McKnight. From maxwell to paraxial wave optics. *Physical Review A*, 11(4):1365, 1975.

[153] Kailiang Duan, Beizhan Wang, and Baida Lü. Propagation of hermite–gaussian and laguerre–gaussian beams beyond the paraxial approximation. *JOSA A*, 22(9):1976–1980, 2005.

[154] B. Z. Wang, Z. G. Zhao, B. D. Lu, and K. L. Duan. Vectorial hermite-laguerre-gaussian beams beyond the paraxial approximation. *Chinese Physics*, 16(1):143–147, 2007.

[155] K. Volke-Sepulveda, V. Garces-Chavez, S. Chavez-Cerda, J. Arlt, and K. Dholakia. Orbital angular momentum of a high-order bessel light beam. *Journal of Optics B-Quantum and Semiclassical Optics*, 4(2):S82–S89, 2002.

[156] J. Durnin, J. J. Miceli, and J. H. Eberly. Diffraction-free beams. *Physical Review Letters*, 58(15):1499–1501, 1987.

[157] F. Gori, G. Guattari, and C. Padovani. Bessel-gauss beams. *Optics Communications*, 64(6):491–495, 1987.

[158] Tomáš Čižmár, Veneranda Garcés-Chávez, Kishan Dholakia, and Pavel Zemánek. Optical conveyor belt for delivery of submicron objects. *Applied Physics Letters*, 86(17):174101, 2005.

[159] Z. Bouchal and M. Olivik. Non-diffractive vector bessel beams. *Journal of Modern Optics*, 42(8):1555–1566, 1995.

[160] GA Turnbull, DA Robertson, GM Smith, L Allen, and MJ Padgett. The generation of free-space laguerre-gaussian modes at millimetre-wave frequencies by use of a spiral phaseplate. *Optics communications*, 127(4-6):183–188, 1996.

[161] Alexander Jesacher, Christian Maurer, Andreas Schwaighofer, Stefan Bernet, and Monika Ritsch-Marte. Near-perfect hologram reconstruction with a spatial light modulator. *Optics Express*, 16(4):2597–2603, 2008.

[162] Jonathan Leach, Stephen Keen, Miles J Padgett, Christopher Saunter, and Gordon D Love. Direct measurement of the skew angle of the poynting vector in a helically phased beam. *Optics express*, 14(25):11919–11924, 2006.

[163] Miles Padgett and Richard Bowman. Tweezers with a twist. *Nat Photon*, 5(6):343–348, 2011.

[164] SJ Van Enk and G Nienhuis. Commutation rules and eigenvalues of spin and orbital angular momentum of radiation fields. *Journal of Modern Optics*, 41(5):963–977, 1994.

[165] A. T. O'Neil, I. MacVicar, L. Allen, and M. J. Padgett. Intrinsic and extrinsic nature of the orbital angular momentum of a light beam. *Physical Review Letters*, 88(5), 2002.

[166] Konstantin Yu Bliokh, Francisco J Rodríguez-Fortuño, Franco Nori, and Anatoly V Zayats. Spin–orbit interactions of light. *Nature Photonics*, 9(12):796–808, 2015.

[167] Y. Gorodetski, A. Niv, V. Kleiner, and E. Hasman. Observation of the spin-based plasmonic effect in nanoscale structures. *Physical Review Letters*, 101(4):043903–4, 2008.

[168] H. Kim, J. Park, S. W. Cho, S. Y. Lee, M. Kang, and B. Lee. Synthesis and dynamic switching of surface plasmon vortices with plasmonic vortex lens. *Nano Letters*, 10(2):529–536, 2010.

[169] Yu Wang, Yuntao Xu, Xue Feng, Peng Zhao, Fang Liu, Kaiyu Cui, Wei Zhang, and Yidong Huang. Optical lattice induced by angular momentum and polygonal plasmonic mode. *Optics letters*, 41(7):1478–1481, 2016.

[170] Shai Tsesses, Kobi Cohen, Evgeny Ostrovsky, Bergin Gjonaj, and Guy Bartal. Spin–orbit interaction of light in plasmonic lattices. *Nano letters*, 19(6):4010–4016, 2019.

[171] A. E. Willner, H. Huang, Y. Yan, Y. Ren, N. Ahmed, G. Xie, C. Bao, L. Li, Y. Cao, Z. Zhao, J. Wang, M. P. J. Lavery, M. Tur, S. Ramachandran, A. F. Molisch, N. Ashrafi, and S. Ashrafi. Optical communications using orbital angular momentum beams. *Advances in Optics and Photonics*, 7(1):66–106, 2015.

[172] S Barreiro and JWR Tabosa. Generation of light carrying orbital angular momentum via induced coherence grating in cold atoms. *Physical review letters*, 90(13):133001, 2003.

[173] Alois Mair, Alipasha Vaziri, Gregor Weihs, and Anton Zeilinger. Entanglement of the orbital angular momentum states of photons. *Nature*, 412(6844):313–316, 2001.

[174] X. F. Ren, G. P. Guo, Y. F. Huang, C. F. Li, and G. C. Guo. Plasmon-assisted transmission of high-dimensional orbital angular-momentum entangled state. *Europhysics Letters*, 76(5):753–759, 2006.

[175] H. He, M. E. J. Friese, N. R. Heckenberg, and H. Rubinszteindunlop. Direct observation of transfer of angular-momentum to absorptive particles from a laser-beam with a phase singularity. *Physical Review Letters*, 75(5):826–829, 1995.

[176] Dietrich Marcuse. Light transmission optics. *New York*, 1982.

[177] N. B. Simpson, K. Dholakia, L. Allen, and M. J. Padgett. Mechanical equivalence of spin and orbital angular momentum of light: An optical spanner. *Optics Letters*, 22(1):52–54, 1997.

[178] A. V. Arzola, P. Jakl, L. Chvatal, and P. Zemanek. Rotation, oscillation and hydrodynamic synchronization of optically trapped oblate spheroidal microparticles. *Optics Express*, 22(13):16207–16221, 2014.

[179] L. Paterson, M. P. MacDonald, J. Arlt, W. Sibbett, P. E. Bryant, and K. Dholakia. Controlled rotation of optically trapped microscopic particles. *Science*, 292(5518):912–914, 2001.

[180] Maria Dienerowitz, Michael Mazilu, Peter J Reece, Thomas F Krauss, and Kishan Dholakia. Optical vortex trap for resonant confinement of metal nanoparticles. *Optics express*, 16(7):4991–4999, 2008.

[181] Z. Shen, L. Su, X. C. Yuan, and Y. C. Shen. Trapping and rotating of a metallic particle trimer with optical vortex. *Applied Physics Letters*, 109(24), 2016.

[182] Kosta Ladavac and David G Grier. Microoptomechanical pumps assembled and driven by holographic optical vortex arrays. *Optics express*, 12(6):1144–1149, 2004.

[183] A. Lehmuskero, Y. M. Li, P. Johansson, and M. Kall. Plasmonic particles set into fast orbital motion by an optical vortex beam. *Optics Express*, 22(4):4349–4356, 2014.

[184] G. Knoner, S. Parkin, T. A. Nieminen, V. L. Y. Loke, N. R. Heckenberg, and H. Rubinsztein-Dunlop. Integrated optomechanical microelements. *Optics Express*, 15(9):5521–5530, 2007.

[185] Z. Shen, Z. J. Hu, G. H. Yuan, C. J. Min, H. Fang, and X. C. Yuan. Visualizing orbital angular momentum of plasmonic vortices. *Optics Letters*, 37(22):4627–4629, 2012.

[186] K. P. Yang, M. B. Pu, X. Li, X. L. Ma, J. Luo, H. Gao, and X. G. Luo. Wavelength-selective orbital angular momentum generation based on a plasmonic metasurface. *Nanoscale*, 8(24):12267–12271, 2016.

[187] Ian Goodfellow, Jean Pouget-Abadie, Mehdi Mirza, Bing Xu, David Warde-Farley, Sherjil Ozair, Aaron Courville, and Yoshua Bengio. Generative adversarial networks. *Communications of the ACM*, 63(11):139–144, 2020.

[188] Zhaocheng Liu, Dayu Zhu, Sean P Rodrigues, Kyu-Tae Lee, and Wenshan Cai. Generative model for the inverse design of metasurfaces. *Nano letters*, 18(10):6570–6576, 2018.

[189] Itzik Malkiel, Michael Mrejen, Achiya Nagler, Uri Arieli, Lior Wolf, and Haim Suchowski. Plasmonic nanostructure design and characterization via deep learning. *Light: Science & Applications*, 7(1):60, 2018.

[190] Hong Liu, Bing Wang, Eunice S. P. Leong, Ping Yang, Yun Zong, Guangyuan Si, Jinghua Teng, and Stefan A. Maier. Enhanced surface plasmon resonance on a smooth silver film with a seed growth layer. *ACS Nano*, 4(6):3139–3146, 2010.

[191] Sunae So, Trevon Badloe, Jaebum Noh, Jorge Bravo-Abad, and Junsuk Rho. Deep learning enabled inverse design in nanophotonics. *Nanophotonics*, 9(5):1041–1057, 2020.

[192] Nanfang Yu and Federico Capasso. Flat optics with designer metasurfaces. *Nat. Mater.*, 13(2):139–150, 2014.

[193] Nina Meinzer, William L Barnes, and Ian R Hooper. Plasmonic meta-atoms and metasurfaces. *Nature Photonics*, 8(12):889–898, 2014.

[194] Hou-Tong Chen, Antoinette J Taylor, and Nanfang Yu. A review of metasurfaces: physics and applications. *Reports on progress in physics*, 79(7):076401, 2016.

[195] Ebrahim Karimi, Sebastian A Schulz, Israel De Leon, Hammam Qassim, Jeremy Upham, and Robert W Boyd. Generating optical orbital angular momentum at visible wavelengths using a plasmonic metasurface. *Light: Science & Applications*, 3(5):e167–e167, 2014.

[196] Qiaoliang Bao and Kian Ping Loh. Graphene photonics, plasmonics, and broadband optoelectronic devices. *ACS nano*, 6(5):3677–3694, 2012.

[197] F Javier Garcia de Abajo. Graphene plasmonics: challenges and opportunities. *Acs Photonics*, 1(3):135–152, 2014.

[198] Denis G Baranov, Martin Wersall, Jorge Cuadra, Tomasz J Antosiewicz, and Timur Shegai. Novel nanostructures and materials for strong light–matter interactions. *Acs Photonics*, 5(1):24–42, 2018.

[199] Todd M Squires and Stephen R Quake. Microfluidics: Fluid physics at the nanoliter scale. *Reviews of modern physics*, 77(3):977, 2005.

[200] Katsuhiko Ariga, Shinsuke Ishihara, Hideki Abe, Mao Li, and Jonathan P Hill. Materials nanoarchitectonics for environmental remediation and sensing. *Journal of Materials Chemistry*, 22(6):2369–2377, 2012.

[201] Wei Gao and Joseph Wang. The environmental impact of micro/nanomachines: a review. *Acs Nano*, 8(4):3170–3180, 2014.

[202] Maria Guix, Carmen C Mayorga-Martinez, and Arben Merkoçi. Nano/micromotors in (bio) chemical science applications. *Chemical reviews*, 114(12):6285–6322, 2014.

[203] Jemish Parmar, Diana Vilela, Katherine Villa, Joseph Wang, and Samuel Sanchez. Micro- and nanomotors as active environmental microcleaners and sensors. *Journal of the American Chemical Society*, 140(30):9317–9331, 2018.

[204] Vincent LY Loke, Theodor Asavei, Alexander B Stilgoe, Timo A Nieminen, and Halina Rubinsztein-Dunlop. Driving corrugated donut rotors with laguerre-gauss beams. *Optics express*, 22(16):19692–19706, 2014.

[205] John Parker, Curtis W Peterson, Yuval Yifat, Stuart A Rice, Zijie Yan, Stephen K Gray, and Norbert F Scherer. Optical matter machines: angular momentum conversion by collective modes in optically bound nanoparticle arrays. *Optica*, 7(10):1341–1348, 2020.

[206] Hong Wang and Martin Pumera. Fabrication of micro/nanoscale motors. *Chemical reviews*, 115(16):8704–8735, 2015.

[207] Peter Muhlschlegel, H-J Eisler, Olivier JF Martin, Bert Hecht, and DW Pohl. Resonant optical antennas. *science*, 308(5728):1607–1609, 2005.

[208] Yanrong Chen, Haihua Wu, Zhipeng Li, Peijie Wang, Longkun Yang, and Yan Fang. The study of surface plasmon in au/ag core/shell compound nanoparticles. *Plasmonics*, 7(3):509–513, 2012.

[209] Kathryn M Mayer and Jason H Hafner. Localized surface plasmon resonance sensors. *Chemical reviews*, 111(6):3828–3857, 2011.

[210] Ying Gu, Lina Huang, Olivier JF Martin, and Qihuang Gong. Resonance fluorescence of single molecules assisted by a plasmonic structure. *Physical Review B*, 81(19):193103, 2010.

[211] Paul L Stiles, Jon A Dieringer, Nilam C Shah, and Richard P Van Duyne. Surface-enhanced raman spectroscopy. *Annu. Rev. Anal. Chem.*, 1:601–626, 2008.

[212] Guillaume Baffou, Romain Quidant, and F Javier García de Abajo. Nanoscale control of optical heating in complex plasmonic systems. *ACS nano*, 4(2):709–716, 2010.

[213] Pawel Karpinski, Steven Jones, Hana Sipova-Jungova, Ruggero Verre, and Mikael Käll. Optical rotation and thermometry of laser tweezed silicon nanorods. *Nano letters*, 20(9):6494–6501, 2020.

[214] Katherine A Willets and Richard P Van Duyne. Localized surface plasmon resonance spectroscopy and sensing. *Annu. Rev. Phys. Chem.*, 58:267–297, 2007.

[215] Prashant K Jain, Xiaohua Huang, Ivan H El-Sayed, and Mostafa A El-Sayed. Noble metals on the nanoscale: optical and photothermal properties and some applications in imaging, sensing, biology, and medicine. *Accounts of chemical research*, 41(12):1578–1586, 2008.

[216] Ya-Xin Hu, Ren-Chao Jin, Xiao-Rui Zhang, Li-Li Tang, Jia-Qi Li, Jin Wang, and Zheng-Gao Dong. Negative optical torque in spin-dependent 2d chiral nanomotor due to dipolar scattering. *Optics Communications*, 482:126560, 2021.

[217] PV Ruijgrok, NR Verhart, P Zijlstra, AL Tchebotareva, and MAGJ Orrit. Brownian fluctuations and heating of an optically aligned gold nanorod. *Physical review letters*, 107(3):037401, 2011.

[218] Michael I Jordan and Tom M Mitchell. Machine learning: Trends, perspectives, and prospects. *Science*, 349(6245):255–260, 2015.

[219] Junfei Qiu, Qihui Wu, Guoru Ding, Yuhua Xu, and Shuo Feng. A survey of machine learning for big data processing. *EURASIP Journal on Advances in Signal Processing*, 2016(1):1–16, 2016.

[220] Alexander Selvikvåg Lundervold and Arvid Lundervold. An overview of deep learning in medical imaging focusing on mri. *Zeitschrift für Medizinische Physik*, 29(2):102–127, 2019.

[221] Waseem Rawat and Zenghui Wang. Deep convolutional neural networks for image classification: A comprehensive review. *Neural computation*, 29(9):2352–2449, 2017.

[222] Tom Young, Devamanyu Hazarika, Soujanya Poria, and Erik Cambria. Recent trends in deep learning based natural language processing. *ieee Computational intelligenCe magazine*, 13(3):55–75, 2018.

[223] Ruben Tolosana, Ruben Vera-Rodriguez, Julian Fierrez, Aythami Morales, and Javier Ortega-Garcia. Deepfakes and beyond: A survey of face manipulation and fake detection. *Information Fusion*, 64:131–148, 2020.

[224] Sandeep Inampudi and Hossein Mosallaei. Neural network based design of metagratings. *Applied Physics Letters*, 112(24):241102, 2018.

[225] A Comin and A Hartschuh. Efficient optimization of shg hotspot switching in plasmonic nanoantennas using phase-shaped laser pulses controlled by neural networks. *Optics express*, 26(26):33678–33686, 2018.

[226] Neuton Li, Jasper Cadusch, Amelia Liu, Anders J Barlow, Ann Roberts, and Kenneth B Crozier. Algorithm-designed plasmonic nanotweezers: Quantitative comparison by theory, cathodoluminescence, and nanoparticle trapping. *Advanced Optical Materials*, 9(19):2100758, 2021.

[227] Gandhi Alagappan and Ching Eng Png. Modal classification in optical waveguides using deep learning. *Journal of Modern Optics*, 66(5):557–561, 2019.

[228] André-Pierre Blanchard-Dionne and Olivier JF Martin. Teaching optics to a machine learning network. *Optics Letters*, 45(10):2922–2925, 2020.

[229] Iman Sajedian, Trevon Badloe, and Junsuk Rho. Optimisation of colour generation from dielectric nanostructures using reinforcement learning. *Optics express*, 27(4):5874–5883, 2019.

[230] Kan Yao, Rohit Unni, and Yuebing Zheng. Intelligent nanophotonics: merging photonics and artificial intelligence at the nanoscale. *Nanophotonics*, 8(3):339–366, 2019.

[231] Peter R Wiecha, Arnaud Arbouet, Christian Girard, and Otto L Muskens. Deep learning in nano-photonics: inverse design and beyond. *Photonics Research*, 9(5):B182–B200, 2021.

[232] Kaiming He, Xiangyu Zhang, Shaoqing Ren, and Jian Sun. Deep residual learning for image recognition. In *Proceedings of the IEEE conference on computer vision and pattern recognition*, pages 770–778, 2016.

[233] Jiuxiang Gu, Zhenhua Wang, Jason Kuen, Lianyang Ma, Amir Shahroudy, Bing Shuai, Ting Liu, Xingxing Wang, Gang Wang, Jianfei Cai, et al. Recent advances in convolutional neural networks. *Pattern Recognition*, 77:354–377, 2018.

[234] Andreas M Kern and Olivier JF Martin. Surface integral formulation for 3d simulations of plasmonic and high permittivity nanostructures. *JOSA A*, 26(4):732–740, 2009.

[235] Alok Ji, TV Raziman, Jérémy Butet, RP Sharma, and Olivier JF Martin. Optical forces and torques on realistic plasmonic nanostructures: a surface integral approach. *Optics letters*, 39(16):4699–4702, 2014.

[236] MATLAB. *version 9.5 (R2018b)*. The MathWorks Inc., Natick, Massachusetts, 2018.

[237] Diederik P Kingma and Jimmy Ba. Adam: A method for stochastic optimization. *arXiv preprint arXiv:1412.6980*, 2014.

[238] David Silver, Aja Huang, Chris J Maddison, Arthur Guez, Laurent Sifre, George Van Den Driessche, Julian Schrittwieser, Ioannis Antonoglou, Veda Panneershelvam, Marc Lanctot, et al. Mastering the game of go with deep neural networks and tree search. *nature*, 529(7587):484–489, 2016.

[239] Weibo Liu, Zidong Wang, Xiaohui Liu, Nianyin Zeng, Yurong Liu, and Fuad E Alsaadi. A survey of deep neural network architectures and their applications. *Neurocomputing*, 234:11–26, 2017.

[240] Alec Radford, Luke Metz, and Soumith Chintala. Unsupervised representation learning with deep convolutional generative adversarial networks. *arXiv preprint arXiv:1511.06434*, 2015.

[241] Mintae Chung, Karim Achouri, and Olivier J. F. Martin. Dataset for the manuscript: Demonstration of the optically-driven plasmonic nanomotor designed by deep learning networks. https://doi.org/10.5281/zenodo.6697321, 2022. Zenodo.

[242] T. V. Raziman, W. R. C. Somerville, O. J. F. Martin, and E. C. Le Ru. Accuracy of surface integral equation matrix elements in plasmonic calculations. *Journal of the Optical Society of America B*, 32(3):485–492, 2015.

[243] Sadasiva Rao, Donald Wilton, and Allen Glisson. Electromagnetic scattering by surfaces of arbitrary shape. *IEEE Transactions on antennas and propagation*, 30(3):409–418, 1982.

[244] JP Kottmann, OJF Martin, David R Smith, and Sheldon Schultz. Field polarization and polarization charge distributions in plasmon resonant nanoparticles. *New Journal of Physics*, 2(1):27, 2000.

[245] Andreas M Kern and Olivier JF Martin. Pitfalls in the determination of optical cross sections from surface integral equation simulations. *IEEE Transactions on Antennas and Propagation*, 58(6):2158–2161, 2010.

[246] Stefan Mühlig, Christoph Menzel, Carsten Rockstuhl, and Falk Lederer. Multipole analysis of meta-atoms. *Metamaterials*, 5(2-3):64–73, 2011.

[247] TV Raziman, Robert Julius Wolke, and Olivier JF Martin. Optical forces in nanoplasmonic systems: how do they work, what can they be useful for? *Faraday discussions*, 178:421–434, 2015.

[248] Andreas M Kern and Olivier JF Martin. Modeling near-field properties of plasmonic nanoparticles: a surface integral approach. In *Plasmonics: Nanoimaging, Nanofabrication, and their Applications V*, volume 7395, page 739518. International Society for Optics and Photonics, 2009.

[249] Craig F Bohren and Donald R Huffman. *Absorption and scattering of light by small particles*. John Wiley & Sons, 2008.

[250] P. B. Johnson and R. W. Christy. Optical constants of the noble metals. *Phys. Rev. B*, 6(12):4370–4379, 1972.

[251] Karim Achouri, Andrei Kiselev, and Olivier JF Martin. Multipolar origin of electromagnetic transverse force resulting from two-wave interference. *Physical Review B*, 102(8):085107, 2020.

[252] C. Girard, A. Dereux, O. J. F. Martin, and M. Devel. Importance of confined fields in near-field optical imaging of subwavelength objects. *Physical Review B Condensed Matter*, 50(19):14467–73, 1994.

[253] Xiaojin Jiao, Jeremy Goeckeritz, Steve Blair, and Mark Oldham. Localization of near-field resonances in bowtie antennae: influence of adhesion layers. *Plasmonics*, 4(1):37–50, 2009.

[254] Nicolas Gosset, Mohamed Boufnichel, Emilie Bahette, Walid Khalfaoui, Rami Ljazouli, Virginie Grimal-Perrigouas, and Remi Dussart. Single and multilayered materials processing by argon ion beam etching: study of ion angle incidence and defect formation. *Journal of Micromechanics and Microengineering*, 25(9):095011, 2015.

[255] B. Abasahl, C. Santschi, T. V. Raziman, and O. J. F. Martin. Fabrication of plasmonic structures with well-controlled nanometric features: a comparison between lift-off and ion beam etching. *Nanotechnology*, 32(47):475202, 2021.

[256] Debdatta Ray, Hsiang-Chu Wang, Jeonghyeon Kim, Christian Santschi, and Olivier JF Martin. A low-temperature annealing method for alloy nanostructures and metasurfaces: Unlocking a novel degree of freedom. *Advanced Materials*, 34(17):2108225, 2022.

[257] Christophe Vieu, F Carcenac, A Pepin, Y Chen, M Mejias, A Lebib, L Manin-Ferlazzo, L Couraud, and H Launois. Electron beam lithography: resolution limits and applications. *Applied surface science*, 164(1-4):111–117, 2000.

[258] Weihua Zhang, Holger Fischer, Thomas Schmid, Renato Zenobi, and Olivier JF Martin. Mode-selective surface-enhanced raman spectroscopy using nanofabricated plasmonic dipole antennas. *The Journal of Physical Chemistry C*, 113(33):14672–14675, 2009.

[259] Marc J Madou. *Fundamentals of microfabrication: the science of miniaturization*. CRC press, 2018.

[260] Rainer Behrisch and K Wittmaack. *Sputtering by particle bombardment*, volume 1. Springer-Verlag New York, 1981.

[261] BXE Desbiolles, A Bertsch, and P Renaud. Ion beam etching redeposition for 3d multimaterial nanostructure manufacturing. *Microsystems & nanoengineering*, 5(1):1–8, 2019.

[262] Woo-Bin Jung, Sungwoo Jang, Soo-Yeon Cho, Hwan-Jin Jeon, and Hee-Tae Jung. Recent progress in simple and cost-effective top-down lithography for ≈10 nm scale nanopatterns: From edge lithography to secondary sputtering lithography. *Advanced Materials*, 32(35):1907101, 2020.

[263] Hubert Gnaser. Energy and angular distributions of sputtered species. In *Sputtering by particle bombardment*, pages 231–328. Springer, 2007.

[264] Rainer Behrisch and Wolfgang Eckstein. *Sputtering by particle bombardment: experiments and computer calculations from threshold to MeV energies*, volume 110. Springer Science & Business Media, 2007.

[265] Harold R Kaufman, Stephen M Rossnagel, and Jerome J Cuomo. *Handbook of Ion Beam Processing Technology: Principles, Deposition, Film Modification and Synthesis*. Noyes Publications, 1989.

[266] Hwan-Jin Jeon, Kyoung Hwan Kim, Youn-Kyoung Baek, Dae Woo Kim, and Hee-Tae Jung. New top-down approach for fabricating high-aspect-ratio complex nanostructures with 10 nm scale features. *Nano letters*, 10(9):3604–3610, 2010.

[267] Dennis M Manos and Daniel L Flamm. Plasma etching: an introduction.(retroactive coverage). *Academic Press, Inc.(United States), 1989,*, page 476, 1989.

[268] KR Milkove and CX Wang. Insight into the dry etching of fence-free patterned platinum structures. *Journal of Vacuum Science & Technology A: Vacuum, Surfaces, and Films*, 15(3):596–603, 1997.

[269] JME Harper, JJ Cuomo, Po A Leary, GM Summa, HR Kaufman, and FJ Bresnock. Low energy ion beam etching. *Journal of the Electrochemical Society*, 128(5):1077, 1981.

[270] Minghui Chen, Quan Liu, and Jianhong Wu. A method of fabricating blazed grating by homogenous grating mask. In *2011 International Conference on Optical Instruments and Technology: Solid State Lighting and Display Technologies, Holography, Speckle Pattern Interferometry, and Micro/Nano Manufacturing and Metrology*, volume 8202, pages 308–314. SPIE, 2011.

[271] John Melngailis. Focused ion beam technology and applications. *Journal of Vacuum Science & Technology B: Microelectronics Processing and Phenomena*, 5(2):469–495, 1987.

[272] Julie M Cairney, Robert D Smith, and Paul R Munroe. Transmission electron microscope specimen preparation of metal matrix composites using the focused ion beam miller. *Microscopy and Microanalysis*, 6(5):452–462, 2000.

[273] S Rajsiri, BW Kempshall, SM Schwarz, and LA Giannuzzi. Fib damage in silicon: Amorphization or redeposition? *Microscopy and Microanalysis*, 8(S02):50–51, 2002.

[274] BI Prenitzer, BW Kempshall, SM Schwarz, LA Giannuzzi, and FA Stevie. Practical aspects of fib milling: Understanding ion beam/material interactions. *Microscopy and Microanalysis*, 6(S2):502–503, 2000.

[275] Sloan Lindsey and Gerhard Hobler. The significance of redeposition and backscattering in nanostructure formation by focused ion beams. *Nuclear Instruments and Methods in Physics Research Section B: Beam Interactions with Materials and Atoms*, 282:12–16, 2012.

[276] Steve Reyntjens and Robert Puers. A review of focused ion beam applications in microsystem technology. *Journal of micromechanics and microengineering*, 11(4):287, 2001.

[277] C-M Park, JA Bain, TW Clinton, PAA Van der Heijden, and TJ Klemmer. Measurement of ga implantation profiles in the sidewall and bottom of focused-ion-beam-etched structures. *Applied physics letters*, 84(17):3331–3333, 2004.

[278] Komal Pandey, Kristof Paredis, Thomas Hantschel, Chris Drijbooms, and Wilfried Vandervorst. The impact of focused ion beam induced damage on scanning spreading resistance microscopy measurements. *Scientific Reports*, 10(1):1–15, 2020.

[279] Vladimir Tuboltsev and Jyrki Räisänen. Ion beam processing of au nanowires. *Nanotechnology*, 20(33):335302, 2009.

[280] Ch Santschi, M Jenke, P Hoffmann, and J Brugger. Interdigitated 50 nm ti electrode arrays fabricated using xef2 enhanced focused ion beam etching. *Nanotechnology*, 17(11):2722, 2006.

[281] Xudi Wang, Ying Liu, Xiangdong Xu, Shaojun Fu, and Zheng Cui. Reactive ion beam etching of hf o 2 film and removal of sidewall redeposition. *Journal of Vacuum Science & Technology A: Vacuum, Surfaces, and Films*, 24(4):1067–1072, 2006.

[282] Akash Kannegulla and Li-Jing Cheng. Metal assisted focused-ion beam nanopatterning. *Nanotechnology*, 27(36):36LT01, 2016.

[283] T Vermeij, E Plancher, and CC Tasan. Preventing damage and redeposition during focused ion beam milling: the “umbrella” method. *Ultramicroscopy*, 186:35–41, 2018.

[284] Nigel P Hacker. Organic and inorganic spin-on polymers for low-dielectric-constant applications. *MRS bulletin*, 22(10):33–38, 1997.

[285] S Lis, R Dylewicz, J Mysliwiec, A Miniewicz, and S Patela. Application of flowable oxides in photonics. *Materials Science-Poland*, 26(1):189–194, 2008.

[286] Sookyung Choi, Michael J Word, Vipan Kumar, and Ilesanmi Adesida. Comparative study of thermally cured and electron-beam-exposed hydrogen silsesquioxane resists. *Journal of Vacuum Science & Technology B: Microelectronics and Nanometer Structures Processing, Measurement, and Phenomena*, 26(5):1654–1659, 2008.

[287] Zhuojun Liu, Jiayi Wang, Bo Chen, Yuming Wei, Wenjing Liu, and Jin Liu. Giant enhancement of continuous wave second harmonic generation from few-layer gase coupled to high-q quasi bound states in the continuum. *Nano Letters*, 21(17):7405–7410, 2021.

[288] Wei-Yi Tsai, Jer-Shing Huang, and Chen-Bin Huang. Selective trapping or rotation of isotropic dielectric microparticles by optical near field in a plasmonic archimedes spiral. *Nano letters*, 14(2):547–552, 2014.

[289] Chuhuan Feng, Qi Li, Yangjian Zeng, Xin Su, and Hongbin Yu. 2d to 3d convertible terahertz chiral metamaterial with integrated pneumatic actuator. *Optics Express*, 26(11):14421–14432, 2018.

[290] Hiromi Okamoto. Local optical activity of nano-to microscale materials and plasmons. *Journal of Materials Chemistry C*, 7(47):14771–14787, 2019.

[291] IV Katardjiev, G Carter, MJ Nobes, and R Smith. Precision modeling of the mask–substrate evolution during ion etching. *Journal of Vacuum Science & Technology A: Vacuum, Surfaces, and Films*, 6(4):2443–2450, 1988.

[292] Michael E Walsh, Yaowu Hao, Caroliine A Ross, and Henry I Smith. Optimization of a lithographic and ion beam etching process for nanostructuring magnetoresistive thin film stacks. *Journal of Vacuum Science & Technology B: Microelectronics and Nanometer Structures Processing, Measurement, and Phenomena*, 18(6):3539–3543, 2000.

[293] Jeffrey R Moffitt, Yann R Chemla, Steven B Smith, and Carlos Bustamante. Recent advances in optical tweezers. *Annual review of biochemistry*, 77(1):205–228, 2008.

[294] Jonathan A Fan, Chihhui Wu, Kui Bao, Jiming Bao, Rizia Bardhan, Naomi J Halas, Vinothan N Manoharan, Peter Nordlander, Gennady Shvets, and Federico Capasso. Self-assembled plasmonic nanoparticle clusters. *science*, 328(5982):1135–1138, 2010.

[295] Linhan Lin, Jianli Zhang, Xiaolei Peng, Zilong Wu, Anna CH Coughlan, Zhangming Mao, Michael A Bevan, and Yuebing Zheng. Opto-thermophoretic assembly of colloidal matter. *Science advances*, 3(9):e1700458, 2017.

[296] Linhan Lin, Mingsong Wang, Xiaolei Peng, Emanuel N Lissek, Zhangming Mao, Leonardo Scarabelli, Emily Adkins, Sahin Coskun, Husnu Emrah Unalan, Brian A Korgel, et al. Opto-thermoelectric nanotweezers. *Nature photonics*, 12(4):195–201, 2018.

[297] Sangeeta Saini, Harjinder Singh, and Biman Bagchi. Fluorescence resonance energy transfer (fret) in chemistry and biology: Non-förster distance dependence of the fret rate. *Journal of Chemical Sciences*, 118(1):23–35, 2006.

[298] Anisa Kaur and Soma Dhakal. Recent applications of fret-based multiplexed techniques. *TrAC Trends in Analytical Chemistry*, 123:115777, 2020.

[299] Hans Albrecht Bethe. Theory of diffraction by small holes. *Physical review*, 66(7-8):163, 1944.

[300] Seymour B Cohn. Microwave coupling by large apertures. *Proceedings of the IRE*, 40(6):696–699, 1952.

[301] Y Pang, C Genet, and TW Ebbesen. Optical transmission through subwavelength slit apertures in metallic films. *Optics Communications*, 280(1):10–15, 2007.

[302] FJ Garcia De Abajo. Light transmission through a single cylindrical hole in a metallic film. *Optics Express*, 10(25):1475–1484, 2002.

[303] Evgeny Popov, Nicolas Bonod, Michel Nevière, Hervé Rigneault, Pierre-François Lenne, and Patrick Chaumet. Surface plasmon excitation on a single subwavelength hole in a metallic sheet. *Applied optics*, 44(12):2332–2337, 2005.

[304] A Degiron, HJ Lezec, N Yamamoto, and TW Ebbesen. Optical transmission properties of a single subwavelength aperture in a real metal. *Optics Communications*, 239(1-3):61–66, 2004.

[305] FJ Garcia-Vidal, Esteban Moreno, JA Porto, and L Martin-Moreno. Transmission of light through a single rectangular hole. *Physical review letters*, 95(10):103901, 2005.

[306] A Degiron and TW Ebbesen. Analysis of the transmission process through single apertures surrounded by periodic corrugations. *Optics express*, 12(16):3694–3700, 2004.

[307] Sergio G Rodrigo, Fernando de Leon-Perez, and Luis Martin-Moreno. Extraordinary optical transmission: fundamentals and applications. *Proceedings of the IEEE*, 104(12):2288–2306, 2016.

[308] Xiao Hu, Li Zhan, and Yuxing Xia. Color filters based on enhanced optical transmission of subwavelength-structured metallic film for multicolor organic light-emitting diode display. *Applied optics*, 47(23):4275–4279, 2008.

[309] C Genet and TW Ebbesen. Light in tiny holes. In *Nanoscience And Technology: A Collection of Reviews from Nature Journals*, pages 205–212. World Scientific, 2010.

[310] Thomas W Ebbesen, Henri J Lezec, HF Ghaemi, Tineke Thio, and Peter A Wolff. Extraordinary optical transmission through sub-wavelength hole arrays. *nature*, 391(6668):667–669, 1998.

[311] HF Ghaemi, Tineke Thio, DE e al Grupp, Thomas W Ebbesen, and HJ Lezec. Surface plasmons enhance optical transmission through subwavelength holes. *Physical review B*, 58(11):6779, 1998.

[312] FJ Garcia De Abajo. Colloquium: Light scattering by particle and hole arrays. *Reviews of Modern Physics*, 79(4):1267, 2007.

[313] Francisco J Garcia-Vidal, Luis Martin-Moreno, TW Ebbesen, and L Kuipers. Light passing through subwavelength apertures. *Reviews of Modern Physics*, 82(1):729, 2010.

[314] Cyriaque Genet, Martin P van Exter, and JP Woerdman. Fano-type interpretation of red shifts and red tails in hole array transmission spectra. *Optics Communications*, 225(4-6):331–336, 2003.

[315] Romain Quidant, Dmitri Petrov, and Gonçal Badenes. Radiation forces on a rayleigh dielectric sphere in a patterned optical near field. *Optics letters*, 30(9):1009–1011, 2005.

[316] M Righini, C Girard, and R Quidant. Light-induced manipulation with surface plasmons. *Journal of Optics A: Pure and Applied Optics*, 10(9):093001, 2008.

[317] R Sainidou and FJ Garcia De Abajo. Optically tunable surfaces with trapped particles in microcavities. *Physical review letters*, 101(13):136802, 2008.

[318] Eun-Soo Kwak, Tiberiu-Dan Onuta, Dragos Amarie, Radislav Potyrailo, Barry Stein, Stephen C Jacobson, WL Schaich, and Bogdan Dragnea. Optical trapping with integrated near-field apertures. *The Journal of Physical Chemistry B*, 108(36):13607–13612, 2004.

[319] AN Grigorenko, NW Roberts, MR Dickinson, and Y Zhang. Nanometric optical tweezers based on nanostructured substrates. *Nature Photonics*, 2(6):365, 2008.

[320] Kai Wang, Ethan Schonbrun, Paul Steinvurzel, and Kenneth B Crozier. Nanoparticle manipulation using a plasmonic nano-tweezer with an integrated heat sink. In *CLEO: 2011-Laser Science to Photonic Applications*, pages 1–2. IEEE, 2011.

[321] Mathieu L Juan, Maurizio Righini, and Romain Quidant. Plasmon nano-optical tweezers. *Nature photonics*, 5(6):349, 2011.

[322] Kevin L Prime and George M Whitesides. Self-assembled organic monolayers: Model systems for studying adsorption of proteins at aurfaces. *Science*, 252(5009):1164–1167, 1991.

[323] Greg T Hermanson. *Bioconjugate techniques*. Academic press, 2013.

[324] Thermofisher. Carbodiimide Crosslinker Chemistry. https://www.thermofisher.com/ch/en/home/life-science/protein-biology/protein-biology-learning-center/protein-biology-resource-library/pierce-protein-methods/carbodiimide-crosslinker-chemistry.html, 2013. [Online;].

[325] Yongxia Zhang, Kadir Aslan, Michael JR Previte, and Chris D Geddes. Low temperature metal-enhanced fluorescence. *Journal of fluorescence*, 17(6):627–631, 2007.

[326] KRISTER Holmberg and BERTIL Hansen. Ester synthesis with dicyclohexylcarbodiimide improved by acid catalysts. *Acta Chem. Scand. B*, 33:410–412, 1979.

[327] Nathan S Claxton, Thomas J Fellers, and Michael W Davidson. Laser scanning confocal microscopy. *Department of Optical Microscopy and Digital Imaging, Florida State University, Tallahassee, http://www. olympusconfocal. com/theory/LSCMIntro. pdf*, 2006.

[328] Chie Hosokawa, Hiroyuki Yoshikawa, and Hiroshi Masuhara. Optical assembling dynamics of individual polymer nanospheres investigated by single-particle fluorescence detection. *Physical Review E*, 70(6):061410, 2004.

[329] Jean-Marc Fournier, Johann Rohner, Pierre Jacquot, Robert Johann, Solon Mias, and René-P Salathé. Assembling mesoscopic particles by various optical schemes. In *Optical Trapping and Optical Micromanipulation II*, volume 5930, pages 238–247. SPIE, 2005.

[330] Min-Cheng Zhong, Ai-Yin Liu, and Rong Zhu. Optical assembling of micro-particles at a glass–water interface with diffraction patterns caused by the limited aperture of objective. *Applied Sciences*, 8(9):1522, 2018.

Curriculum Vitae

MINTAE CHUNG

Born in 1st July 1989 in Seoul (Republic of Korea)

Nationality: Korean (Republic of Korea)

Address : Route du Bois 57, 1024 Ecublens VD, Canton de Vaud, Suisse

Mobile: +41 78 709 71 86 or +82 10 8897 2155 • E-mail: mintae.chung@epfl.ch or mintae7605@gmail.com

EDUCATION

• Doctor's degree

École Polytechnique Fédéral de Lausanne, EPFL* (Lausanne), *Switzerland ***Jan. 2018 – Present***
Nanophotonics and Metrology laboratory, EDPO, EPFL with Prof. Olivier J.F. Martin
Main works: Design and Nanofabrication of Photonic Devices at the Nanoscale.

• Master's degree (Dual Master's Program)

École Polytechnique* (Paris*), France ***Feb. 2016 – Sep. 2017***
Major: Innovation Technology

Kyung-Hee University* (Seoul), *Republic of Korea ***Mar. 2015 – Jan. 2016***
Major: Information Display

• Bachelor's degree

Kyung-Hee University* (Seoul), *Republic of Korea ***Mar. 2009 – Feb. 2015***
Major: Information Display
Military Service (Aug. 2010 – May.2012)

PROFESSIONAL EXPERIENCES

• Master Internship

- **École polytechnique fédérale de Lausanne, LMSC, Switzerland** ***Apr. 2017 – Dec. 2017***
  - with Prof. Anna Foncuberta i Morral "The optimization and the characterization of Gallium Arsenide nano membrane grown by Molecular Beam Epitaxy (MBE) on the silicon substrate".
  - main work: Nanofabrication with E-beam lithography in cleanroom (CMi) and GaAs MBE growth.

- **École polytechnique, LPICM, France** ***Apr. 2016 – Aug. 2016***
  - with Prof. Pere Roca i Cabarrocas "Analyse de cellules solaires à l'échelle nanométrique Assigned activities: Mesures à l'échelle nanométrique par microscopie de sonde locale (KPFM et CP-AFM) sur des cellules solaires, échantillon de dopage, wafers passive."
  - main work: Surface potential detecting and analysis on various solar-cell structures using KPFM.

- **Advanced Display Research Center (ADRC), Republic of Korea** ***Feb. 2015 – Jan. 2016***
  - with Prof. Kyu-chang Park " *Thin film silicon crystallization with electron beam and analysis of electric and optical properties of the crystallized silicon*".
  - main work: Amorphous silicon thin film crystallization with an electron beam from CNT tips.

EXTRA CURRICULUM VITAE

Language Skills

- Korean (Native)
- English (Advanced)
- French (B1 in TCF, Nov. 2016)

Software Skills

- Tensorflow for artificial intelligence using CNN and DCGAN networks
- CST studio & Comsol multiphysic & Lumerical & Zemax for optics and nanoplasmonic structures
- Python & Matlab for data analysis
- Nextnano (Photo detector design, Bandstructure optimization)

Metrology experiences

- Scanning electron microscopy (SEM), facility: Zeiss Merlin, usage duration: 6 years
- Focused ion beam (FIB), facility: FEI Nova 600 and Zeiss CrossBeam 540, usage duration: 5 years
- Atomic force microscopy (AFM), facility: Bruker FastScan AFM, usage duration: 2 years
- Ellipsometer, facility: Sopra GES 5E, usage duration: 2 years

Fabrication tool experiences

- Electron beam lithography (EBL), facility: Raith EBP5000+, usage duration: 6 years
    - Resists treated: HSQ, ZEP, PMMA
- Ion beam etcher (IBE), facility: NEXUS Veeco IBE, usage duration: 5 years
- Dielectric plasma etcher, facility: SPTS APS, usage duration: 6 years
- Electron beam evaporator, facility: Leybold-Optics LAB600 H, usage duration: 6 years
- Metallic film sputter, facility: Alliance-Concept DP650, usage duration: 6years

PUBLICATIONS

Chung, M.; Achouri, K.; Martin, O. J. F. (2022). Demonstration of optically-driven plasmonic nanomotors designed by deep learning networks, *Nature computational science*, Manuscript under review.

Chung, M.; Santschi, C.; Martin, O. J. F. (2022). Fence-free ion beam etching of plasmonic gold nanostructures. Manuscript in preparation.

Chung, M.; Martin, O. J. F. (2022). Optical micro/nanomotors driven by light momenta (review article). Manuscript in preparation.

Achouri, K.; Chung, M.; Kiselev, A.; Martin, O. J. F. (2022). Extrinsic multipolar chiral induced optical torque. Manuscript in preparation.

Lee, H. R.; Kang, J. S.; Chung, M.; & Park, K. C. (2017). Pseudo-Crystalline Silicon Thin Films with Carbon Nanotube Electron Beam Exposure. *Journal of Nanoscience and Nanotechnology*, *17*(11), 7852-7858.

Kang, J. S.; Hong, J. H.; Chung, M.; & Park, K. C. (2016). Highly stable carbon nanotube cathode for electron beam application. *Journal of Vacuum Science & Technology B, Nanotechnology and Microelectronics: Materials, Processing, Measurement, and Phenomena*, *34*(2), 02G104.

PATENT

"Integration of a short-wave infrared detector with cmos compatible substrates", Anna Fontcuberta i Morral, Mintae Chung, European Patent, EP3794643B1, filed May 16, 2018 and granted June 22, 2022.

"Short-wave infrared detector and its integration with cmos compatible substrates" (pending), Anna Fontcuberta i Morral, Mintae Chung, US Patent, US20210210544A1, filed May 16, 2018 and published July 08, 2021.

AWARDS AND HONORS

Best Poster Awards – 1st prize, "Demonstration of the optically-driven plasmonic nanomotor designed by deep learning networks", EPFL Photonics Day 2021.

CONFERENCE

- Poster presentation at SPP9 - 9*th* international conference on surface plasmon polariton, near-field optics, nanophotonics & related techniques, Title: Visualization of optical trapping of nanoparticles using fluorescence resonance energy transfer (FRET), Copenhagen (Denmark), May 2019

- Poster presentation at NFO15 - 15*th* international conference on near-field optics, surface plasmon polaritons, nanophotonics & related techniques, Title: Massive parallel optical trapping of nanoparticles, Troyes (France), September 2018

- Oral presentation at IDW2015 – 22*nd* international display workshops on oxide-semiconductor TFT, augmented reality and virtual reality, lighting technologies & printed electronics. Title: Pseudo-crystalline silicon PIN diode with carbon nanotube electron beam (C-Beam) exposure technique, Otsu (Japan), December 2015